Quantifying the Response of Relative Brain/Skull Motion to Rotational Input in the PMHS Head

Allison Jean Guettler

Thesis submitted to the faculty of the Virginia Polytechnic Institute and State University in partial fulfillment of the requirements for the degree of

Master of Science
In
Mechanical Engineering

Warren N. Hardy, Chair
Pamela J. VandeVord, Co-Chair
Steve C. Southward
Costin D. Untaroiu
John H. Bolte IV

December 18, 2017
Blacksburg, Virginia

Keywords: Traumatic Brain Injury, Biomechanics, Cadaver

Quantifying the Response of Relative Brain/Skull Motion to Rotational Input in the PMHS Head

Allison Jean Guettler

ABSTRACT

Post-mortem human surrogate (PMHS) head specimens were subjected to two different angular speed pulses. Each pulse was approximately a half-sine with either a peak angular speed of either 40 or 20 rad/s and duration of either 30 or 60 milliseconds. High-speed biplane x-ray was used to record the motion of the brain and skull via radio-opaque markers implanted at specified locations in the brain, and lead markers on the skull. Specimens were perfused to physiologic conditions throughout preparation and testing to maintain the integrity of the brain tissue and ensure coupling of the brain and skull. Intracranial pressure was measured anteriorly and posteriorly. The test event was controlled by a cam-follower-flywheel mechanism, which facilitated control of pulse parameters and provided a form of "extreme energy" so that the device and therefore the test input would not be influenced by the characteristics of the object under test. This approach kept the independent and dependent variables separated. The brain targets were also deployed in a prescribed manner with two methodologies that were scalable to different specimens. The repeatable input and target deployment schemes helped reduce experimental variation (between tests and subjects) to produce consistent response data. Displacement of the brain was calculated with respect to a body-fixed basis on the skull. The relative motion of the brain with respect to the skull was shown to be dependent on the location of the target in the brain. The major deformation axis of each target followed the contour of the skull or bony landmark to which it was closest. Intracranial pressure

was relatively low because the changes were due to inertial effects in the absence of impact. Tests with lower speeds and longer durations produced less deformation, lower intracranial pressures, and longer pressure durations than the tests that were high-speed, short-duration. The response of the brain to rotation of the head was quantified at two test levels and on two PMHS specimens.

Quantifying the Response of Relative Brain/Skull Motion to Rotational Input in the PMHS Head

Allison Jean Guettler

GENERAL AUDIENCE ABSTRACT

Motor-vehicle collisions (MVCs) are the second leading cause of traumatic brain injury (TBI) in the United States and the leading cause of TBI-related death [1a]. Regulations are in place for vehicle design to reduce the occurrence and severity of head injuries during MVCs. The metric used is based on the resultant linear acceleration at the center of gravity of the occupant's head. However, TBI are still occurring despite the current regulations. This suggests the importance of using additional injury metrics to predict TBI in MVCs.

In automotive impact biomechanics, a combination of real world, experimental, and simulation data is used to determine how the human body responds during MVCs. While computer (finite element) simulations can provide extensive information about the kinematic and kinetic response of the human body, these models require experimental data to validate and evaluate their responses.

This study focuses on determining the response of the human cadaver brain to angular speed loading without contact of the head. High-speed biplane x-ray and radiopaque markers were used to quantify the displacement of the brain with respect to the skull throughout rotational events. Two angular speed profiles with different peak angular speeds and durations were used. The methods were determined to reduce experimental variation to obtain data that is useful for finite element model validation.

The average peak angular speed for the high-speed tests was 41.8 rad/s and the average peak angular speed for the low-speed tests was 22.0 rad/s. The peak angular speed only varied by 10% between similar tests. The motion of the brain lagged behind that of the skull, producing a relative displacement of the brain with respect to the skull. The magnitude and primary direction of the relative displacement was dependent on the location at which it was measured. The location of the radiopaque target with respect the anatomical coordinate system and bony landmarks of the skull are both important in determining the characteristics of the relative displacement profiles. The high-speed tests produced an average displacement of +/-5 mm, while the low-speed tests had an average displacement of +/-2.5 mm in the X-direction. Intracranial pressure (ICP) was also measured at two points in the cranial cavity, and showed the delayed response of the brain to the rotational loading of the head.

[1a] M. Faul, L. Xu, M. M. Wald, and V. G. Coronado, "Traumatic brain injury in the United States: emergency department visits, hospitalizations, and deaths," Atlanta (GA), 2010.

Dedication

I would also like to dedicate this to my grandparents, Alvin and Esther Hinnenkamp and

Barbara Guettler. They were my first friends and teachers, and I miss them every day.

Table of Contents

List of Figures

List of Tables

Introduction

It has been reported that there are approximately 1.7 million traumatic brain injuries (TBIs) in the United States every year, and of those 1.7 million, 52,000 result in death [1]. The report states that motor vehicle accidents are the second leading cause of TBI in the US, and the leading cause of TBI-related deaths between 2002 and 2006. A report by the World Health Organization (WHO) from 2015 stated that there are more than 1.2 million road deaths globally each year. While the total number of traffic injury deaths has plateaued in recent years, traffic-related injuries remain the leading cause of death in people ages 15-29 [2].

While considerable study has been devoted to understanding the physiological mechanisms and biomechanics of TBI, there is still a lot to learn about how the brain responds to different loading scenarios of the head. While many tests have been conducted to examine the response differences associated with linear and angular kinematics. Several studies have determined that angular inputs (angular speed and duration) are important correlates for brain injury.

Current regulations use the Head Injury Criterion (HIC) to mitigate head injury during MVCs. The criterion (Equation 1) is based on the resultant linear acceleration of the center of gravity (c.g.) of the head, and is a measure of the average change in kinetic energy of the head [3]. While HIC is a good metric for head injury involving head contact, TBI and TBI-related deaths are still prominent in MVCs. This elucidates two possible problems with current regulation: first, that HIC is not identifying all possible TBI, or second, that the regulatory tests do not identify all modes of injury.

$$HIC = (t_2 - t_1)\left[(t_2 - t_1)^{-1} \int_{t_1}^{t_2} a(t)dt \right]_{MAX}^{2.5} \qquad (1)$$

In 1985, Ommaya recommended a combined metric so that rotational input was included in addition to contact and linear acceleration [4]. However a temporal component is necessary for identifying potential injury. Ommaya recommended a two-step scale based on angular speed which had high-speed (above 30 rad/s) and low-speed (no more than 30 rad/s) categories. In both categories, peak angular accelerations above 4500 rad/s^2 would be classified as AIS 5 injuries. In the high-speed category anything below that would be considered AIS 0 or 1, whereas in the low-speed category there are three levels of AIS definition.

The Brain Injury Criterion (BrIC) was developed to include an angular speed-based metric [5]. Angular speed in all three planes relative to their critical values are included in BrIC (Equation 2). Each critical value is set so that a BrIC of 1 corresponds to a 50% probability of AIS 4+ injury.

$$BrIC = \sqrt{\left(\frac{\omega_x}{\omega_{xC}}\right)^2 + \left(\frac{\omega_y}{\omega_{yC}}\right)^2 + \left(\frac{\omega_z}{\omega_{zC}}\right)^2} \qquad (2)$$

While experimental models have provided insight into how the brain responds to various loading scenarios, experiments are expensive and time-intensive. Thus, finite element (FE) modeling has become a large part of the impact/injury biomechanics field. There are many existing finite element models of the human head. The Simulated Injury Monitor (SIMon) is one of the simplest models, and was developed to investigate injury metrics for diffuse axonal injuries (DAI), subdural hematoma, and contusions or focal lesions [6]. The simplicity of this model leads to computation of these three injury metrics with relatively short computation times. The Global Human Body Model Consortium (GHBMC) head model has a detailed model of the brain, including differences between white and gray matter, as well as several specific structures [7]. The Royal Institute of Technology (KTH) model has several iterations. The first has

isotropic material properties [8], and the newer model has anisotropic material properties based on the white matter tracks in the brain [9]. Other models include the Total Human Model for Safety (THUMS) [10], the Worcester Head Injury model (WHIM) [11], and the Louis Pasteur University (ULP) head models [12].

These models require very little cost, and save time while having the potential to provide more and different information than could be observed in any experiment. However useful FE models are, they must be validated under a variety of conditions and loading scenarios to provide meaningful insight into biomechanical responses. Additionally, the historical data used to validate and evaluate FE models were not developed with the intent of model validation [13−15]. The nature of the historical data has led model developers to select specific data sets to use for model validation and evaluation. This process has led to inconsistencies in definition of validity of each of the different FE models. In efforts to combat this, Giordano and Kleiven developed standardized methods for model validation [16]. The study developed a selection process for experimental data, a systematic way for comparisons between experimental and simulation data, and a biofidelity ranking. Experimental data was selected and used if it met accuracy, reproducibility, and redundancy standards. The authors stated that this systematic approach would lead to a more consistent definition of validation between models by limiting subjective selection of experimental data for validation. The produced methodology would not be necessary if scalable brain response data were available. With scalable response data available, the same data sets could be used for validation of every FE model. Therefore, repeatable and scalable experiments need to be conducted to create corridors and serve as validation references for FE models. This is especially important for the brain, which has limited data available for validation and is a dominant injury in MVCs.

The goal of this study is to determine how the brain responds to rotation of the head with no impact using high-speed biplane x-ray. Additionally, methods were developed to reduce and limit experimental variation by controlling the exact placement of brain targets for brain motion measurements, and creating a test input that would not vary based on specimen characteristics.

Literature Review

Brain-Skull Kinematics

Motion of the brain within the skull has been of continuing interest. In 1946, a study was done using Macaque monkeys fitted with Lucite calvaria to quantify the motion of the brain during impact of a 200-gram projectile. Movement of the sulci were measured over time. "Gliding" movements of the brain varied by brain region, and existed mostly in impacts with rotation in the sagittal or horizontal planes. One test compared brain response with and without cerebrospinal fluid (CSF). The tests with no CSF had more movement and a longer period of oscillation—that is, the CSF (and resulting intracranial pressure) act to dampen the response of the brain tissue to impact [17]. Later, a study on adult Rhesus monkeys removed the dura mater and replaced the calvaria with polycarbonate to monitor the movement of the brain within the cranial vault. During impact, high accelerations cause the brain to move separately from the skull. Upon analysis of the brains, damage and injury occurred where the brain and brain stem met the skull [18]. While these studies elucidated some important factors in the response of the head to impact, the removal of the calvaria and dura compromised the tethering of the brain to the skull, and gliding motions between the cortex and the skull were likely artifact of the loss of tethering.

In 1966, Hodgson et al. impacted the heads of anesthetized dogs to observe the movement of the brain resulting from impact. During each test, the dog's head rested on an x-ray

cassette with its mandible fixed. Three lead wires were implanted to quantify motion during the test. Pulsed x-ray showed a change of orientation between each of the three wires, suggesting that shear strain existed in the brain [19]. Radiopaque media has been used to quantify brain movement via a high speed camera and "flash x-ray cinematography" [20]. Rhesus monkeys were injected with radiopaque media through a catheter in the left internal carotid artery. Movements of the cerebral vasculature relative to the test apparatus were measured for each impact test. Each test showed initial depression of the skull followed by high frequency oscillation of the vessels relative to the skull, which eventually decreased in frequency [20].

X-ray cinematography has been used measure motion of the brain relative to the skull. Impact tests to PMHS heads showed that the brain can move relative to the skull (imperfectly coupled) during impact [21]. By calculating effective mass of the test subject, it was determined that the entire mass of the brain is not immediately loaded during impact. Specimens that were successfully pressurized resulted in strain-related tissue damage, which was considered to be a more biofidelic response. It was noted that any impacts that caused skull fracture greatly affected the kinematic response of the PMHS heads.

In 1997, Hardy et al. used a high-speed biplane x-ray system and neutral density accelerometers (NDAs) to measure deformation of the brain and its displacement relative to the skull during impacts on inverted, aCSF (artificial cerebral spinal fluid) perfused PMHS heads [22]. Kinematics of the skull were measured with a nine accelerometer array fixed to the skull. Kinematics of two locations in the brain were measured using tri-axial NDAs, which were validated by motion tracking. The data showed that the brain moved relative to the skull at a magnitude related to the impact severity. The brain data showed a lag in response to impact as well as evidence of a damped response. Additionally, radiopaque markers called reduced density targets (RDTs) were inserted into the brain. Stretch between markers was calculated to range

between 5 and 7 percent at lower severities [22]. These data were later used to validate a finite element model [23]. Another study measured relative motion of the brain with respect to the skull using accelerometers implanted in the brains of three PMHS during six impacts. However, in this study the accelerometers moved through the brain during the tests [24]. Later, Hardy et al. conducted another test series for which high-speed biplane x-ray was used to measure the relative motion of various locations of the brain with respect to the skull [14]. Larger, neutral density targets (NDTs) were implanted in two columns: one anterior and one posterior. Target motion was reported with respect to a body-fixed basis. Targets followed a figure-eight pattern, of which the direction of the major axis changed based on depth and fore-aft position within the brain. Impacts of similar severity to the previous study [22] caused relative brain displacement of +/-5 mm [14]. Subsequently, the NDT motion data from these tests were analyzed to separate the motion into rigid body displacement and deformation. Deformation increased as the impact severity increased [25].

In a newer study, NDTs were implanted in two clusters, typically in coup/countercoup positions. PMHS heads were impacted in the median, coronal, and horizontal planes [15]. Targets nearer the center of gravity of the head had less relative motion and strain than targets farther from the CG. Additionally, target motion patterns were similar for all three impact directions; however, horizontal and coronal impact response was affected by the proximity of the targets to the flax cerebri. Both the 2001 and 2007 Hardy studies showed that relative displacement of the brain was best correlated to angular speed [14,15]. The 2007 study showed that average maximum principal strain was correlated to angular speed.

In 1990, a study compared the response of three physical surrogate head models to angular acceleration loading. Three models were used: two of non-human primates (with and without a falx), and one human skull with a falx. The model skulls were subjected to angular

accelerations in the coronal plane. The study determined that shear strain patterns in the gel brain models were positively correlated with angular acceleration [26]. This corroborates an earlier paired-study that looked at physical symptoms and neuropathological damage in relation to applied angular acceleration in non-human primates. First, 53 monkeys were subjected to a controlled 60° sagittal rotation over a varied duration of 10-20 ms [27, 28]. An experimental trauma severity (ETS) scale was developed to determine the severity of damage to physiological and cognitive function. A strong positive correlation was found between angular acceleration and ETS. For the lowest severity tests, blood pressure or heart rate might have been disturbed, but for the highest severity tests, immediate death and gross damage to the brainstem were potential outcomes [27]. Neuropathology trends included 23 subdural hematomas, which occurred mostly in grade 4 or 5 animals, and contusions in the frontal and temporal lobes in 39 of the 53 animals [28].

More recently, two studies have used magnetic resonance imaging (MRI) to quantify movement and deformation of the brain on human volunteers. The first used controlled drops from flexion to a neutral spine configuration in 5 volunteers, and focused on the cerebellum and the brain stem [29]. The study noted that during slow movements, the cerebellum rotated with respect to the skull, and the brain stem displaced caudally through the foramen magnum due to tension in the spinal cord. In the second, through controlled, mild acceleration occipital impacts on human volunteers, it was noted that due to adhesions and bony structures around the base of the brain, rotation of the brain can occur even during linear input [30]. Along with this rotation, strain develops as part of the brain compresses against the skull and another part is pulled away from the skull. It is unlikely that these findings hold for impact of an incompressible system.

Frontal impacts of PMHS heads demonstrated that intracranial pressure is at its maximum near the impact site and decreases posteriorly throughout the brain until it is negative at the

countercoup site [13]. These pressure changes occur before the head begins rotating. In a second series of tests, one PMHS was subjected to several impacts, removing human variability. Peak pressure was found to be linearly related to the peak linear acceleration of the head. No quantification of skull deformation was made, so it is unclear if global deformation of the skull caused the pressure profile. In finite element simulations performed as part of the study, stress produced by skull deformation was neglected so that simulated intracranial pressures were due only to the differential motion of the brain and skull.

The positive correlation between linear acceleration and coup pressure was again shown in isolated head impact tests [15]. The rate of pressure increase was also found to be positively correlated with linear acceleration while the duration of the pressure pulse was inversely correlated with linear acceleration. Angular acceleration did not have a significant effect on any pressure parameters [15].

A study comparing PMHS to both anesthetized and post-mortem Rhesus monkeys showed via high speed x-ray that the skull deforms during impact, and that this deformation (without fracture) can cause injury. Additionally, epidural pressure was measured and was identified as a response related to the skull acting on the brain, followed by the brain transferring energy to the skull later in the event. This study also emphasized the importance of pressurizing PMHS to maintain biofidelic response [31].

Finite Element Models

Due to the prevalence of TBI in motor vehicle collisions as well as falls and sports, developing a validated finite element model of the brain has long been of interest. In 2001, several studies were used to validate improvements made on the Wayne State University Brain Injury Model (WSUBIM) with pressure, brain motion, and facial impact data [32]. Additional

tests from the Nahum test series [13] were used to validate ICP (intracranial pressure) response, in addition to ICP and ventricular pressure data from the Trosseille tests [24]. Relative brain motion response was validated using the 2001 Hardy et al. study [14], and displacement of the markers in tests with mostly linear acceleration was compared to tests with higher rotational acceleration components. The tests with higher rotational accelerations caused for higher displacements of the targets relative to the skull. Overall the study highlighted the importance of accurate material models for specific brain structures and the importance of the contact definition between the brain and skull [32].

In 2002, Nahum's intracranial pressure data [13] and Hardy's brain-skull motion data [14] were used to develop and validate a scalable FE model [33]. The study determined that the stiffness of the brain material had a large effect on the relative displacement of the brain within the skull. A stiffer material would produce lower displacement, while a more compliant material would produce displacements larger than the experimental data. When comparing the maximum principle strain between stiff, average, and compliant materials, a similar trend was found, where the stiffer material produced lower strains than the average one. However, simulated intracranial pressure was largely dependent on the type of contact defined between the brain and the dura mater/skull [33].

In 2003, Takhounts and colleagues developed the SIMon model (Simplified Injury Monitor) [34]. SIMon is a basic brain model developed to determine injury probability during impact, and requires a relatively short computation time. SIMon contains a rigid skull, a dura and CSF layer, the brain, falx cerebri, tentorium cerebelli, and parasagittal bridging veins. Specific regions and structures of the brain are not specifically modeled. Material properties were determined using experimental data from one NDT test [14]. Once the material properties for all components were defined, the remaining NDT data from the 2001 Hardy study were used

to validate the model. Injury metrics were related to the model by scaling to animal studies. The injury metrics included were the cumulative strain damage measure (CSDM), the dilatation damage measure (DDM), and the relative motion damage measure (RMDM). These metrics correlate to diffuse axonal injury, contusions, and acute subdural hematoma, respectively [34].

Methods

Motion of the brain with respect to the skull of two post mortem human surrogates (PMHS) was measured during controlled angular speed pulses. High-speed biplane x-ray was used to record the motion of radio-opaque targets on the skull and in the brain. The brain was perfused to 10.3 kPa with aCSF to remove gases from the cranial cavity and replicate *in vivo* conditions. In addition to displacement, ICP was measured by two pressure transducers inset slightly from the inner table of the skull. Rotation was restricted to the median plane and occurred about the occipital condyles (OC.)

The first series, NDTA, tested the first PMHS four times at 40 rad/s and 30 ms. The second series, NDTB included five tests: four at 20 rad/s in 60 ms, and one at the same speed as NDTA (Table 1.) While NDTs were not used in this study, naming convention of the tests follows that of the funding source.

Table 1. Test matrix for both test series. *Test does not have x-ray data.

Test ID	Angular Speed (rad/s)	Duration (ms)
NDTA-T1*, NDTA-T2, NDTA-T3, NDTA-T4, NDTB-T4	40	30
NDTB-T1, NDTB-T2, NDTB-T3, NDTB-T5	20	60

Specimen Preparation

Two fresh, never frozen PMHS head-neck specimens were obtained from the body donor program at The Ohio State University. The neck was separated from the body below the seventh cervical vertebra (C7) to ensure the preservation of the vasculature in the neck before transport. Specimens were obtained within 3 days post-mortem and were tested within 7 days of death. With proper perfusion and cooling of the head, degradation is limited after the first 24 hours through the first week post-mortem. Characteristics of both PMHS are in Table 2.

Table 2. Specimen Characteristics

	SM147	SM149
Test Series	A	B
Sex	Male	Male
Age	58	51
Stature (cm)	183	185
Mass (kg)	82.5	55.9

The right and left common carotid arteries and internal jugular veins were dissected from the flesh of the neck. Polymer compression fittings were attached to each vessel. The vertebral arteries were identified and left patent for evacuation of gases and fluid return during perfusion (Figure 1.) A length of the spinal dura was separated from the inner surface of the vertebral canal and the cervical spine was removed below C3 in Series A and above C3 in Series B. After the inferior cervical vertebrae were removed the dura that had been separated from the vertebral canal remained with the specimen. One to two inches of the spinal cord was transected from the subdural space and a barbed fitting was fixed to the dura. Tygon® tubing was mated to each

compression fitting, as well as the barbed fitting on the dura. The opposite end of each Tygon®

tube was fitted with a quick-disconnect coupling. Artificial CSF was used to flush and perfuse

the subdural space and vasculature. As aCSF was pushed through each fitting, any leaks caused

by compromised vasculature were dissected out and ligated. The head was pressurized

throughout specimen preparation to maintain integrity of the vasculature and neural tissues.
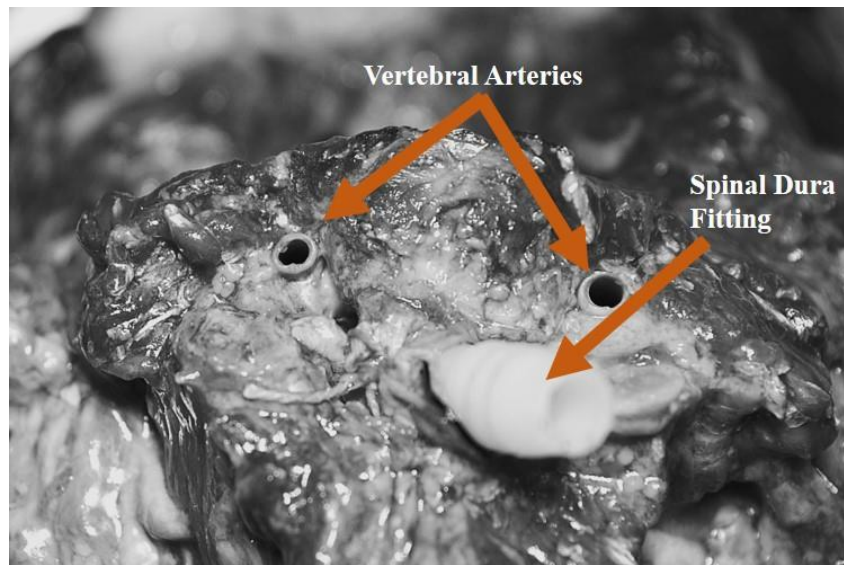
Figure 1. Inferior view of the vertebral column with the vertebral arteries left patent. Also shown is the barbed fitting tied to the spinal dura.

Excess tissue was removed to facilitate instrumentation and mounting of the specimen to

the test fixture. The mandible was cut inferior to the temporomandibular joint and removed for

access to the hard palate, which was used as a point of fixation to the test apparatus. The soft

tissue of the anterior of the neck was removed, excluding the perfusion vasculature. The scalp

was completely removed for skull marker placement, target deployment, and transducer

installation.

The head specimen was mounted to a custom-designed head cradle, which rigidly coupled the specimen and the driving axle of the test device. The cradle consisted of independent right and left sides, which were connected by bridging pieces that were machined for each specimen, allowing for specimens of slightly different sizes to be accommodated. The mounts fixed the specimen to the cradle via connections to the hard palate and occiput. The right and left sides of the cradle each had a pillow block that mated to an axle. The pillow blocks were designed to be adjustable so that the axles could be aligned with the centroid of the OCs. The left cradle axle mated to the main drive axle of the test device. The main axle was directly connected to and driven by a pinion gear that was rotated by the follower mechanism, part of which was a gear rack. An angular rate sensor (ARS) was mounted to one side of the head cradle for measurement of the test pulse. All parts of the head cradle were made of aluminum, which is largely radiolucent, so that the brain targets were still visible with x-ray throughout the rotation.

Several steps were required to fix the specimen to the mounting locations on the head cradle. The nasal cartilage, vomer, and nasal conchae were all removed from the nasal cavity; the soft palate was also removed. Three holes were drilled through the hard palate, and threaded inserts were held inside the nasal cavity through those holes. A fourth threaded insert was potted in the anterior opening of the nasal cavity to provide an anterior fixation point. With the threaded inserts in place, radiolucent dental cement was used to fill in the nasal cavity. The dental cement was allowed to harden for several hours. A right-angle maxilla mount (bridging piece) was attached to the skull via one bolt anterior to the nasal cavity, and three that were secured into the threaded inserts through the hard palate. Aluminum screws were used so that they would not block the x-ray beams. Part of the ethmoid cartilage was removed from the ethmoid sinus so that the nasal cavity could be filled completely. Two holes were drilled in the occiput near the nuchal

ridge. Helicoil® thread inserts were placed such that the occipital mount could be fixed to the head. Once the mounting brackets were fixed to the head, the brackets were bolted to the right and left pieces of the head cradle. The final attachment of the head cradle is in Figure 2.
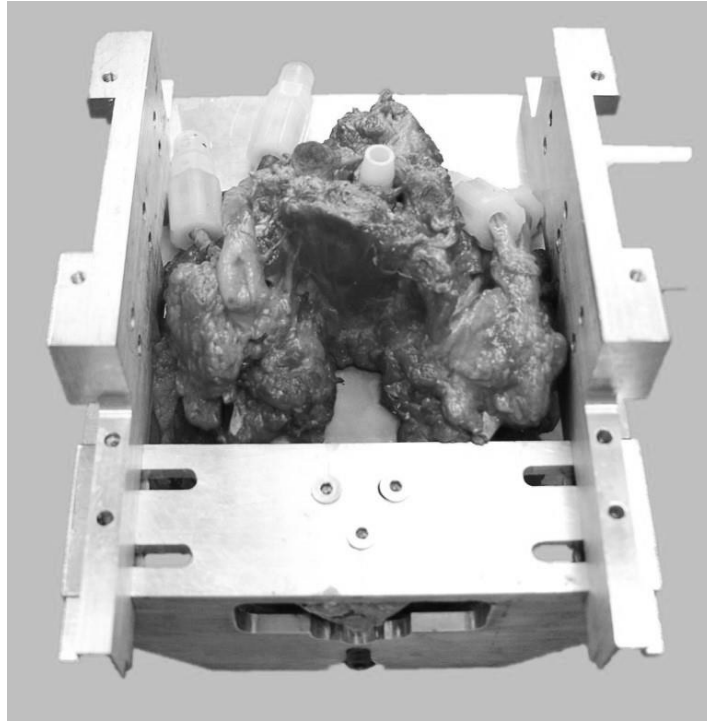
Figure 2. Inferior view of the specimen in the head cradle. Anterior is at the bottom of the image. Compression fittings on the vasculature as well as the barbed fitting in the spinal dura are visible.

Once the head was fixed in the cradle, the pillow blocks were adjusted so that the center of rotation would align with the approximate centroid of the occipital condyles, as stated previously. The pillow blocks were set so that both axles were aligned.

Kinematics

Kinematics of the head were measured on the head cradle since measurement of rotation is independent of measurement location, and the head was rigidly fixed to the head cradle itself. One angular rate sensor (DTS ARS Pro) was mounted to the right pillow block. A head specimen

fixed in the head cradle with the pillow blocks set and kinematic instrumentation in place is in Figure 3.
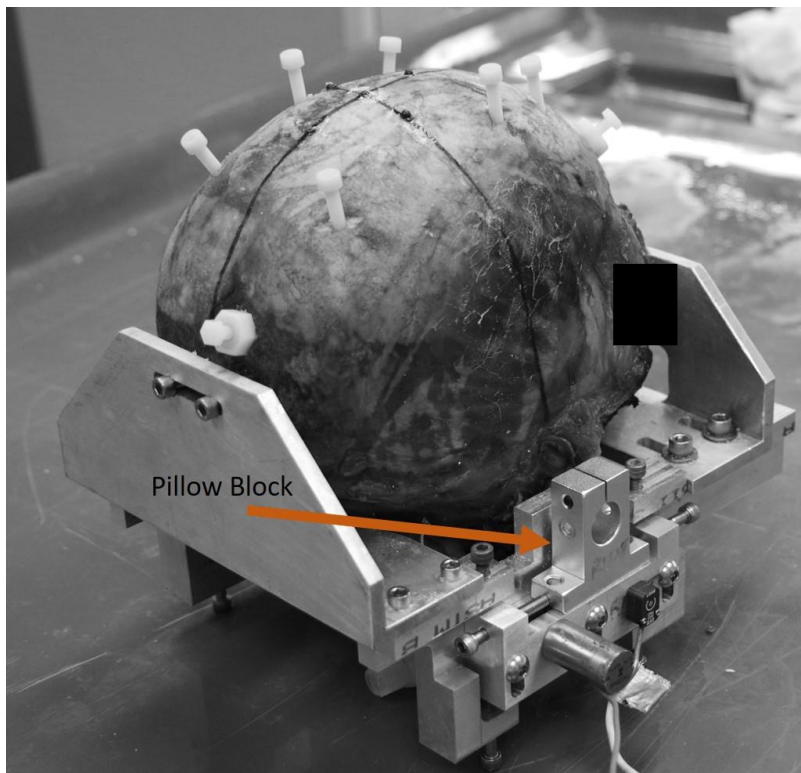
Figure 3. Head specimen in cradle with pillow blocks set

Brain Targets

The brain targets were 1.5-mm diameter tin granules. Tin was used because it has similar x-ray absorption properties to gold and lead, while far less dense. Previous studies have used neutral density targets (NDTs) where the tin targets were encapsulated in polystyrene tubing to make each target's density similar to that of brain tissue with the idea that the targets would not move through the tissue if they were of equal density [14,15]. However, it was found that ultimately the low mass of the targets was the critical factor to keeping the targets from moving. Encapsulation of targets also increases the volume of brain tissue being displaced, so forgoing the capsules is beneficial in this way as well. Therefore, the tin granules were implanted without

the polystyrene capsules. A collection of some granules (1-mm diameter) is seen in Figure 4, although slightly larger, 1.5-mm diameter granules were used for these tests.

Figure 4. Collection of tin granules made to be used during tests.

The head in the cradle was placed on a stereotactic frame designed for accurate deployment of the radio-opaque targets. The frame facilitates five degrees of freedom in the deployment cannula. The frame (Figure 5) allows for translation of the cannula in the sagittal and coronal planes as well as rotation within these planes. Finally, the depth of target deployment (z-direction) can be determined using a scale fixed to the cannula.
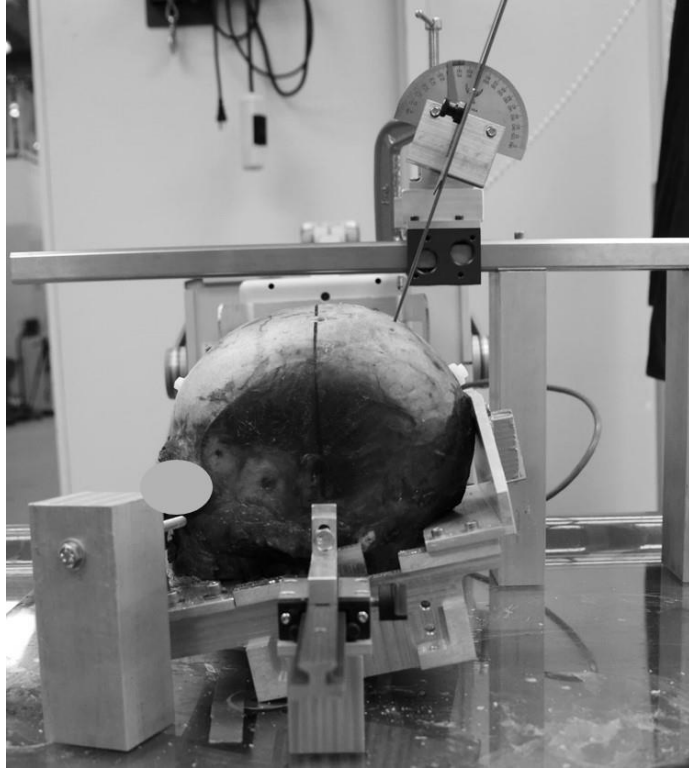
Figure 5. PMHS 1 in the stereotactic frame

The frame pins the head at the external acoustic meatuses (EAM) and the angle of the head can be adjusted so that the Frankfort plane is parallel to horizontal (i.e. the head was held in anatomical position.) Two schemes to determine target locations were used on each head. The target deployment schemes were pre-determined so that they were repeatable, reproducible, and scalable. To determine target deployment locations, four measurements of the skull were taken, some of which are shown in Figure 6. The width was measured at the maximum width of the head. The height was measured perpendicularly from the Frankfort plane to the apex. The length of the head was split into anterior and posterior lengths: from the EAM to the nasion and to the occiput, respectively. Dimensions for both subjects can be found in Table 2. The same scheme was used for both test series, NDTA and NDTB, however an additional column of targets was implanted in the right hemisphere in SM149.
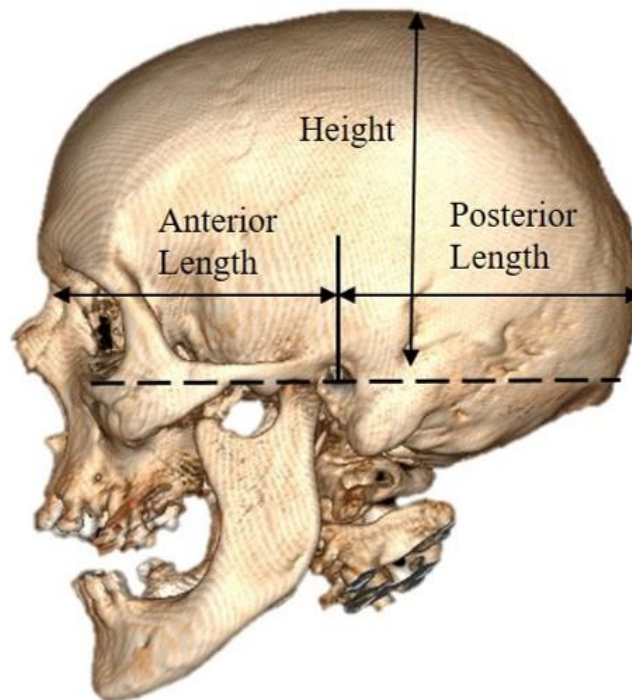
Figure 6. Measurements made on each skull.

Table 3. Specimen Measurements

Parameter		SM147	SM149
Height	mm	121.4	115.9
Width	mm	136.0	147.0
Anterior Length	mm	100.0	90.49
Posterior Length	mm	90.87	101.6

Series A

The linear grid scheme has 3 columns (seen in Figure 7.)The most-anterior column is 2/3 the distance from the EAM to the nasion, the middle column is 1/3 the distance from the EAM to the nasion, and the posterior column is 1/2 the distance from the EAM to the occiput. To define rows, the apex height was divided into sixths. The middle and posterior columns have targets at 1/3, 1/2, 2/3, and 5/6 the distance from the apex to the EAM, and the anterior column has targets and 1/3 and 1/2. Laterally, the middle and posterior columns are 1/4 of total head width away from the midline, while the anterior column is 1/6 of the total width from the midline. The radial scheme in the left of Figure 7 has 3 "columns" of targets that radiate from the reference coronal plane (from EAM to skull, perpendicular to the Frankfort plane.) The columns are at -20, 0, and 20 degrees with respect to that plane. The "rows" are 2 and 4 cm deep to the external table of the skull. Laterally, the radial targets are half the distance from the midline to the side of the head.
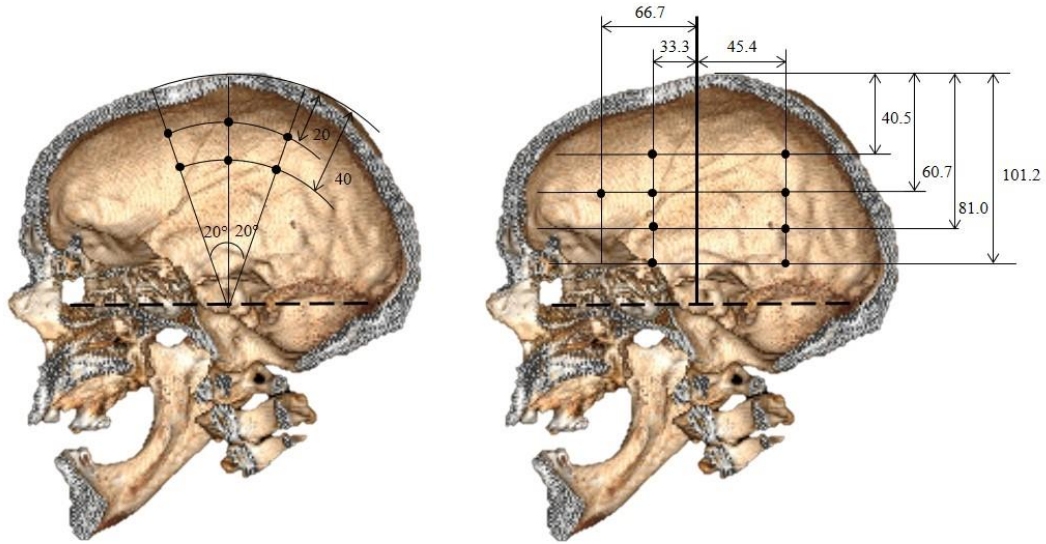
Figure 7. Ideal target locations (in mm) in NDTA based on the radial (left) and linear grid (right) target schemes.

To create the body-fixed basis for brain motion, two clusters of five 3-mm lead markers were attached to the skull: one at the apex and one on the left side. In addition to providing a means of creating a body-fixed basis, these targets serve as a check for data analysis, as they are on a rigid body and have exact known locations. If during data analysis the skull markers appear to move relative to the body-fixed basis or each other, something could be wrong with distortion of the image or the definition of the target positions.

Targets were deployed through a cannula fixed to the stereotactic frame and inserted using a stylet once the cannula was at the correct depth. Plain-film digital x-rays were taken at each stage of the implanting process to ensure correct target placement. Once all the targets were implanted, the holes in the skull were plugged with nylon screws (Figure 3) so that aCSF would not leak and pressure could be maintained throughout testing. An x-ray was taken of the final

placement of the brain targets as well as the placement of the skull markers at the apical and temporal regions (Figure 8.) It is important to note that while this specific image shows air in the head (at the apex), there was no air in the head during target deployment or the tests themselves.
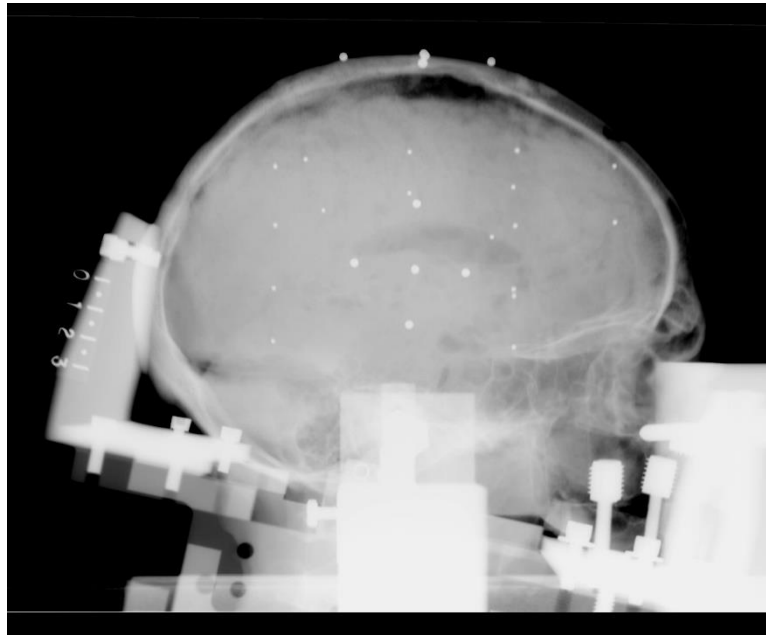
Figure 8. Plain x-rays of final brain target deployment and skull target fixation in Series A.

Series B

Series B used the same target location scheme as Series B, with a few modifications (Figure 9.) Due to differences in specimen anthropometry, the deployment scheme was scaled to the dimensions of PMHS 2. That is, the linear grid scheme maintained the same levels (1/3, 1/2, 2/3, and 5/6) of the total height of the head, and the depths of the targets of the radial scheme were scaled by apical height, so that the deployment depths were 19.1 and 38.2 mm from the surface of the skull.

A few other changes were made in addition to scaling. The first was the omission of the anterior target at 1/3 the apical height. This target dislodged before testing began in Series A, so

it was left out in Series B. Second, a fourth column of targets was added in the linear grid scheme. The additional column was aligned with the meatus and had seven evenly spaced targets (depths of 5/12, 7/12, and 3/4 of the apical height were added to the depths used in the other columns.) Finally, four additional lead markers were placed on the on the left side of the skull.
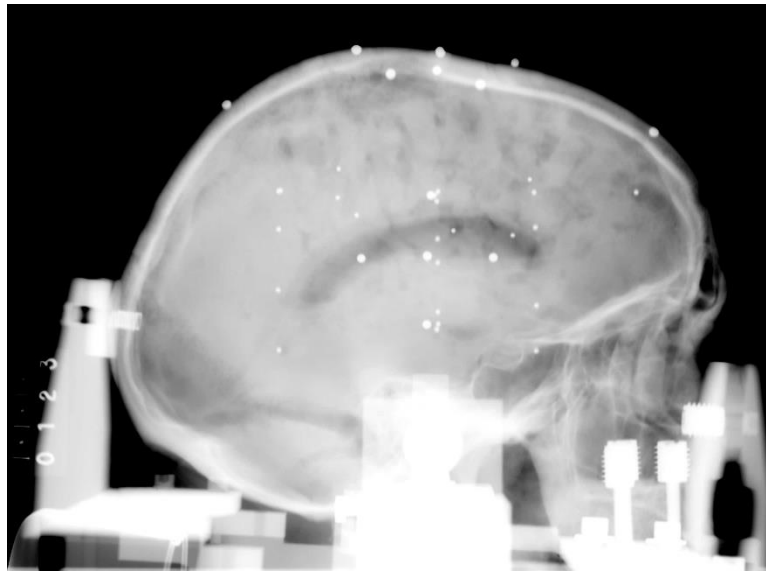
Figure 9. Plain x-ray of the brain and skull targets in NDTB.

Intracranial Pressure

Intracranial pressure was measured in two locations using Endevco 8530C pressure transducers with a full scale output of 689 kPa (100 psi). The threads on the pressure transducers ended about 3.5 millimeters from the sensing diaphragm. With such a long distance, very few threads would engage with the skull while aligning the sensing element with the inner table of the skull. Therefore, threaded adapters were needed for secure mounting of the pressure transducers. Holes were drilled through the central axis of nylon hex-head screws. The holes were then threaded so that the pressure transducers could be tightened into place. The length of the screw was cut so that it matched the length of the transducer.

Trephines (holes) were drilled and tapped in the frontal and occipital bones on the right side of the skull. The transducer adapters were threaded into the holes. Nylon screws were tightened into the adapters to seal the wholes until the transducers were inserted before the tests. Figure 10 shows the frontal and occipital pressure transducer adapters installed during specimen preparation.
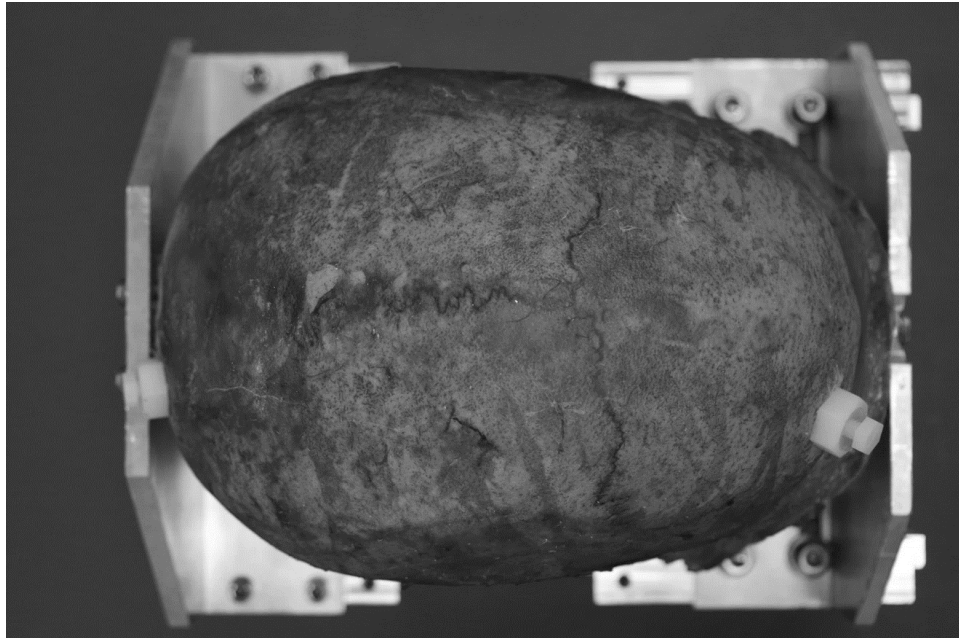
Figure 10. Specimen mounted in the head cradle with both pressure transducer adapters installed and plugged with nylon screws.

Data Acquisition

A high-speed biplane x-ray system was used to record movement of the skull and brain targets throughout the test. The system includes two x-ray head and image intensifier pairs with Phantom v9.1 monochrome high-speed cameras mounted on the image intensifiers. The x-ray system is non-gated (i.e. it produces x-rays continuously). The aperture of the camera lenses was completely open (f-stop = 1.4) and set to infinite zoom (parallel light is emitted from the output of the image intensifiers. The cameras were operated at 1250 frames per second (800 µs interval)

with an exposure time of 100 µs to prevent blurring of the images. The x-ray images had a resolution of 1200x1200 pixels and 14-bit depth.

Kinematic and ICP data were recorded on a DTS TDAS Pro sampling at 20 kHz. A Phantom v9.1 high speed camera was used to record the event. All three high-speed cameras were synchronized using the TDAS system, which was used to drive LEDs that were placed in the view of all three cameras.

After the tests, a FARO scanner was used to collect location data of the 10 skull targets as well as the right and left acoustic meatuses, infraorbital notches, and occipital condyles. The points are within an arbitrary user-defined three-axis coordinate system. These points were used to define the Frankfort plane, create the coordinate axes, and transform data to a body-fixed basis at the occipital condyles. The body-fixed coordinate system followed SAE J-211 standards—an inverted, right-handed system. That is, x is positive from posterior to anterior, y is positive from left to right, and z is positive from superior to inferior. The origin of the body-fixed basis was on the midline between the EAMs.

Data Processing

TEMA® motion tracking software (TEMA, Image Systems, Linköping, Sweden) was used to determine 3D coordinate system from the biplane videos, as well as to determine the position of each target frame-by-frame. First, each x-ray video had to be corrected for distortion created by the optics in each image intensifier. Post-test distortion correction images were taken using panels, with custom grids with lead BBs 10 mm apart. Additionally, calibration images were taken of a calibration cube placed within the test setup.

X-ray images of the calibration cube were used to determine the position of the slave camera relative to the master view. The calibration cube has 24 radio-opaque markers, the distances between which are known. Each point is labeled in both camera views in the TEMA motion tracking software. The distance between two points was defined, and a best-fit relative position (in six degrees of freedom) was created. For each test file in TEMA, the calibration parameters were input to link the tracking data from each view and create an arbitrary global coordinate system. Target motion data were filtered using pseudo-CFC 30 Hz, while the angular velocity and pressure data were filtered using CFC 60 and CFC 180, respectively. Angular acceleration was calculated from the angular velocity data from each test.

The normalized root mean squared deviation (NRMSD), seen in Equation 3 [35] was used as a metric for preliminary comparison of test pulses and the relative brain/skull displacement measured in each test. The average angular speed at each time point was calculated and used as the reference curve for each NRMSD calculation. The same was done for displacement measured at each target location and in each direction of displacement.

$$NRMSD = \frac{1}{Y'_{max} - Y'_{min}} \sqrt{\frac{\sum_{i=0}^{n}(Y_i - Y'_i)^2}{n}} \tag{3}$$

Test Setup

Two test series were conducted using two half-sine angular speed profiles: 40 rad/sec with a 30 millisecond duration, or 20 rad/sec with a 60 millisecond duration. Four tests were conducted at the same speed on one specimen (only three include x-ray data). Five tests were conducted on the second PMHS head specimen using both speed profiles.

Test Apparatus

Since the ultimate goal of these tests is to contribute to corridors for brain-skull relative motion during a rotational event, the energy input (i.e. the angular speed pulse) needed to be predictable and repeatable between tests – within tests using the same specimen and between tests on different specimens. To this end, an "extreme energy" device was used so that the input pulse would not be affected by the mass of the specimen. The test apparatus is made up of two main parts: a driver and a driven section Figure 11.

The driver was made up of a motor-driven flywheel, cam, follower, and actuator (Figure 11). The 320-kg flywheel and the cam were driven by a 2-HP motor. The rotational speed of the flywheel and cam were controlled by adjusting the gear ratio between the motor and the drive axle. The cam had a 180° lobe cut to produce the desired half-sine angular speed pulse. The driven section (Figure 11) was primarily composed of the follower and main driving axle that rotated the head specimens. The follower interacted with the lobe of the cam during the test, and rotated the main axle via a rack and pinion gear set.
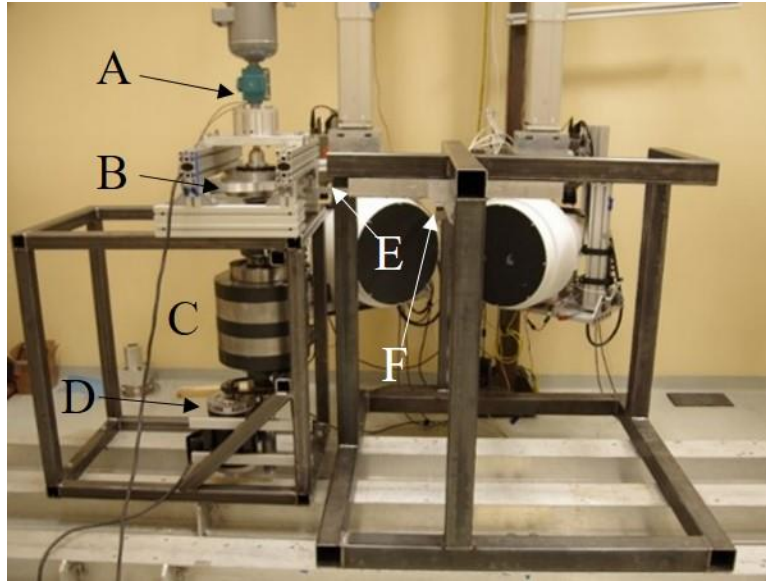
Figure 11. Test apparatus with driving section: actuator (A), cam (B), flywheel (C), and motor (D). The driven section: follower (E) and main axle (F).

The event involved 45-degree rotation of the specimen with 2-inch stroke of the follower. After the event, the follower was locked in place by two catch mechanisms (Figure 12) to prevent additional rotations. The first, a catch pin toward the front of the follower that locked in front of a fin on the top of the follower, preventing forward motion after the initial test event. Second, a pawl gear mechanism was coupled to the main axle, the pawl would lock one of the teeth on the gear to provide a back-up if the catch-pin did not release.
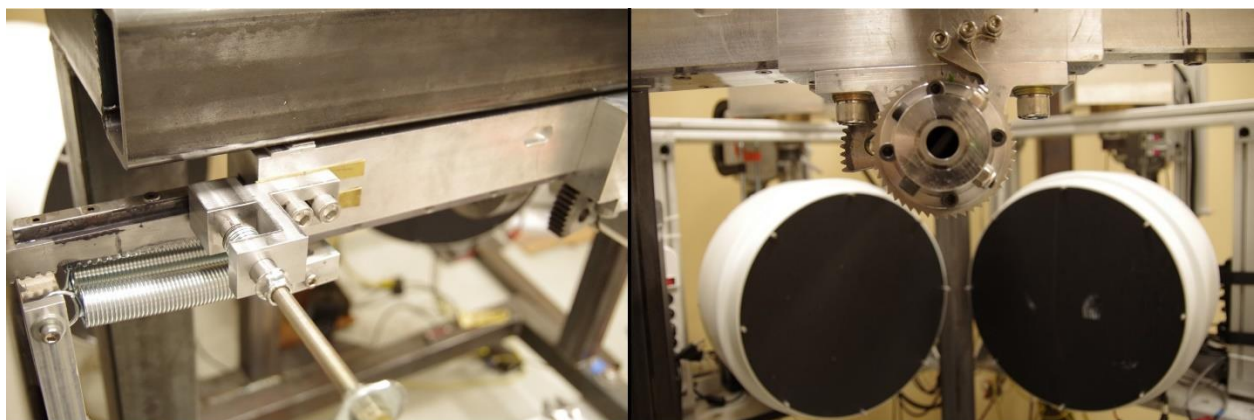
Figure 12. The catch-pin (left) and pawl gear (right) locking mechanisms on the driven section of the test apparatus.

The lobe of was cut to produce a half-sine pulse with a maximum angular speed of 40 rad/s while the flywheel rotated at 1000 rpm (obtaining a 30 ms duration), and 20 rad/s while the flywheel rotated at 500 rpm (obtaining a 60 ms duration). The cam had a base circle fixed to the bottom that had a 4-inch diameter. As the flywheel began to spin, the follower was in contact with the base circle. Once the flywheel was at the desired speed, the actuator was triggered via an optical sensor, and the cam was driven down. With the cam in its lowered position, the follower was in line with the cam and followed the lobe, driving the event. Due to the large amount of energy transferred between the cam and follower, two sets of reaction springs (Figure 13) were installed to maintain contact between the follower and cam throughout the event.
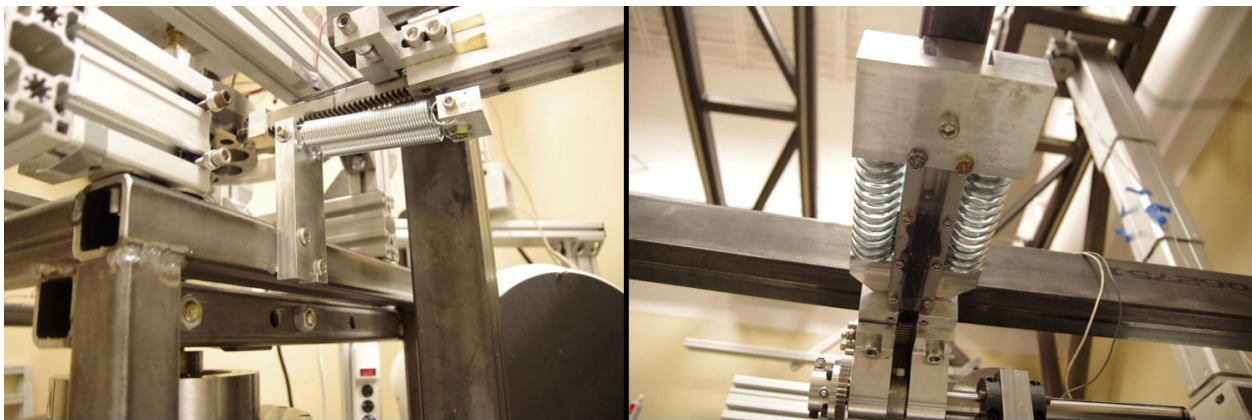
Figure 13. Reaction springs installed to counteract over-rotation caused by the momentum of the head specimens during the tests.

Perfusion System

A perfusion system was used to pressurize the head and re-cycle aCSF throughout the day of testing. A vinyl pool liner was used as a catch basin below the head fixture frame. A drain in the liner fed the aCSF into a pump which circulated aCSF from the catch basin up to a holding tank. The holding tank was kept approximately 1.5 meters above the head specimen to produce a 10.3 kPa (1.5 psi) intracranial pressure. A tube from the holding tank directed aCSF to a 5-outlet manifold which had Tygon® tubing with quick-disconnect fittings at the end for mating with the

fittings on the vasculature on the head. A pressure gauge was connected in series with the spinal dura perfusion line, which could be held at the level of the head to measure the perfusion ICP.

Final Setup

For the PMHS tests, the head cradle was mounted onto the head fixture via the axles on the head cradle. A cradle axle was inserted into the main drive axle and held in place with set screws. The axle on the left side of the head cradle was held in place by a mount on the head fixture frame that did not restrict rotation of the axle. For rotation in the median plane, the head was mounted so that forward rotation occurred in the median plane (about the y-axis).

Once the head was on the fixture, the head perfusion fittings were connected to the perfusion system via the quick-disconnect fittings, and the system was allowed to run for 6-8 hours prior to the first test. Allowing the perfusion system to run facilitated the evacuation of air from the intracranial space so that the brain had the correct conformation and coupling to the skull, forming an incompressible system. A picture of the test setup with the specimen in place (Figure 14) shows the image intensifiers in place (the x-ray heads are just to the left of the image window.)

Figure 14. Complete test setup with head in the testing fixture.

An x-ray image of the head in Figure 15 shows that there was no air in the cranial vault for the tests in Series A. Perfusion was allowed to run to the same point in Series B. Again, the x-ray system was run continuously for two seconds and kinematics data were recorded at 20 kHz.
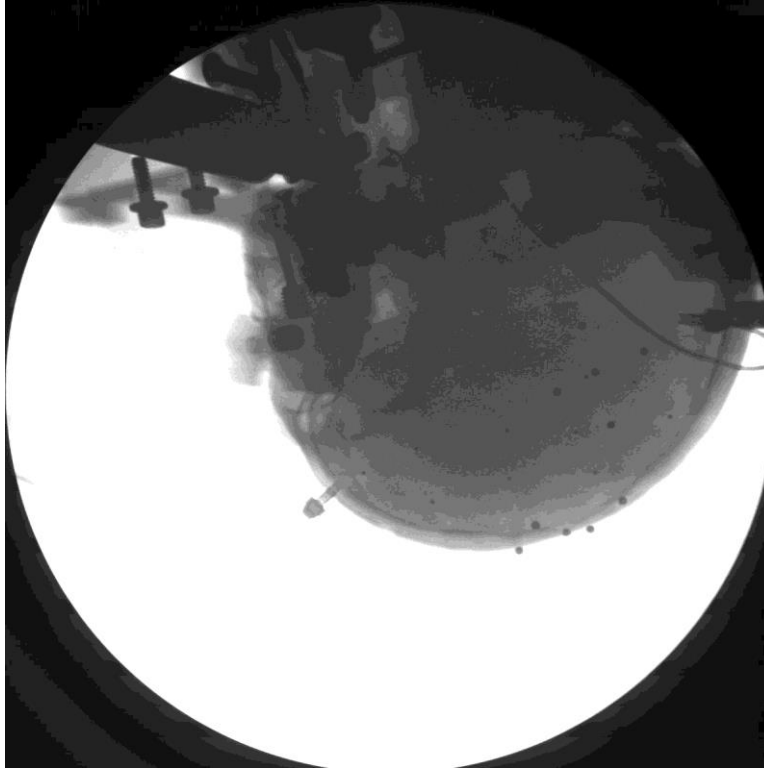
Figure 15. Pre-test x-ray image of the specimen in Series A. All brain and skull markers are clearly seen, and there is no air in the cranial vault.

Results

Two PMHS head specimens were tested under two angular speed conditions to quantify the relative motion of the brain to the skull. The first series, NDTA, consisted of four tests in a high-speed, short-duration test condition. The second series, NDTB, included one test at the same high-speed, short-duration condition, as well as four tests at a low-speed, long-duration condition. All tests measured frontal and occipital ICP, and all but one test measured the displacement of the brain with respect to the skull. Data presented here encompass all of the points which were considered valid and follow expected trends and magnitudes.

NDTA

Four tests with a half-sine angular speed pulse of 40 rad/s and duration of 30 ms were conducted on a PMHS 1. Motion of the brain and skull were quantified using biplane high-speed x-ray in three out of four tests. Relative motion between the brain and skull were quantified, and intracranial pressure was measured in anterior and posterior positions.

Angular Speed Input

Angular speed was measured on the head cradle. The average peak speed of all four tests was 41.2 rad/s (+/- 3.9). The average speed of the tests was very close to the desired peak angular speed. The average positive duration of the tests was 42.1 ms, 40% higher than desired. The peak angular speed and duration of all four tests are cataloged in Table 4. All data were aligned such that the peak angular speed corresponded to 50 ms (Figure 16). The average peak angular speed was 3% higher than the desired peak, while the highest peak angular speed was 45.6 rad/s. The higher speeds were caused by an over-rotation of the head due to momentary loss of contact between the follower and the cam. The over-rotation also produced a negative phase at the end of the speed pulse.

The NRMSD of the angular speed pulse from each test with respect to the average angular speed pulse of NDTA was calculated (Table 4). The average NRMSD was 4.14 %, which demonstrates similarity between test pulses throughout each test (i.e. the magnitude, duration, and phase are similar.)

32

Table 4. Angular speed, duration, and NRMSD from each test pulse in NDTA.

Test ID	Peak Angular Speed (rad/s)	Duration (ms)	NRMSD (%)
NDTA-T1	43.1	41.1	3.65
NDTA-T2	45.6	39.1	5.63
NDTA-T3	39.5	43.0	2.47
NDTA-T4	36.8	45.3	4.79
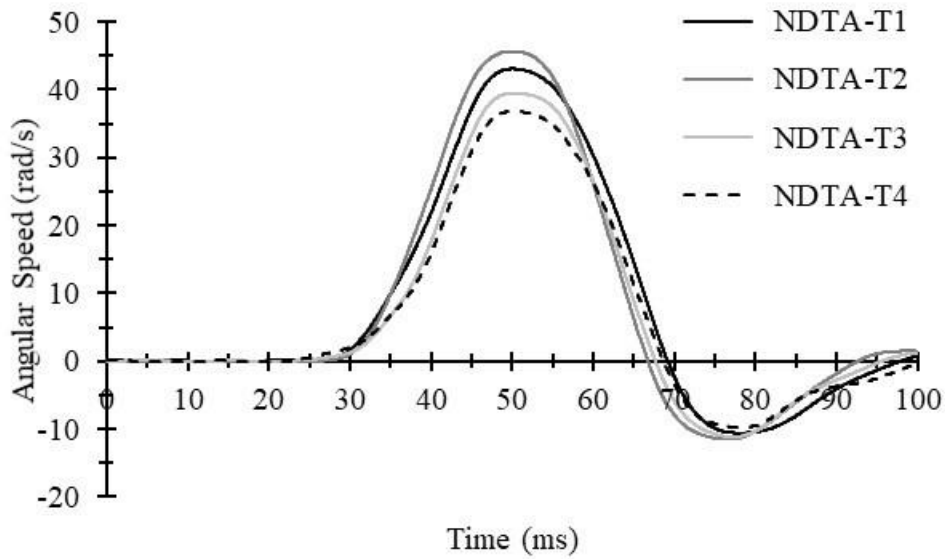
Figure 16. Angular speed profiles for all four tests in NDTA. The peak speeds are aligned at 50 ms.

The angular acceleration of the head throughout each test was calculated (Figure 17). The average peak angular acceleration in all four tests was 3,390 rad/s^2. The maximum and minimum angular accelerations were similar (average of 3305 and -3670 rad/s^2 respectively) for all tests, demonstrating symmetry of the angular speed throughout the acceleration (rising edge) and deceleration (falling edge) phases of the tests.

Figure 17. Calculated angular acceleration of the head specimen for NDTA.

Intracranial Pressure
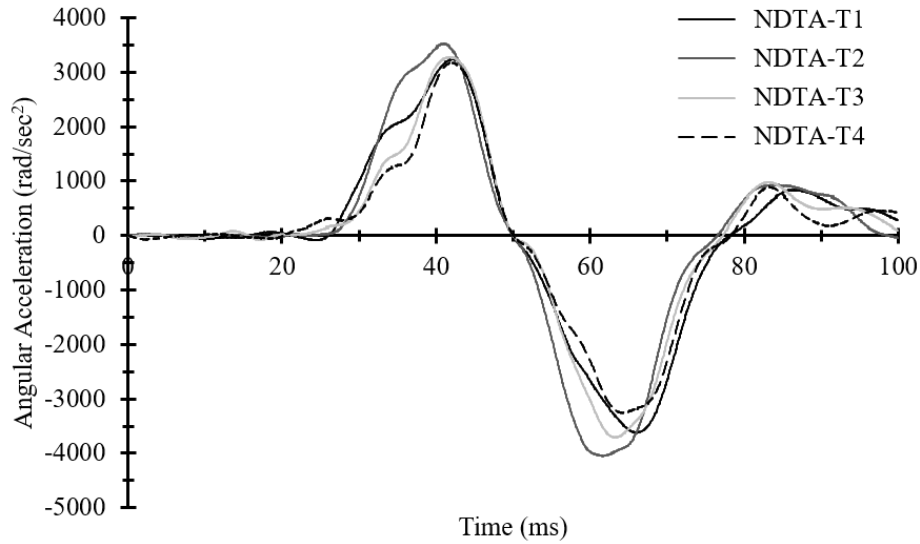
ICP magnitude was small throughout the tests, the maximum values of which are cataloged in Table 5. The average peak frontal ICP in NDTA was 28.6 kPa, and the average minimum was -20.8 kPa. The average maximum and minimum occipital ICPs were 11.0 and -15.3 kPa.

Table 5. Maximum and minimum ICP in the frontal and occipital regions during NDTA.

	Frontal ICP (kPa)		Occipital ICP (kPa)	
	Maximum	Minimum	Maximum	Minimum
NDTA-T1	24.4	-27.6	8.3	-15.9
NDTA-T2	32.3	-24.7	11.3	-17.2
NDTA-T3	29.9	-20.9	11.9	-15.9
NDTA-T4	27.9	-19.8	12.3	-12.0

As seen in Figure 18, the frontal region first experienced a negative pressure, and at the time of the peak angular speed, ICP passed through zero and began a positive phase of larger

magnitude. The occipital region experienced the opposite trend with an initial positive phase, however the initial phase lasted about 10 ms longer in the occipital region. These trends are what would be expected during a chin-to-chest rotation with no impact. In the occipital region, the negative pressure phase had a larger magnitude than the positive phase; however both magnitudes were smaller than those of the frontal region.
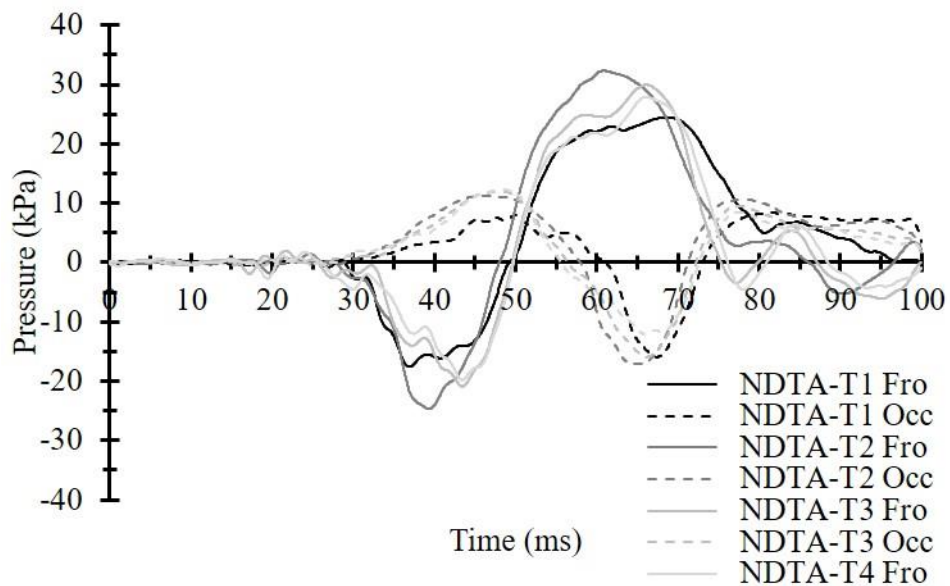

Figure 18. Intracranial pressure time histories from all four tests in NDTA.

Relative Brain-Skull Kinematics

Brain-skull relative motion was measured using high-speed biplane x-ray. Tin granules were implanted into the brain using two schemes (prescribed locations for target deployment) to measure local deformation of the brain tissue with respect to the body-fixed basis of the rigid skull. The coordinate system followed SAE J-211 standards with the X-Y plane corresponding to the Frankfort plane and the z-axis extending from superior to inferior in the median plane. Relative motion data are presented from tests 2-4 for NDTA.

The X-Z displacements are plotted in the head coordinate system. In each plot, X-displacement is on the horizontal axis, and Z-displacement is on the vertical axis — both in millimeters. The head outline represents the orientation of the head during the forward rotation in the sagittal plane. The traces are the time histories of each target throughout a given test. Approximately 120 ms of displacement data were analyzed. X-Z displacement curves for the radial and grid targets from T2 are in Figure 19 and Figure 20. Time histories of x and z-displacement in NDTA-T2 were separated by hemisphere. The radial targets (in the left hemisphere) are in Figure 21, and the grid targets in the right hemisphere are in Figure 22. All motion data were shifted so that the peak angular speeds are aligned at 50 ms.

The traces in Figure 19 show that all 6 radial targets tend to follow a tangential path along a semi-circular pathway, following the contour of the skull. All 6 radial targets are relatively superficial in the brain, so it is expected that they have similar displacements. It may be expected that superficial targets in the opposite hemisphere (Figure 20) would follow similar trends, which appears to be the case. As seen in Figure 21, the radial targets follow the same trend in the X-direction. Initial motion of the targets is negative relative to the skull as the head begins to move, but the bulk of the brain has not yet started to move. This causes the brain to twist, producing an apparent negative relative displacement. After the time of peak angular speed, the head begins to slow down, but the bulk of the brain does not, so relative displacement begins a positive phase until the brain slow and eventually returns to its initial conformation. After the head stops, the brain oscillates, which is seen in all the time histories. The superficial targets (PGB3, PGB4, MGB3, and MGB4) in the grid scheme follow a similar trend; however, the deep targets, PGB1 and PGB2, have the opposite trend, suggesting that they are on the opposite side of the center of rotation for the brain. The Z-displacements exhibit different behavior. All anterior targets—right or left hemisphere, as long as they are anterior to the

EAM—begin with a negative displacement phase. All targets posterior to the EAM begin by moving caudally relative to the skull's motion. The targets on the reference coronal plane, MRB1 and MRB2, have much smaller magnitudes of displacement in the Z-direction.
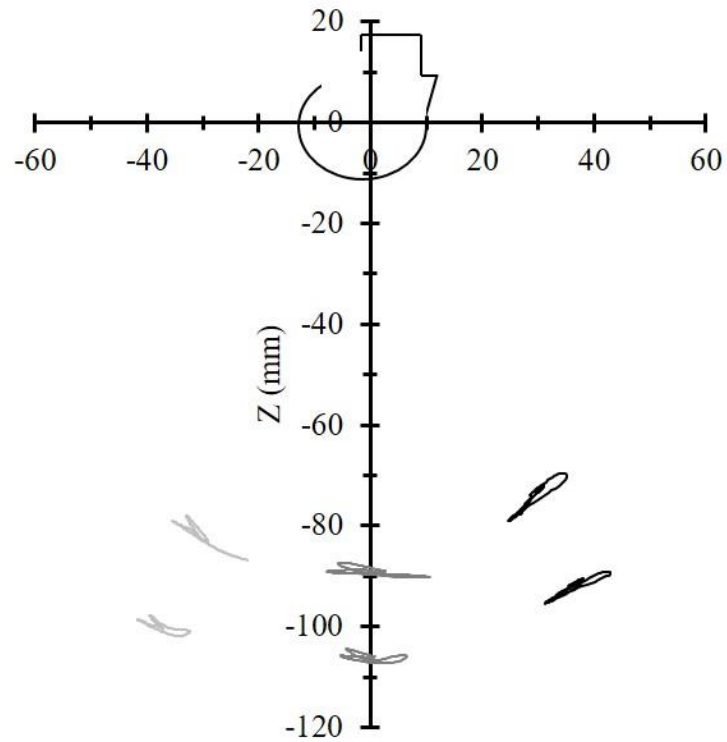

Figure 19. Relative displacement traces of the radial targets from NDTA-T2 in the X-Z plane.
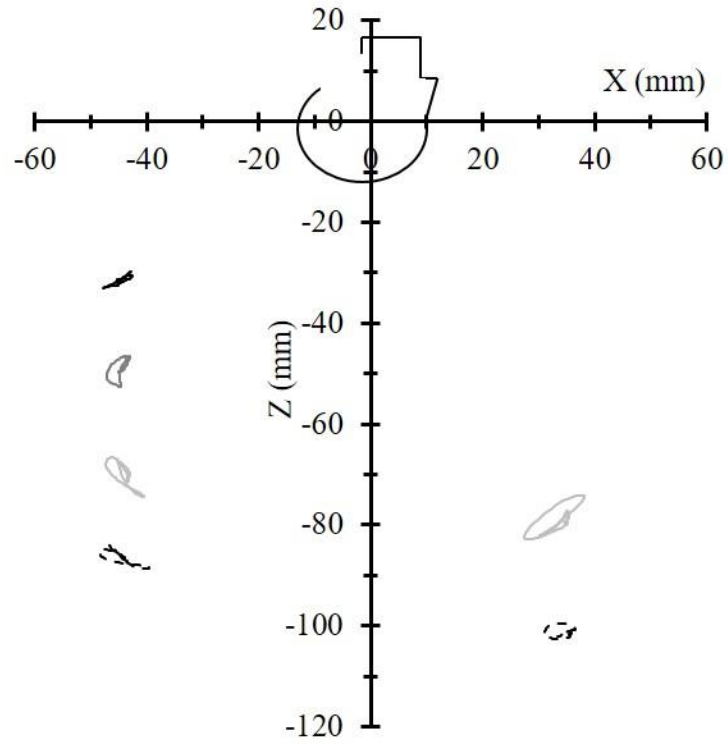
Figure 20. Relative displacement traces of the linear grid targets from NDTA-T2 in the X-Z plane.
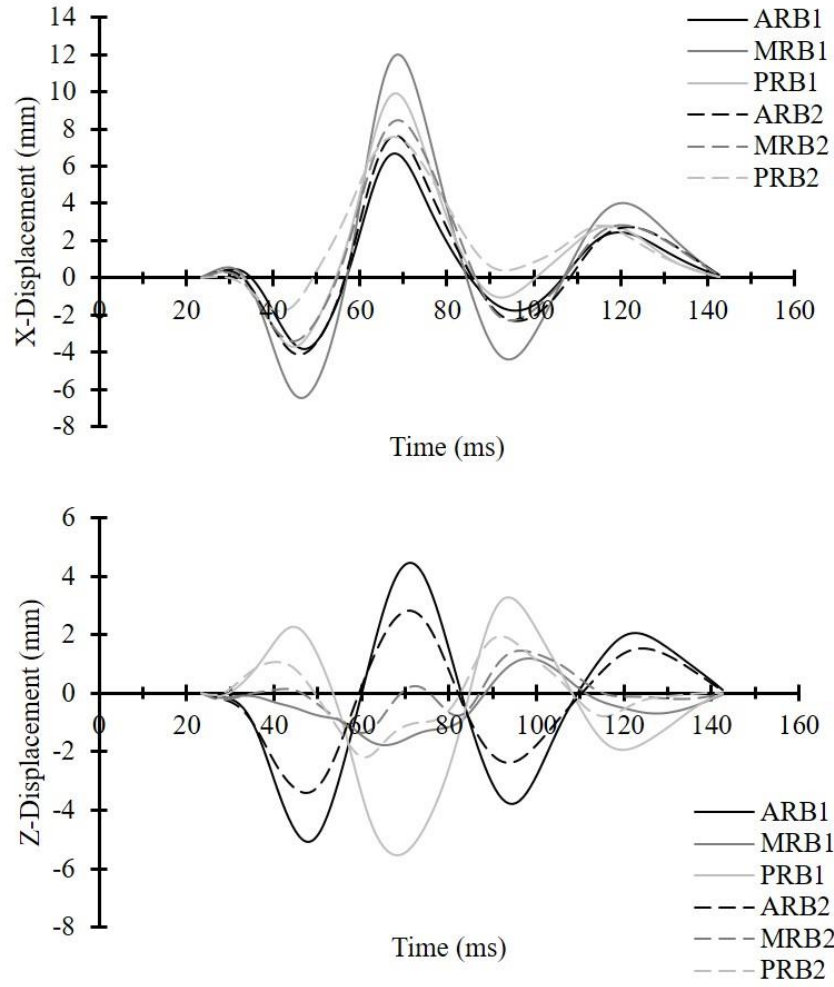
Figure 21. Time histories of X (top) and Z (bottom) displacements for radial targets in NDTA-T2.
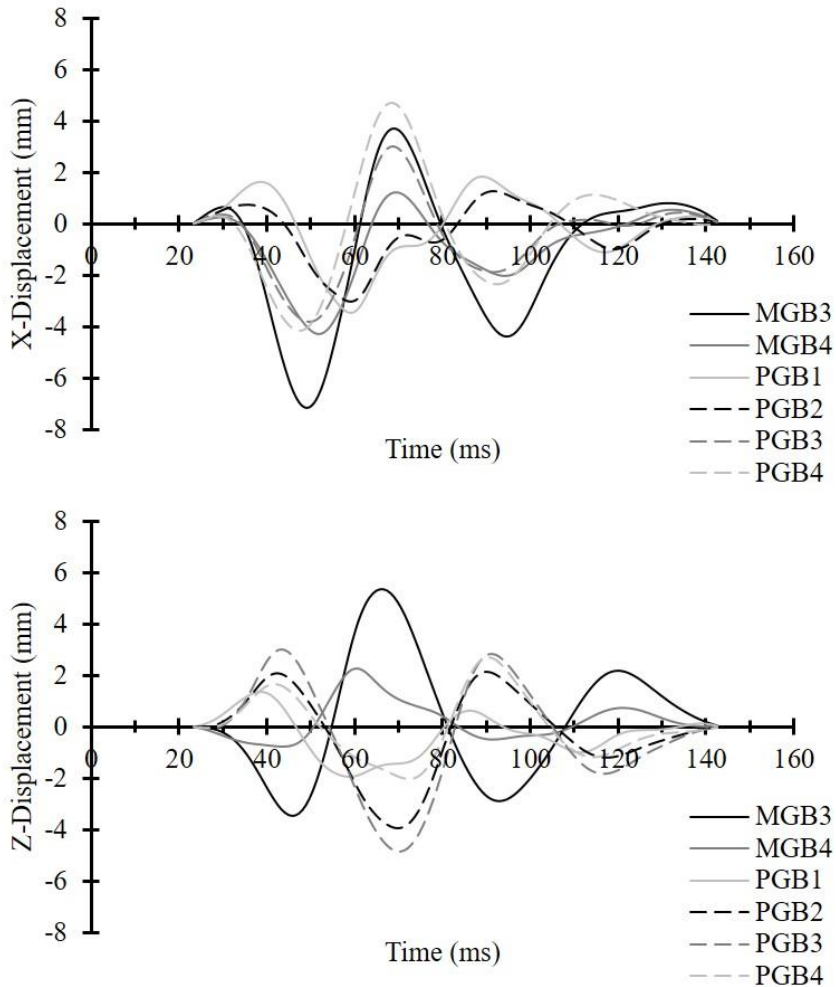
Figure 22. Time histories of X (top) and Z (bottom) displacements for grid targets in NDTA-T2.

Displacement plots from NDTA-T3 and NDTA-T4 are presented in the same order as those for NDTA-T2—X-Z displacement for radial targets, then grid targets followed by X and Z time histories for radial and grid targets (Figure 23 through Figure 30.) Both tests seem to follow the same general trends as NDTA-T2. Maximum and minimum displacements of each target for NDTA-T2 through NDTA-T4 are in Table 6 and Table 7.

Time histories of relative displacements from all three tests have also been compared (Figures A1-A24 in Appendix A.) Displacement patterns of each target varied minimally

40

between tests. The NRMSD of displacement measured by each target in each test was calculated with respect to the average displacement of that target between tests, seen in

Table and Table in Appendix A. The average NRMSD for all points in all tests was 8.7%. Targets which had relatively small displacements varied more between tests, and the displacement of targets from NDTA-T2 showed the largest difference from the other tests with the highest average NRMSD values for X and Z-displacements.
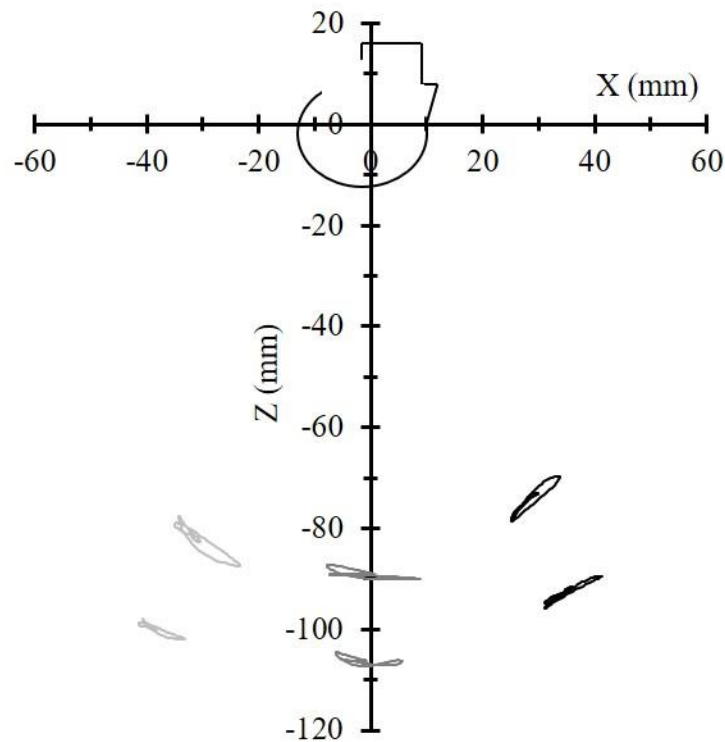

Figure 23. Relative displacement traces of the radial targets from NDTA-T3 in the X-Z plane.

Figure 24. Relative displacement traces of the linear grid targets from NDTA-T3 in the X-Z plane.

Figure 25. Time histories of X (top) and Z (bottom) displacements for radial targets in NDTA-T3.

Figure 26. Time histories of X (top) and Z (bottom) displacements for grid targets in NDTA-T3.

Figure 27. Relative displacement traces of the radial targets from NDTA-T4 in the X-Z plane.
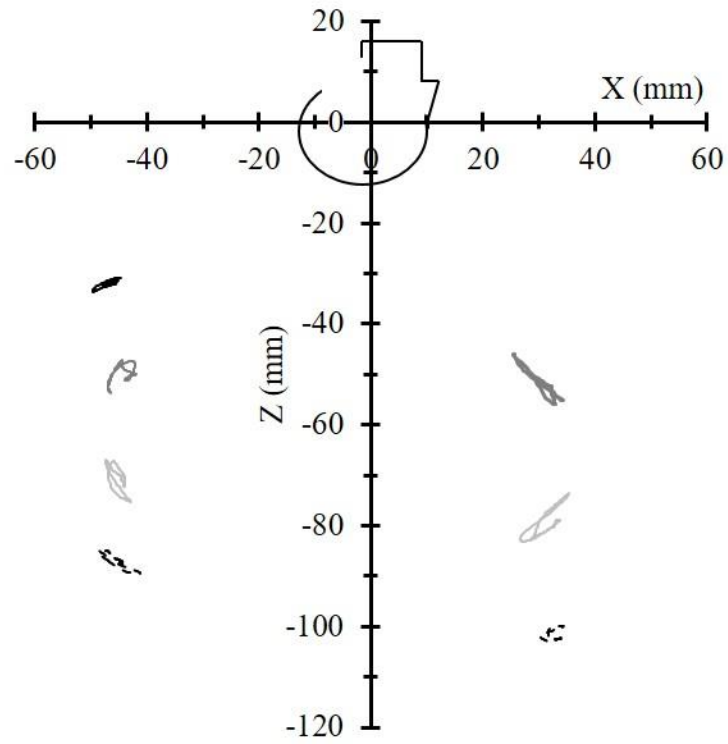
Figure 28. Relative displacement traces of the linear grid targets from NDTA-T4 in the X-Z plane.
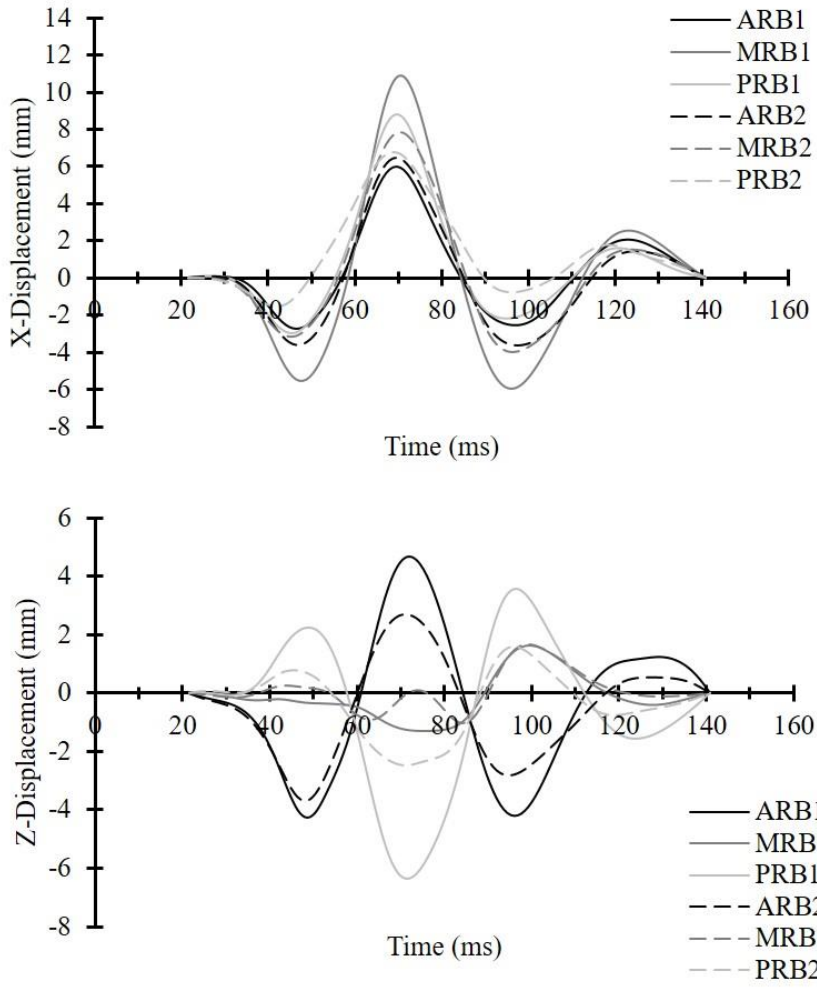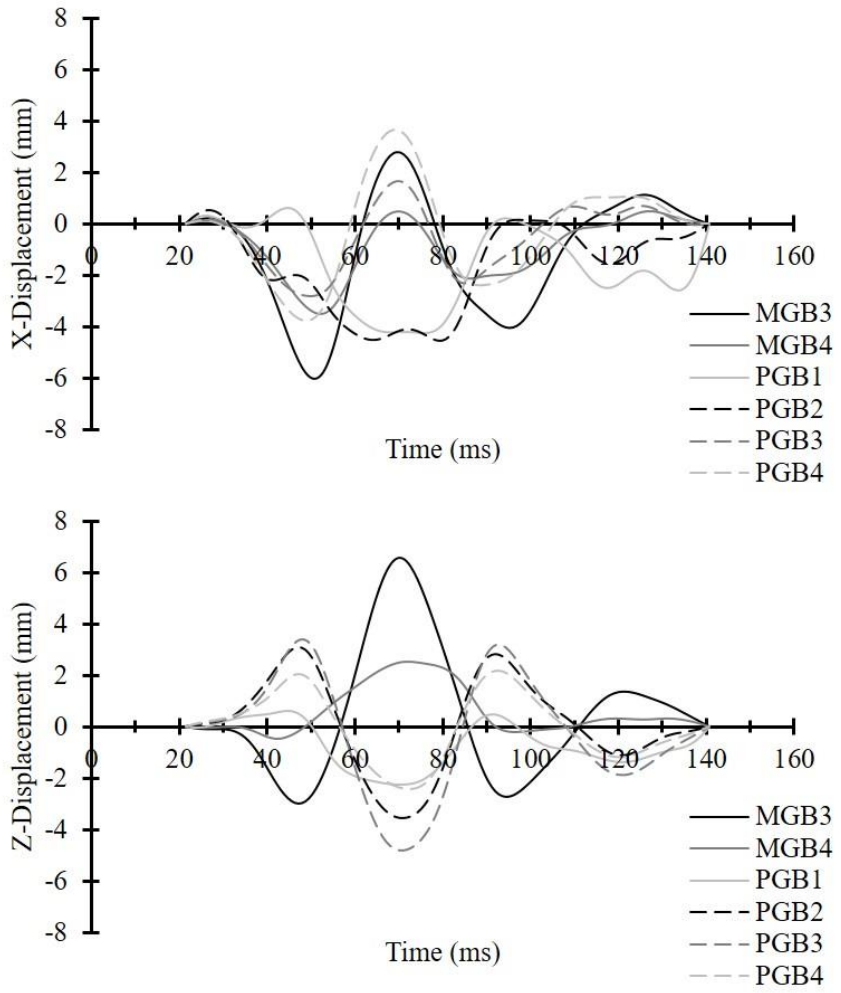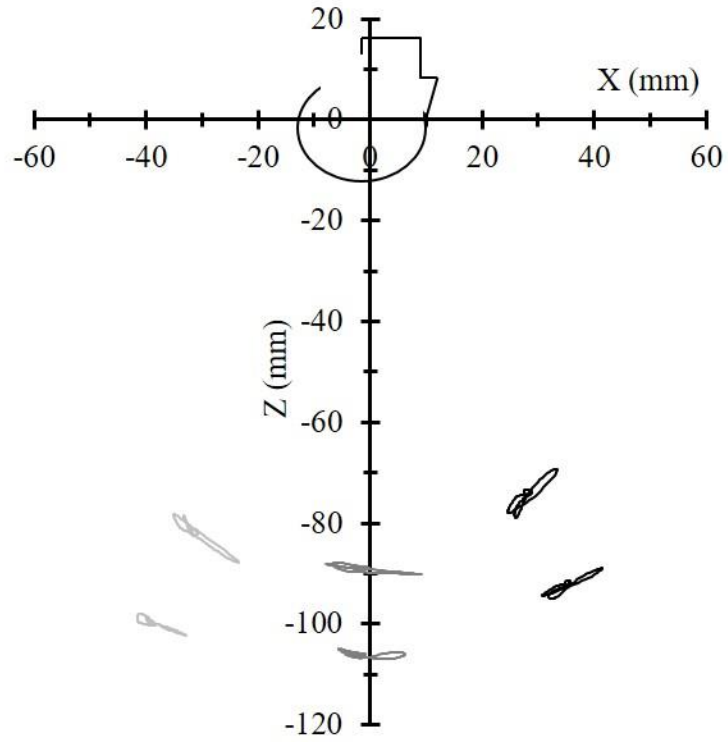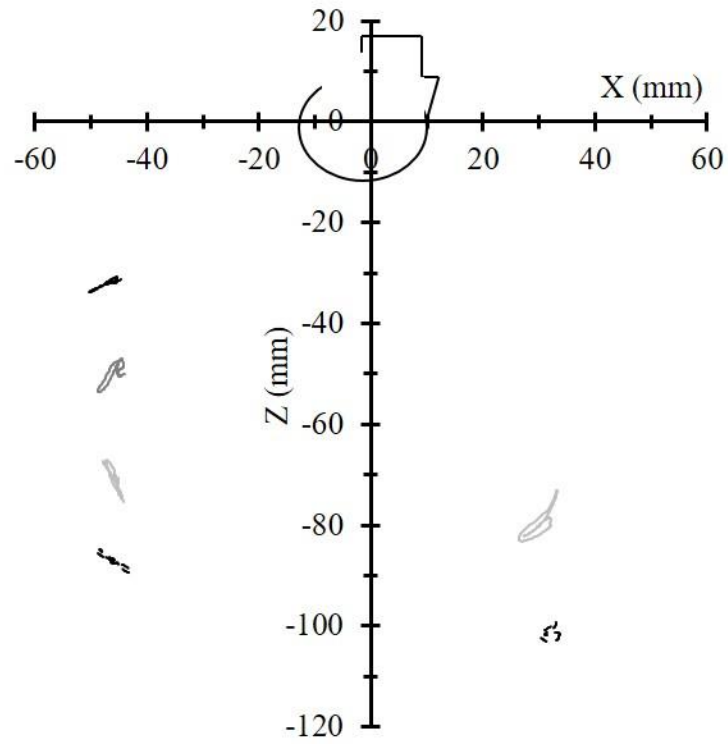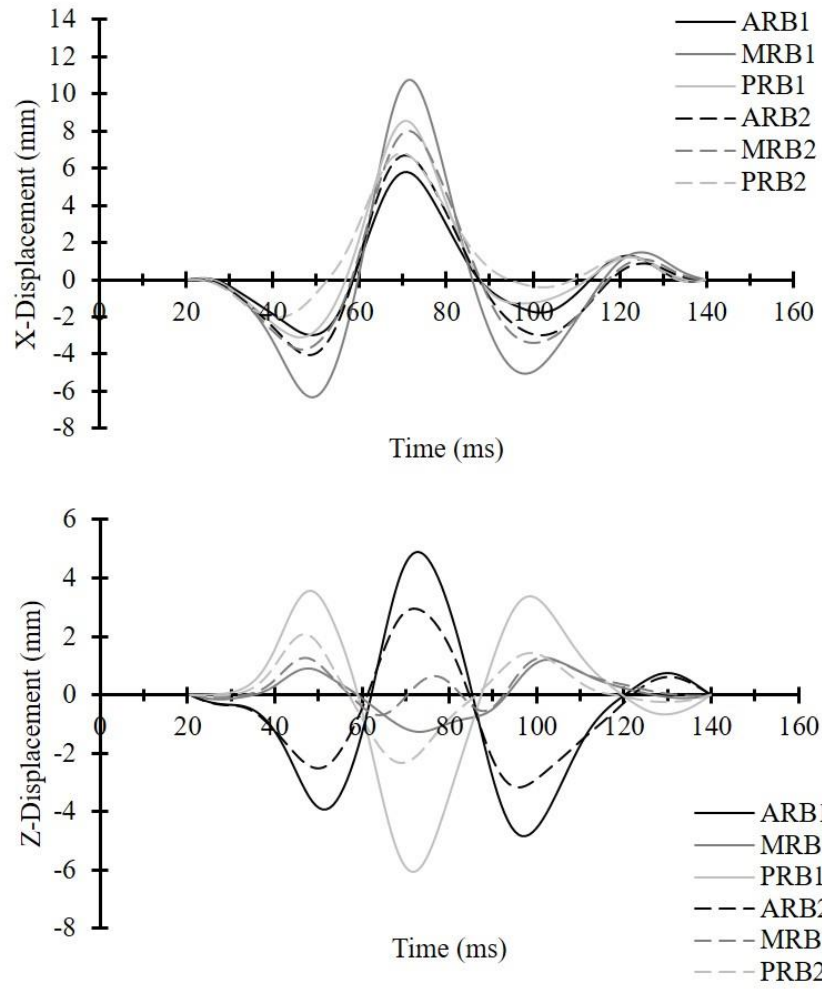
Figure 29. Time histories of X (top) and Z (bottom) displacements for radial targets in NDTA-T4.
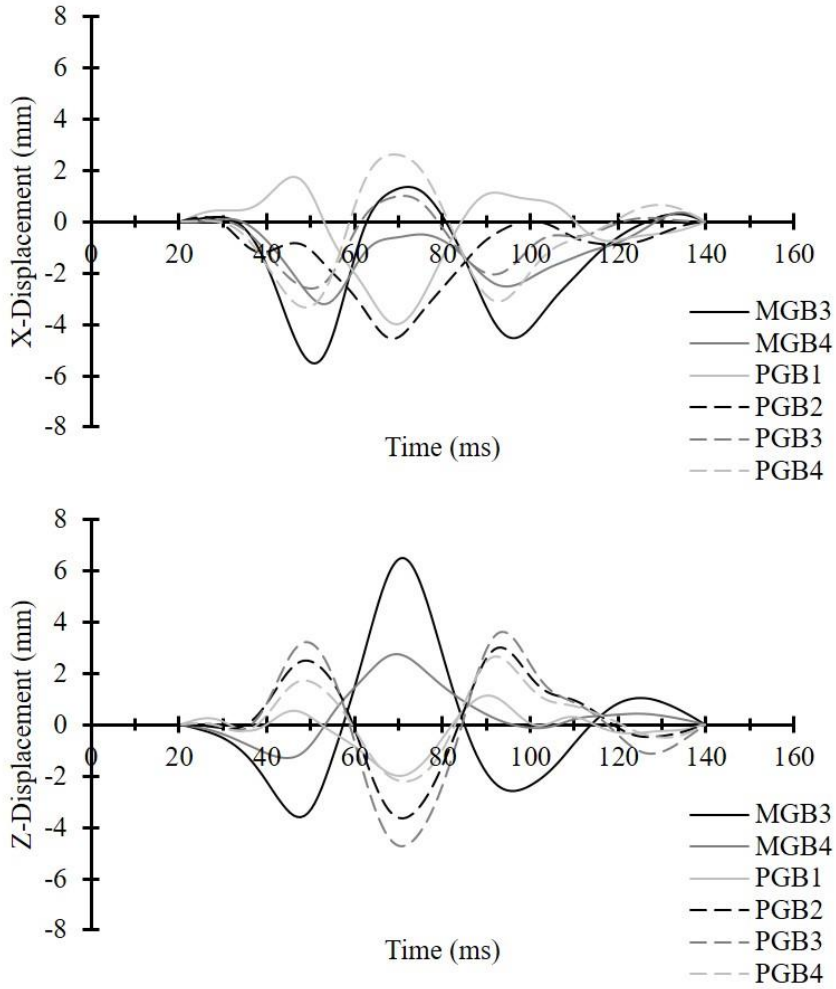
Figure 30. Time histories of X (top) and Z (bottom) displacements for grid targets in NDTA-T4.

Table 6. Peak relative displacements for the radial-pattern targets in NDTA.

(mm)		ARB1		ARB2		MRB1		MRB2		PRB1		PRB2	
T2	X	6.69	-3.86	7.62	-4.15	12.0	-6.48	8.45	-3.44	9.91	-3.71	7.56	-1.79
	Z	4.44	-5.09	2.82	-3.41	1.19	-1.78	1.46	-1.37	3.28	-5.56	1.95	-2.18
T3	X	5.99	-2.76	6.46	-3.65	10.9	-5.94	7.86	-3.96	8.80	-2.98	6.79	-1.54
	Z	4.66	-4.26	2.71	-3.69	1.64	-1.28	1.67	-1.04	3.55	-6.36	1.60	-2.50
T4	X	5.82	-3.00	6.66	-4.06	10.7	-6.33	8.01	-3.76	8.57	-3.10	6.83	-2.01
	Z	4.88	-4.83	2.93	-3.17	1.20	-1.28	1.29	-0.70	3.57	-6.08	2.08	-2.33

Table 7. Peak relative displacements for the grid-pattern targets in NDTA.

(mm)		MGB3		MGB4		PGB1		PGB2		PGB3		PGB4	
T2	X	3.69	-7.18	1.22	-4.29	1.82	-3.45	1.26	-3.03	3.01	-3.83	4.70	-4.18
	Z	5.33	-3.46	2.28	-0.79	1.36	-1.94	2.11	-3.94	3.03	-4.87	2.72	-2.03
T3	X	2.80	-6.03	0.49	-3.53	0.64	-4.23	0.51	-4.57	1.66	-2.81	3.65	-3.79
	Z	6.57	-2.99	2.54	-0.47	0.63	-2.25	3.07	-3.57	3.42	-4.83	2.18	-2.44
T4	X	1.35	-5.51	0.36	-3.22	1.76	-3.99	0.16	-4.58	0.99	-2.62	2.60	-3.33
	Z	6.47	-3.59	2.75	-1.31	1.12	-2.01	3.00	-3.64	3.60	-4.71	2.66	-2.21

NDTB

Four tests with maximum angular speed of 20 rad/s and duration of 60 ms and one test with maximum angular speed of 40 rad/s and 30 ms duration were run on a second PMHS head-neck specimen. As with NDTA, localized motion at several points in the brain with respect to the skull was quantified using high-speed biplane x-ray imaging.

Angular Speed Input

The peak angular speeds of each test pulse, as well as their durations, are cataloged in Table 8. The low speed tests had an average peak of 22.0 rad/s (+/- 0.45), and average duration of 61.3 ms. All motion data were shifted so that the peak angular speeds are aligned at 50 ms (see Figure 31.)

Table 8. Angular speed and duration from each test pulse in NDTB.

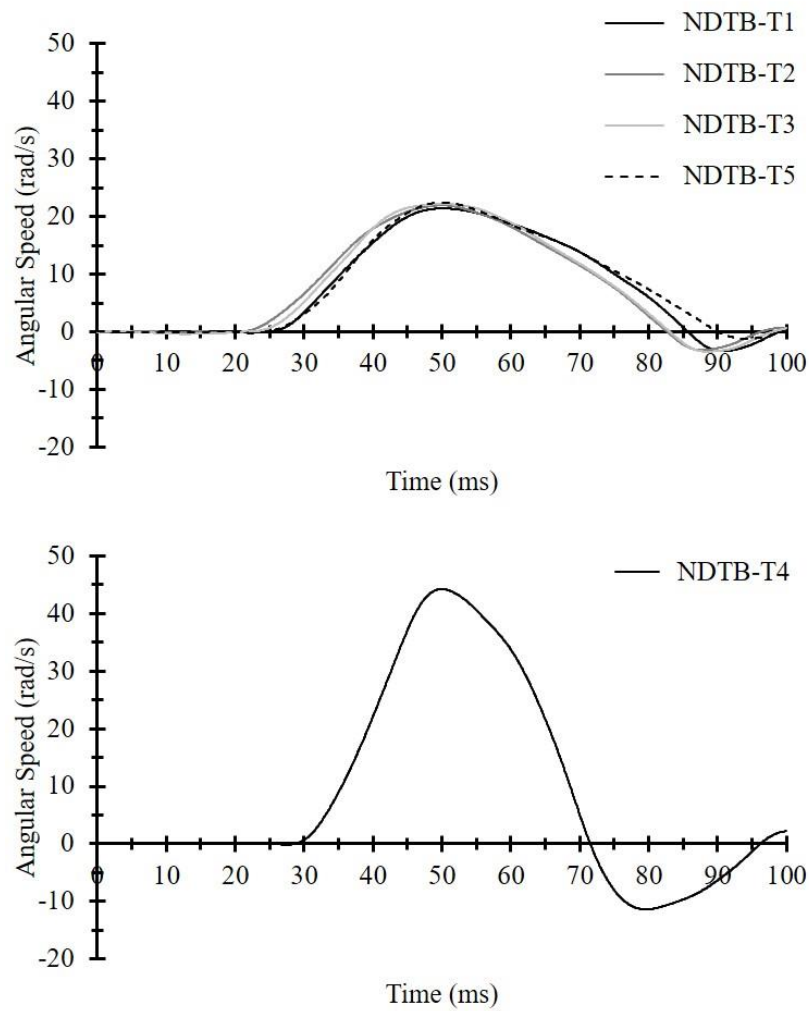| Test ID	Peak Angular Speed rad/s	Duration ms
NDTB-T1	21.4	59.8
NDTB-T2	22.0	60.8
NDTB-T3	22.2	59.8
NDTB-T4	44.2	42.4
NDTB-T5	22.5	64.7

Figure 31. Angular speed profiles for all five tests in NDTB. The peak speeds are aligned at 50 ms.

The NRMSD was calculated for both test speeds in NDTB. The low speed tests were compared to their average angular speed pulse having an average NRMSD of 4.8%, and NDTB was compared to the average of all 5 high-speed tests (including NDTA).

Table 9. NRMSD values for all low-speed and all high-speed tests.

Low-Speed Tests			
NDTB-T1	NDTB-T2	NDTB-T3	NDTB-T5
3.61 %	5.31 %	3.95 %	6.45 %
High-Speed Tests				
NDTA-T1	NDTA-T2	NDTA-T3	NDTA-T4	NDTB-T4
2.12 %	6.34 %	3.79 %	5.24 %	7.15 %

The average peak angular acceleration of the low-speed tests was 1183 rad/s^2, and the average peak from NDTB-T4 was 3,310 rad/s^2. The angular acceleration was similar between low-speed tests over time (Figure 32), with a longer deceleration phase. However the angular acceleration from NDTB-T4 showed more symmetry, similarly to the tests in NDTA.
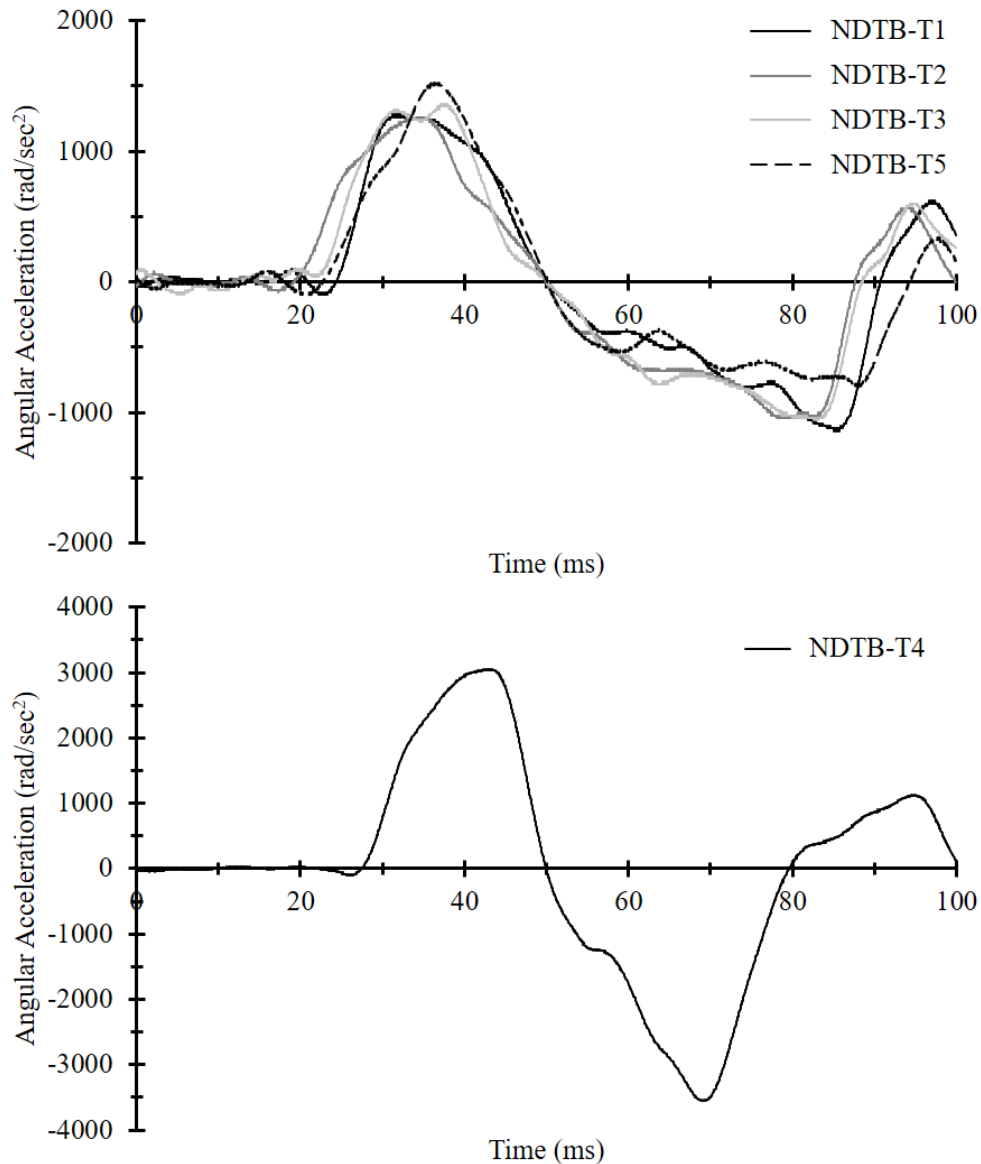
Figure 32. Angular acceleration of the head in NDTB.

Intracranial Pressure

Again, ICP was relatively small in all five tests. The low-speed tests (T1, T2, T3, and T5) had an average maximum ICP of 8.8 kPa, and an average minimum ICP of -14.0 kPa in the frontal region. The occipital region experienced average maximum and minimum ICPs of 9.2 kPa and -2.7 kPa, respectively. These magnitudes are substantially smaller than those of T4 (the high-speed test), which had a maximum and minimum ICP of 42.5 and -28.0 kPa in the frontal

region, and 26.1 and -12.7 kPa in the occipital region. Time histories of ICP in the low-speed tests are different from NDTB-T4 in magnitude and duration (Figure 33. Intracranial pressure readings from the low-speed (top) and high-speed tests (bottom) in NDTB.

Table 10. Maximum and minimum ICP in the frontal and occipital regions during NDTB.

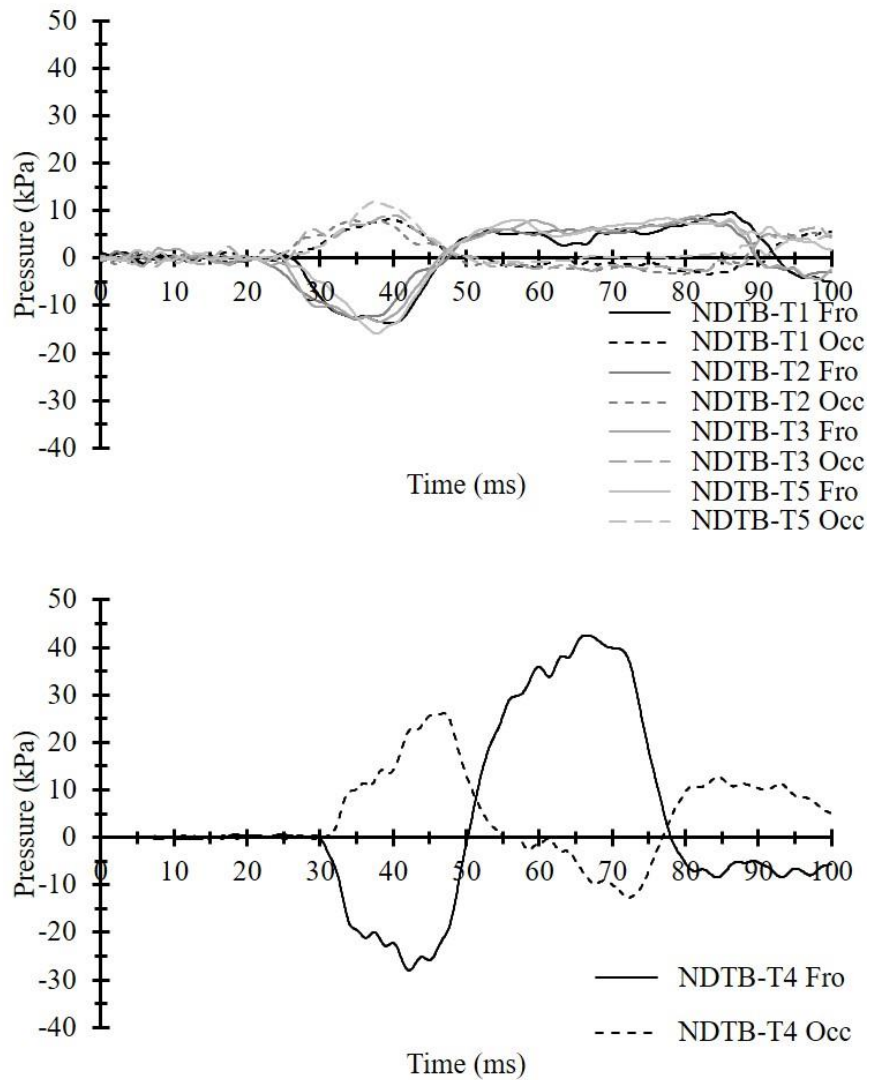|	Frontal ICP (kPa)		Occipital ICP (kPa)	
	Maximum	Minimum	Maximum	Minimum
NDTB-T1	9.7	-13.7	8.2	-3.4
NDTB-T2	8.3	-12.9	7.9	-3.4
NDTB-T3	8.9	-13.4	9.0	-2.8
NDTB-T4	42.5	-28.0	26.1	-12.7
NDTB-T5	8.4	-15.9	11.8	-1.3

Figure 33. Intracranial pressure readings from the low-speed (top) and high-speed tests (bottom) in NDTB.

Relative Brain-Skull Kinematics

      Targets were implanted in the brain using the same two schemes as in NDTA, but were

scaled to the dimensions of PMHS 2. Again, the deformation of the brain relative to the skull

was quantified in a body-fixed coordinate system following SAE J-211 standards where the X-Y

plane corresponds to the Frankfort plane and the Z-axis extends caudally. Relative motion data

are presented from NDTB-T1 through T5.

The relative displacements in the sagittal plane for all targets in the NDTB series are shown. In all plots, the X-axis is horizontal and the Z-axis is vertical. Each plot has a head outline to demonstrate the coordinate system and target location with respect to the skull. Approximately 120 ms of data were processed for all tests in NDTB. All motion data were shifted so that the peak angular speeds are aligned at 50ms. The traces represent the time history of each target's movement in the sagittal plane (relative to the motion of the skull.) Figure 34 and Figure 35 show the X-Z displacement traces for the radial and grid targets, respectively, in NDTB-T1. In addition, time-history plots of each displacement axis for each hemisphere are in Figure 36 and Figure 37. All displacement data presented are in millimeters, and time is always represented in ms.
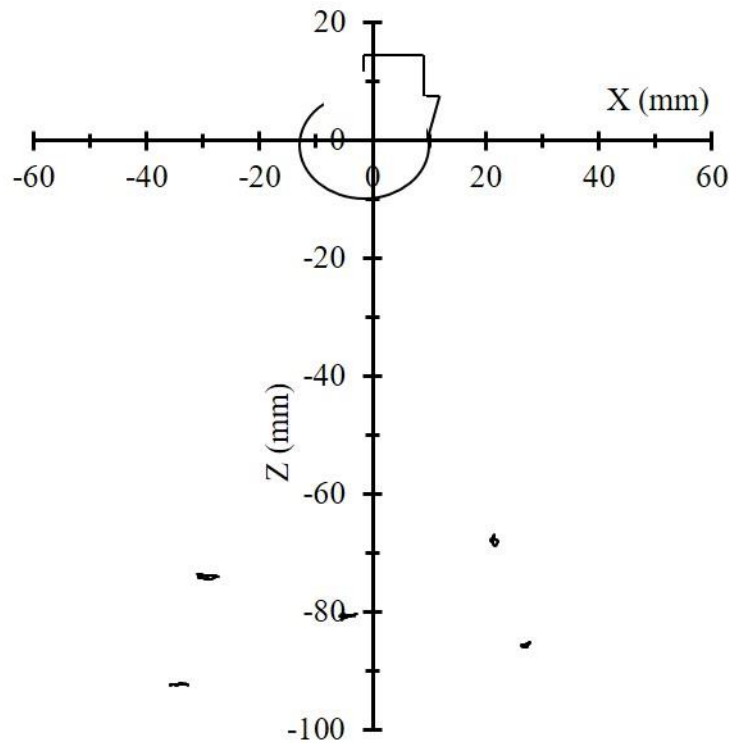

Figure 34. Relative displacement traces of the radial targets from NDTB-T1 in the X-Z plane.
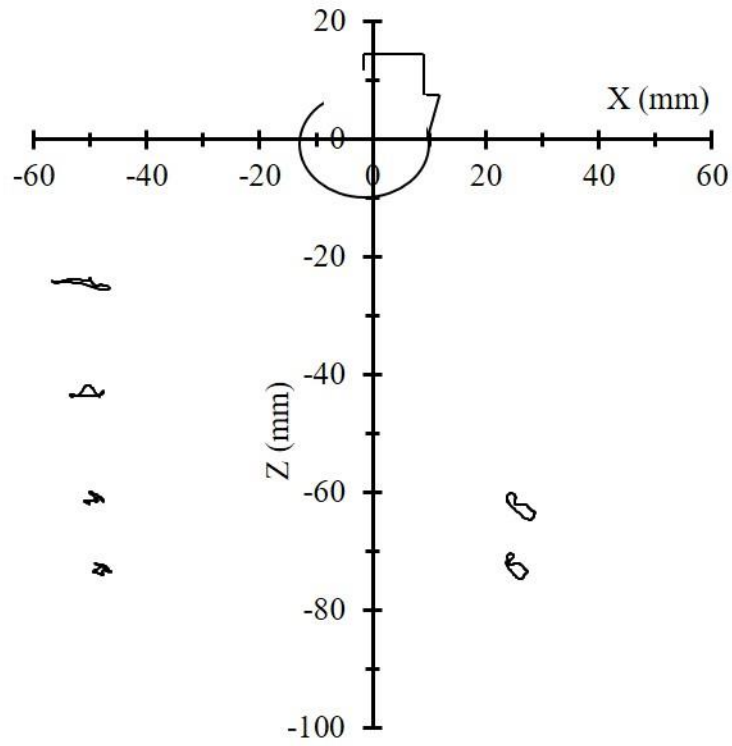
55

Figure 35. Relative displacement traces of the linear grid targets from NDTB-T1 in the X-Z plane.
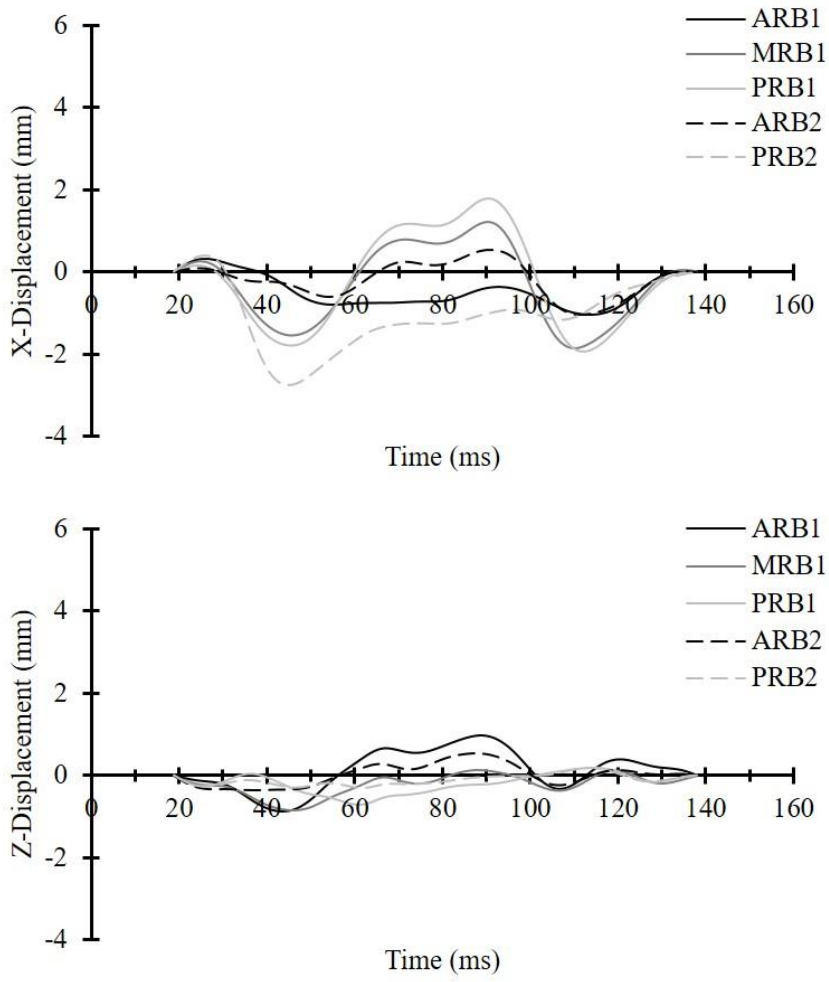
Figure 36. Time histories of X (top) and Z (bottom) displacements for radial targets in NDTB-T1.
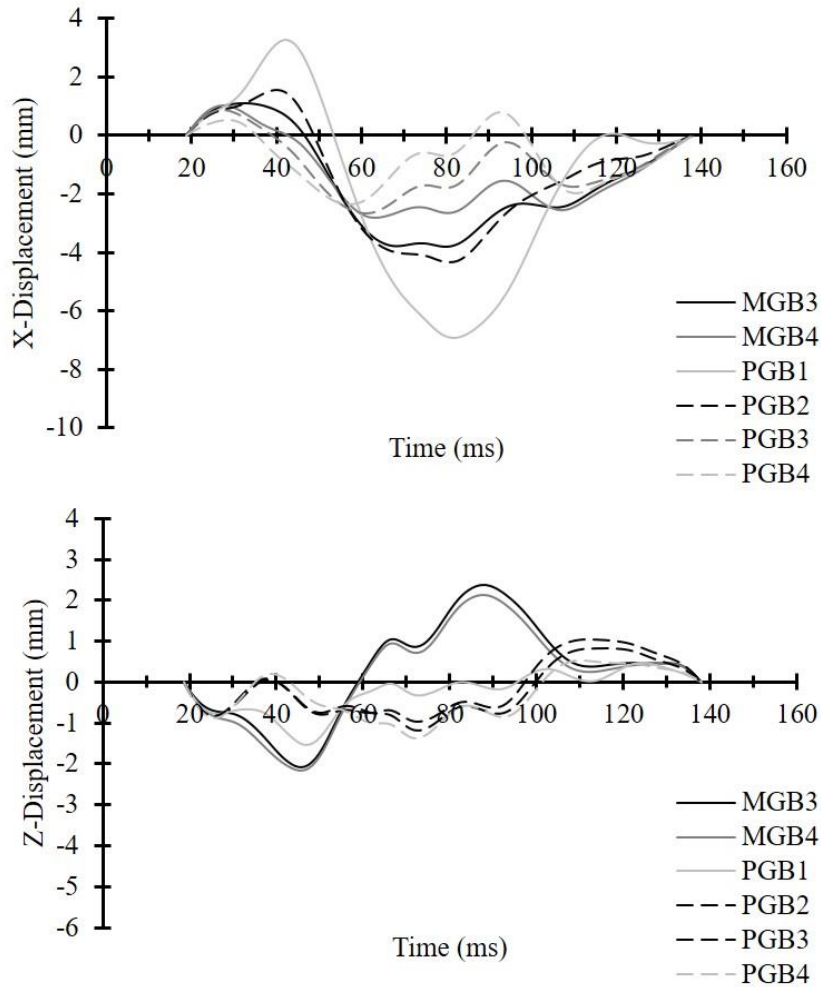
Figure 37. Time histories of X (top) and Z (bottom) displacements for targets in NDTB-T1.

The relative displacement of the brain in NDTB are similar between the low speed tests, with magnitudes that were much smaller than in NDTA. NDTB-T4 produced displacements of similar magnitude, however the trends in orientation of displacement traces are not seen. X-Z displacement plots and time histories of motion in the x and z-directions are in Figure 38 through Figure 53. The consistency of pattern between tests varies much more in NDTB, likely because of the smaller displacements.
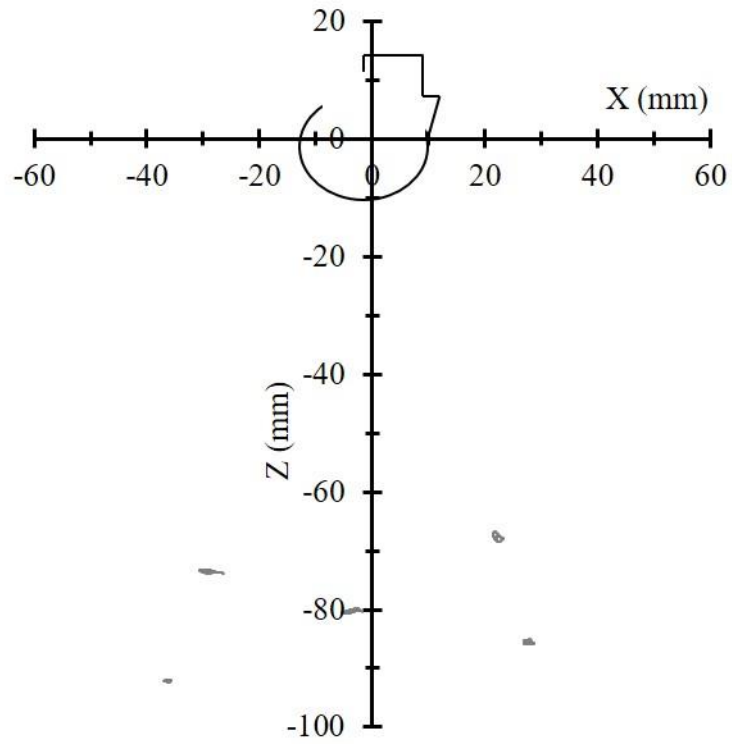
Figure 38. Relative displacement traces of the radial targets from NDTB-T2 in the X-Z plane.
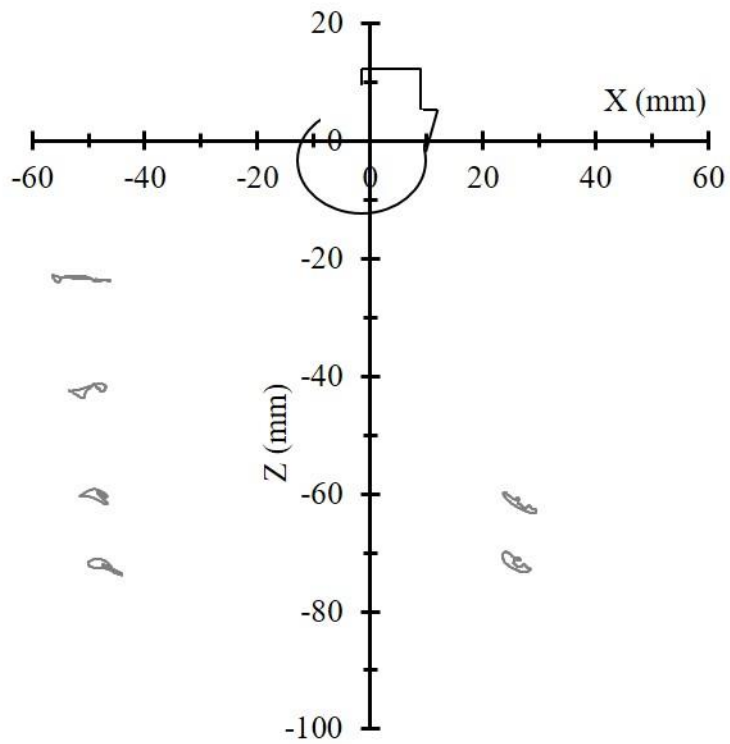
Figure 39. Relative displacement traces of the linear grid targets from NDTB-T2 in the X-Z plane.

Figure 40. Time histories of X (top) and Z (bottom) displacements for radial targets in NDTB-T2.

Figure 41. Time histories of X (top) and Z (bottom) displacements for grid targets in NDTB-T2.

Figure 42. Relative displacement traces of the radial targets from NDTB-T3 in the X-Z plane.

Figure 43. Relative displacement traces of the linear grid targets from NDTB-T3 in the X-Z plane.
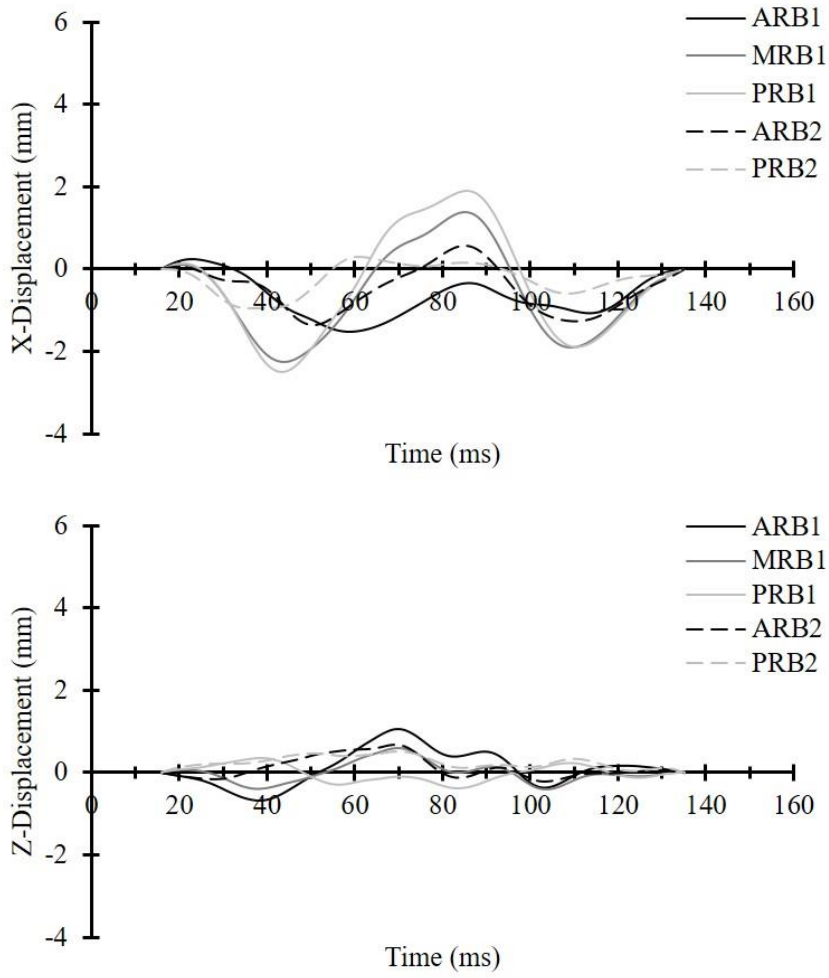
63

Figure 44. Time histories of X (top) and Z (bottom) displacements for radial targets in NDTB-T3.
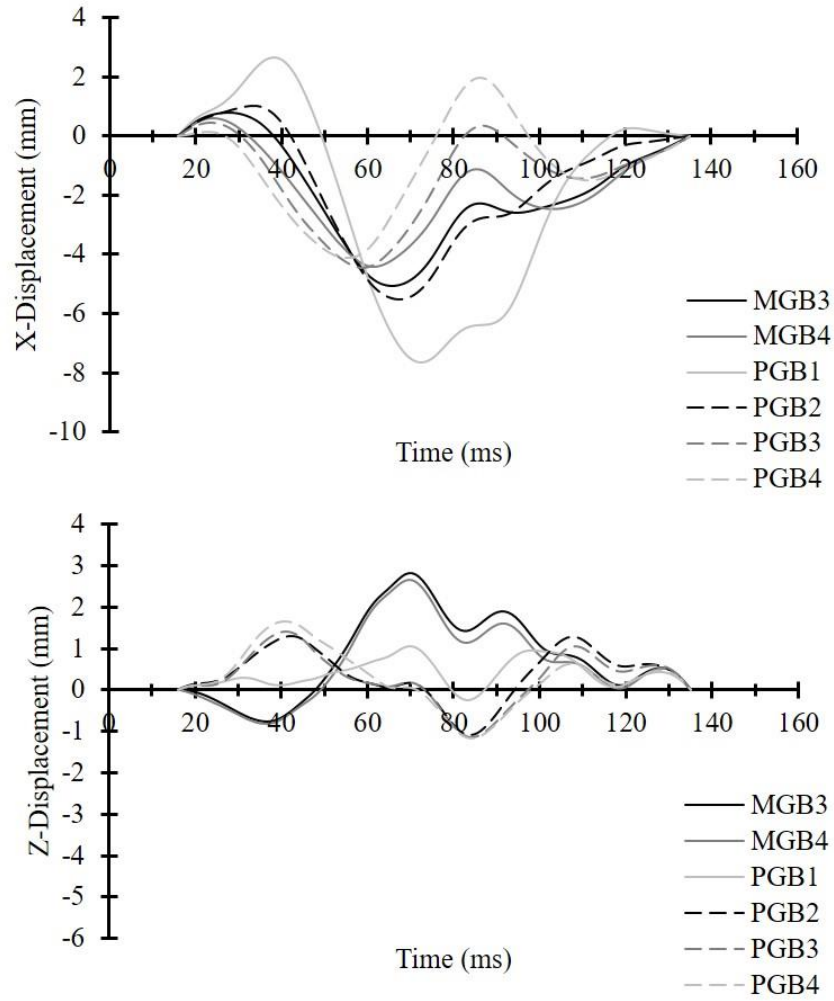
Figure 45. Time histories of X (top) and Z (bottom) displacements for grid targets in NDTB-T3.
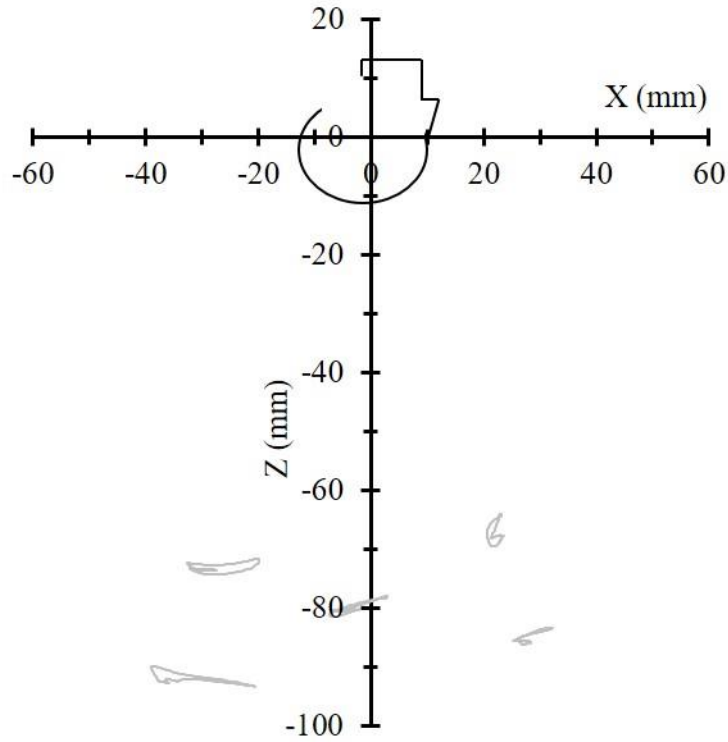
Figure 46. Relative displacement traces of the radial targets from NDTB-T4 in the X-Z plane.
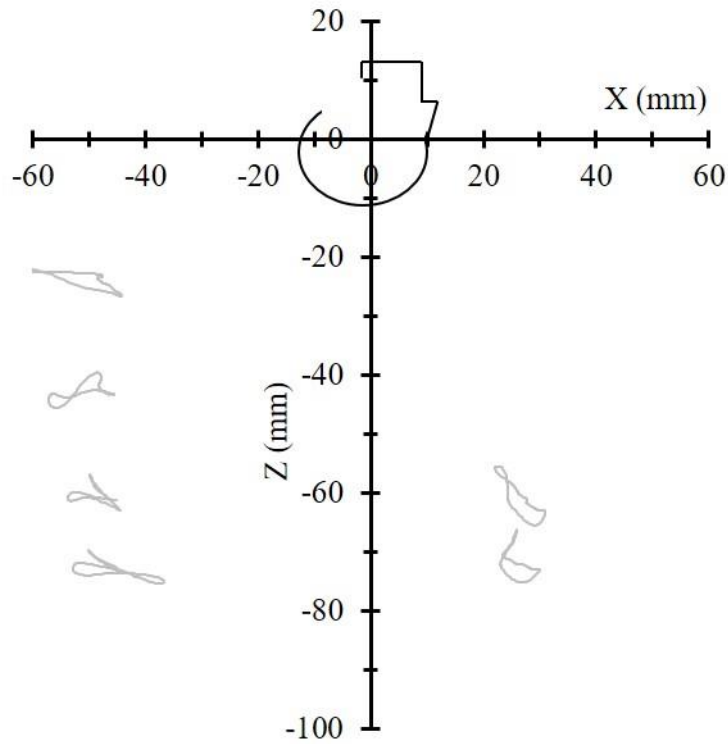
Figure 47. Relative displacement traces of the linear grid targets from NDTB-T4 in the X-Z plane.
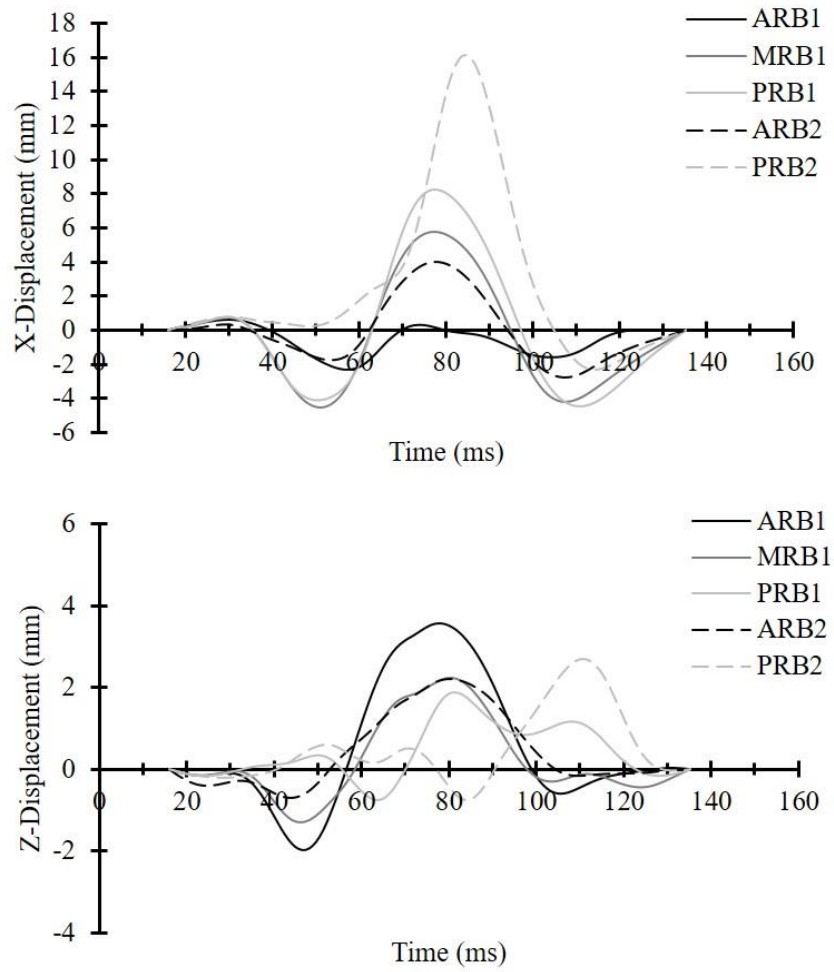
Figure 48. Time histories of X (top) and Z (bottom) displacements for radial targets in NDTB-T4.
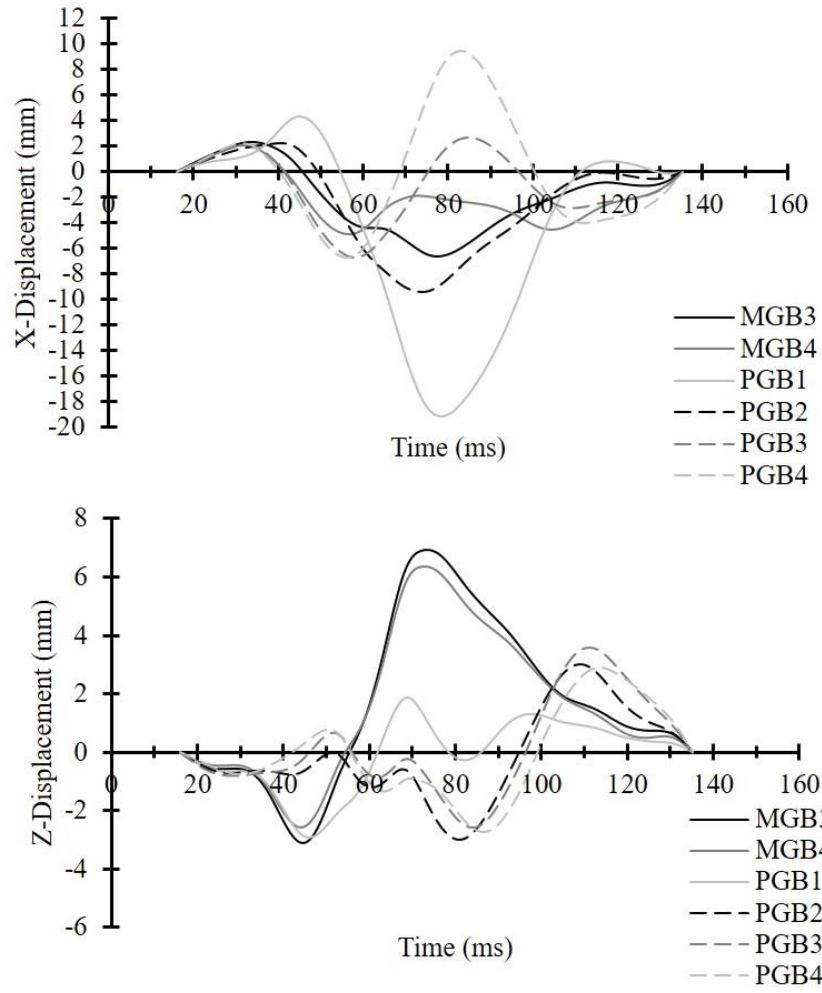
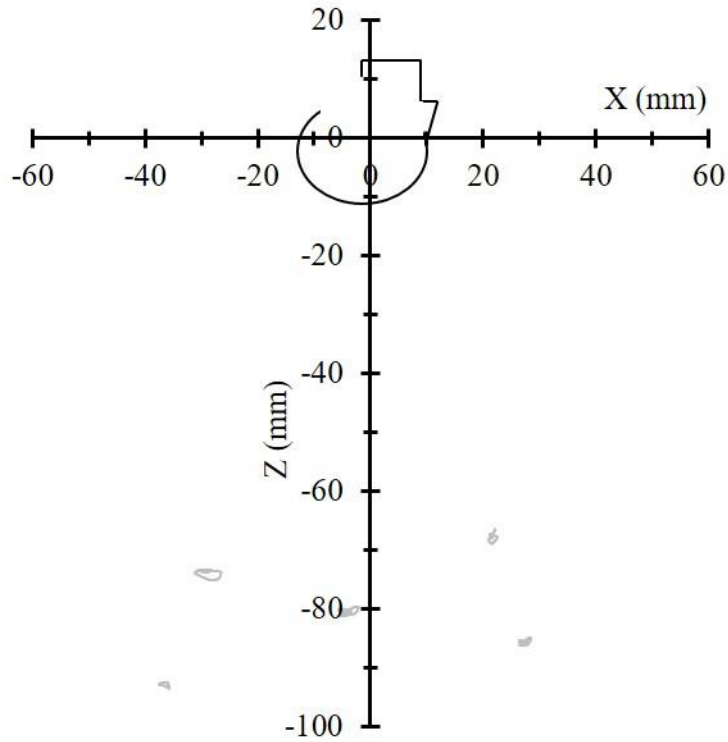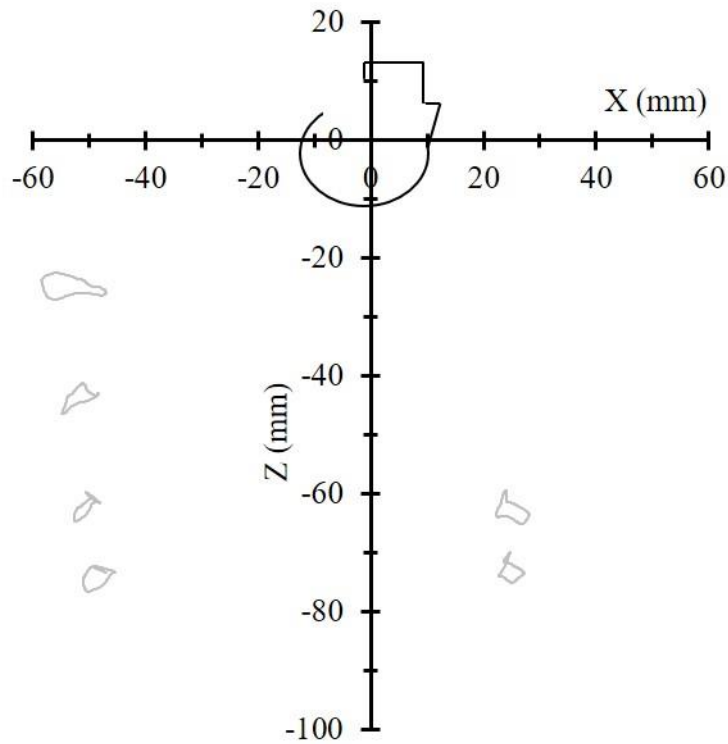**Figure 49. Time histories of X (top) and Z (bottom) displacements for grid targets in NDTB-T4.**
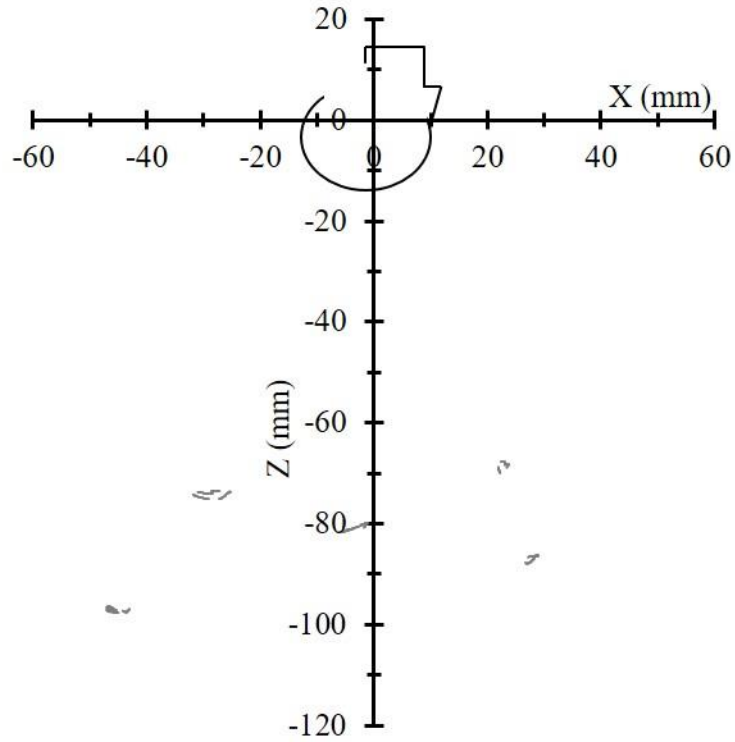
Figure 50. Relative displacement traces of the radial targets from NDTB-T5 in the X-Z plane.
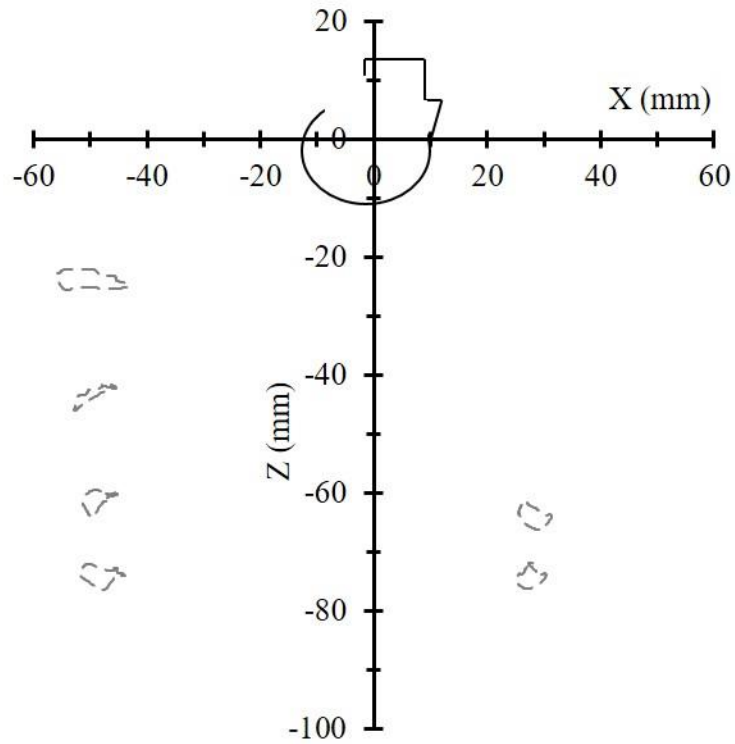
Figure 51. Relative displacement traces of the linear grid targets from NDTB-T5 in the X-Z plane.
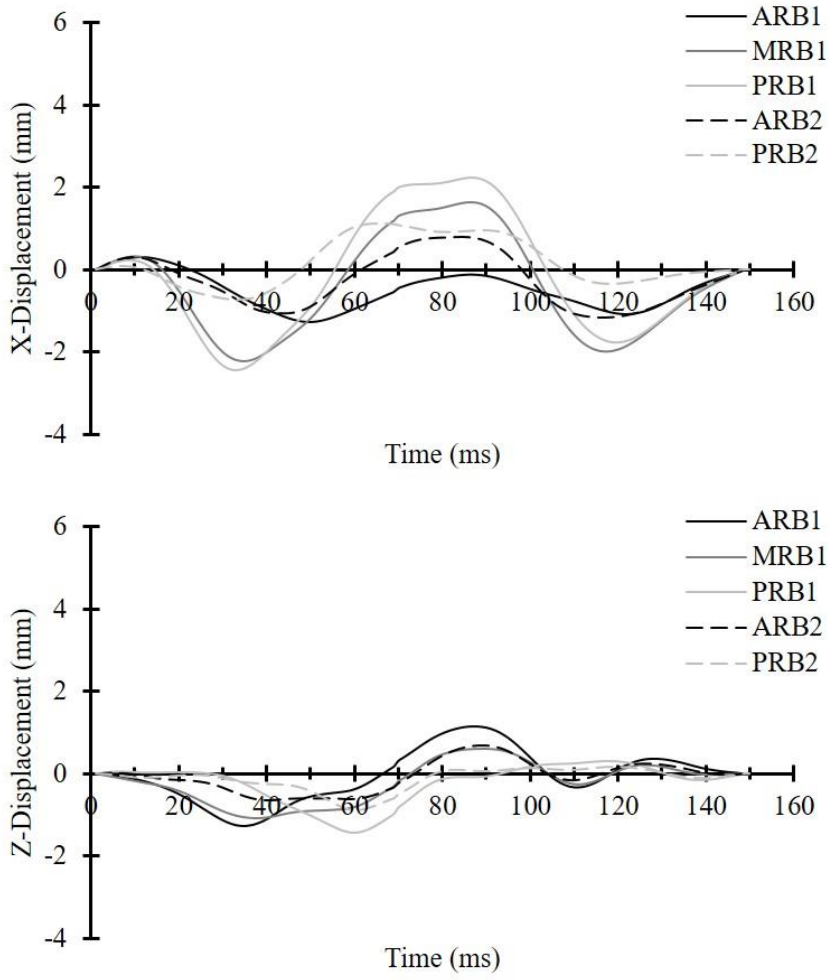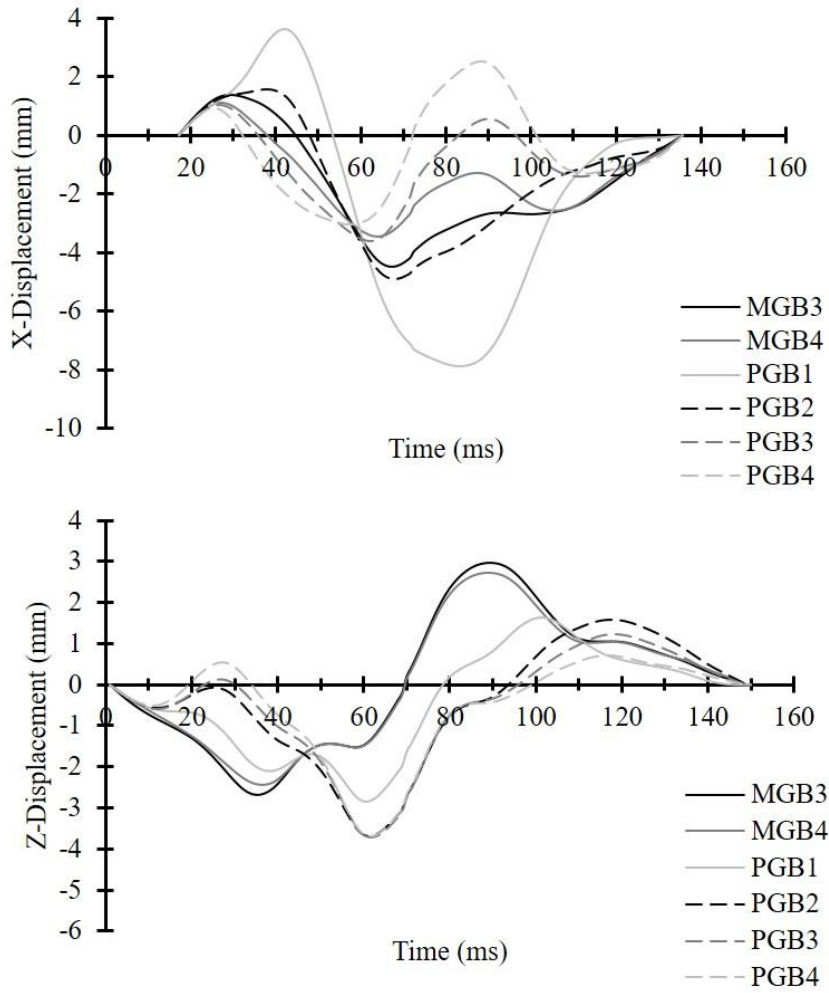
69
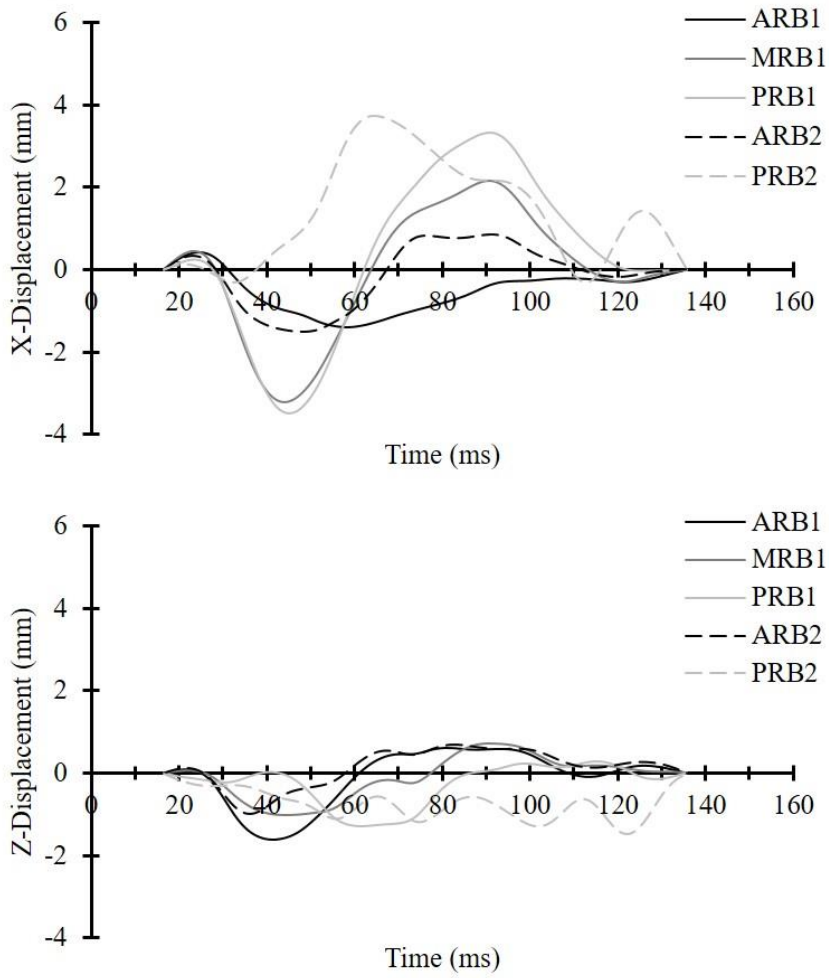
Figure 52. Time histories of X (top) and Z (bottom) displacements for radial targets in NDTB-T5.
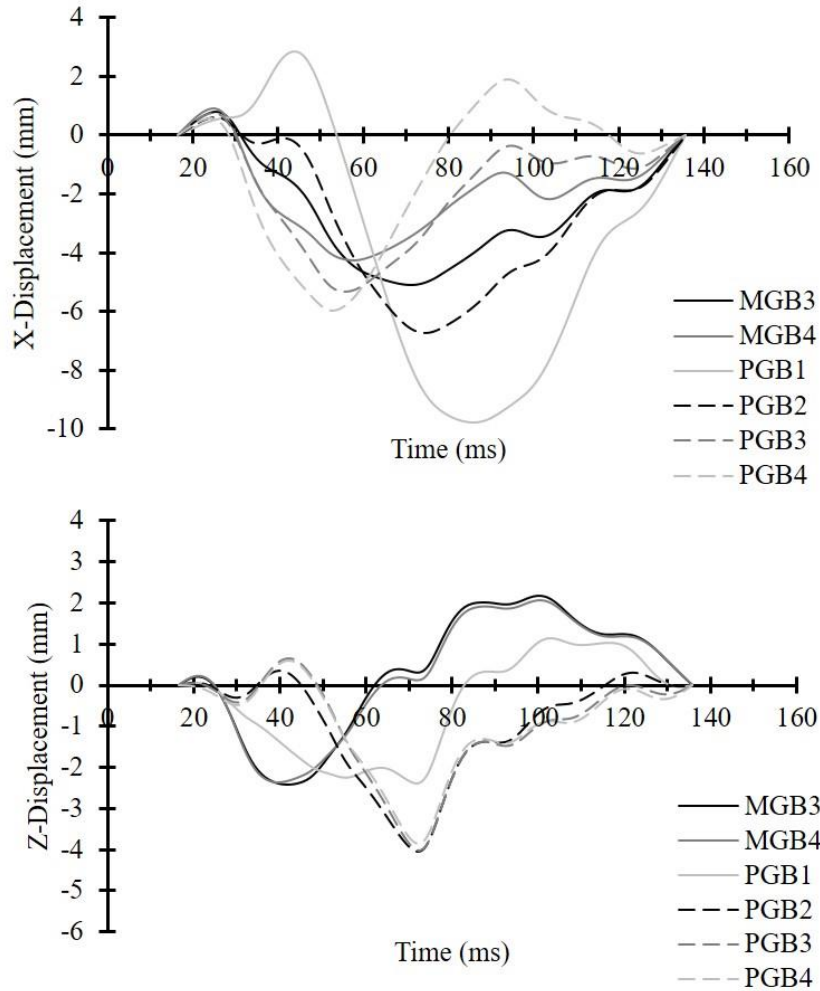
Figure 53. Time histories of X (top) and Z (bottom) displacements for grid targets in NDTB-T5.


Discussion

NDTA

Series A included four tests with an angular speed pulse having maximum speed of 40 rad/s and duration of 30 ms. Frontal and occipital ICP data were obtained for all four tests, however relative brain displacement data were obtained for three tests.

Angular Speed

The average maximum angular speed measured in NDTA was 41.2 rad/s with an average duration of 42.1 ms. Additionally, as seen in Figure 16, there is a short, negative speed duration at the end of the test. This, as well as the slightly higher angular speed, is caused by a slight over-rotation of the head. The over-rotation and any deviations from the sine trace were caused by brief moments were the follower lost contact with the cam because of the momentum of the head. Reaction springs at the front and back ends of the follower were designed to control the follower-cam contact throughout a test, but the coupling achieved was never perfect.

Examining differences between an ideal half-sine and the measured test pulses can help illustrate potential causes of differences between expected and actual angular speed pulse characteristics. In Figure 54, the angular speed pulses from all four tests in NDTA are plotted with a half-sine with an amplitude of 40 rad/s and duration of 30 ms centered at 50 ms. Upon visual inspection, it can be seen that the magnitude of the sine is in the middle of the tests, which deviated by less than 10% from their average of 41.2 rad/s. The slopes of the curves near the peak on the leading edge, and the entire trailing edge seem parallel to the slope of the sine. Larger differences appear near the start and end of the pulses. However, all of the tests start similarly to each other.
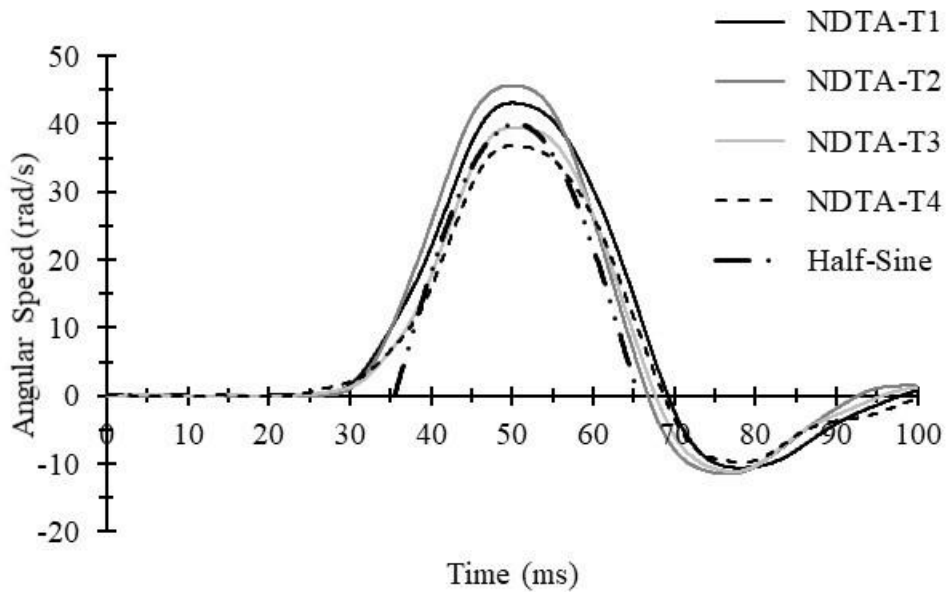
Figure 54. Angular speed pulses from all four tests in NDTA plotted with a half-sine resembling the ideal pulse.

When comparing angular speed pulses to each other, the NRMSD of each test with respect to the average speed pulse was relatively low (average of 4.1%). This signifies that while the test pulses deviated from the ideal half-sine, the four test inputs were consistent with each other. That comparison includes the negative angular speed portion of the test pulses.

Intracranial Pressure

In general, the ICPs in NDTA are much lower in magnitude than what was measured by Hardy et al. [14,15] where angular speeds were never more than 30 rad/s. Those studies were done with head impacts that involved either linear or combined angular and linear accelerations. The large linear acceleration and impact of those tests caused the large ICP of up to 150 kPa. Other studies of ICP in head impact have pressure profiles similar to those found by Hardy et al. [13–15] . Peak coup intracranial ICP is directly correlated with resultant linear acceleration at the c.g. of the head [13,15]. The maximum pressure in NDTA was 32.3 kPa. The significantly lower ICP values in these tests involving pure rotation are related to inertial effects. This result is as

expected since a strong positive correlation between linear acceleration and ICP has been found previously.

Brain Kinematics

Intracranial pressure in the frontal and occipital regions followed specific trends in each test in the NDTA series. At the frontal location, pressure was initially negative, due to the lack of global motion of the brain as the head started to move. Initially the brain is twisting with respect to the skull (Figure 55.) When the brain begins moving globally, it is moving towards its initial conformation with respect to the skull. The restorative motion caused the magnitude of relative motion to decrease up to the time of maximum angular speed. After the head reaches maximum speed, it begins to slow down while the brain continues to deform. This pattern of motion is what causes the ICP to pass through zero near 50 ms and to transition to a positive phase. As the brain returns to its original conformation within the cranial cavity, the pressure decreases again to physiologic conditions. The opposite happens at the occipital location - beginning with positive pressure that transitions to negative pressure near 60 ms. The occipital ICP does not transition through zero until 10 ms later than the frontal ICP. Additionally, the magnitude of the positive ICP at the occipital transducer is much smaller in magnitude than at the frontal transducer. In the previous impact studies, coup ICP had a large rise in positive pressure with a short pulse duration, however there was no negative phase as with the current study [13–15]. This again shows the positive correlation between linear acceleration and coup ICP, as well as the correlation between angular speed and relative brain/skull motion which produces the positive and negative ICP in the current study.
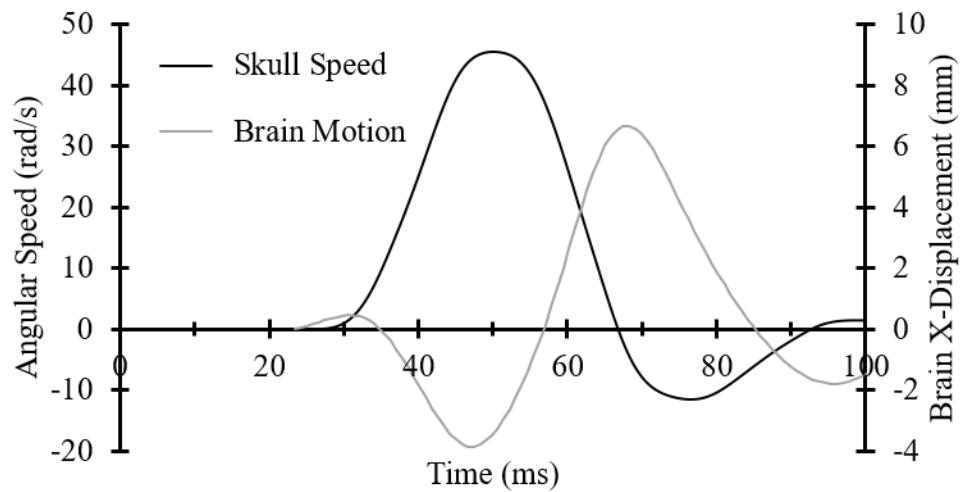
Figure 55. Comparison between the angular speed profile of one test (NDTA-T2) and displacement of one target.

The targets followed figure-eight and looping patterns, the magnitude and orientation of which are dependent on the location of each target in the brain. The magnitude and orientation of the figure-eight and looping patterns can be described by the major deformation axis (MDA) [33]. The MDA of each target is the long axis of the displacement pattern (Figure 56). The average instant center (AIC) of rotation is the point at which the perpendicular bisectors of each MDA in a column intersect [33]. Each column of targets has its own AIC that does not correspond with the c.g. of the head. Examination of x-ray videos as well as relative displacement calculations confirm that the targets did return to their initial position, showing that the targets were moving with the brain tissue and were not being displaced through the tissue. Major deformation axes of the targets follow a path that follows the contour of the part of the skull to which they are nearest. Since the brain is confined within the skull, and the cortex of the brain is essentially fixed to the skull along the midline, the deformation of the brain is guided in a path that follows the contour of the skull.
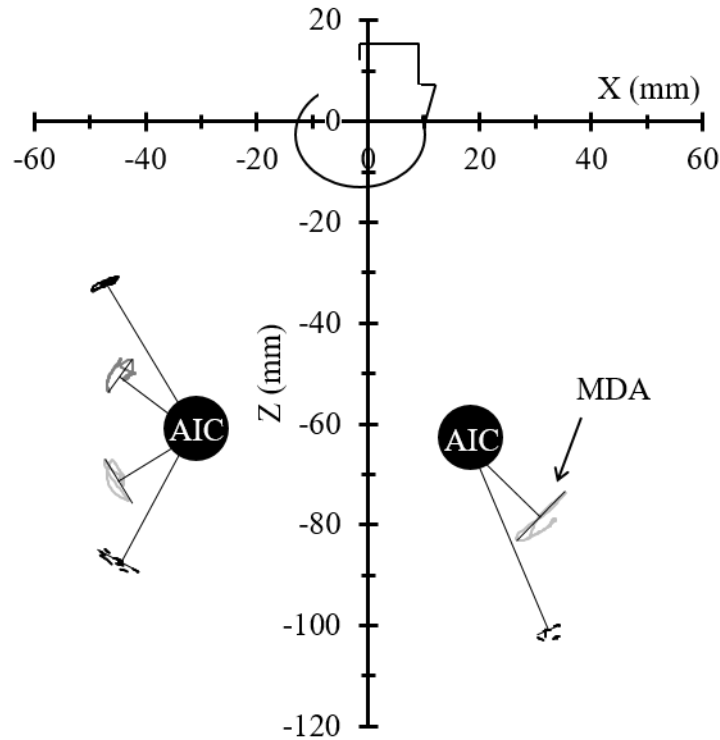
Figure 56. NDTA-T3 major deformation axes (MDA) and average instant centers (AIC) of rotation.

In this test series, the targets in the radial pattern (in the left hemisphere) had the largest relative displacement, and the deeper of the two rows exhibited larger displacements than the more superficial row. This is demonstrated most clearly in the middle column (targets along the reference coronal plane), which displaced largely in the X-direction as they followed the shape of the skull. The superficial radial targets had smaller displacements than the deeper targets because they were closer to the fixed boundary between the cerebral cortex and the skull. The deeper row of targets are farther from this constraint while still being far from the deep brain (where there is little motion), and are therefore located in the region of the brain in which the largest deformations would be expected. The radial targets also provide good comparison for the differences in Z-displacement trends as the middle targets are on the Z-axis, and the anterior and posterior targets are in similar positions reflected about the z-axis. When looking at the Z-displacement time histories from all three tests (Figure 19, Figure 22, Figure 26, Figure 30), a

76

clear trend in displacement based on A-P location is observed. The anterior targets first move superiorly while the posterior targets move inferiorly to the head coordinate system. Deformation of the middle targets was nearly zero in the Z-direction. The middle radial targets were near the apex of the skull, where the inner surface is nearly parallel to the x-axis; and therefore almost no relative motion occurred in the Z-direction. In the X-direction, all radial targets follow the same pattern. The deep middle target (MRB1) has the largest deformation in this direction, while all of the superficial targets have similar X-displacement magnitudes. This suggests restriction of motion of these targets, which are within one inch of the outer surface of the skull.

The posterior column of targets in the grid scheme illustrates the difference in relative motion between superficial and deep targets. It is apparent that the MDA of each target in the posterior column rotates to follow the contour of the skull (Figure 20, Figure 24, Figure 28). That is, PGB1 (near the base of the skull) and PGB4 (near the calvarium) undergo displacement primarily in the X-direction, and PGB2 and PGB3 are associated with deformation primarily in the Z-direction. The deeper targets have smaller magnitudes of displacement, and have slightly more inconsistent patterns of motion. The targets in the middle column (MGB3 and MGB4) both have more open "looping" patterns.

Trends in motion in the X and Z-directions were similar to those found in the Hardy et al. studies [14,15]. Figure 57 shows the relative X-displacement and angular speed in the sagittal plane from test C064-T2 from Hardy et al., 2007 [15]. Similar comparisons between angular speed and relative motion can be made. As the angular speed of the head increases the relative displacement of the brain increases. After the peak angular speed is reached, the head begins to slow down and the relative displacement reaches a peak. These trends are the same as the ones seen in the current study. However, there are several differences between the angular speed pulse produced in this study and the one in Figure 57. After the first peak there is a sustained plateau in

angular speed. During that time, the brain relaxes towards its initial conformation, reducing the relative displacement. There is then an additional peak, which causes another increase in the magnitude of the relative displacement. Finally, similarly to the current study, the head slows down and has a negative angular speed, and the brain relaxes to its initial conformation before twisting in the opposite direction, creating a positive relative displacement until the relative displacement returns to zero again. While the shape, magnitude, and duration of the angular speed pulse was different from the current study, the relationship between the angular speed of the head and the relative motion of the brain is the same. In all three studies, depth of the target determined the initial of motion in the X-direction, anterior/posterior location of the targets determined the initial motion in the Z-direction. Additionally, the average maximum displacement in the X-direction for NDTA was +/- 5 mm, whereas average maximum excursions measured in previous studies were 5 mm [14] and 7 mm [15] in the direction of impact.
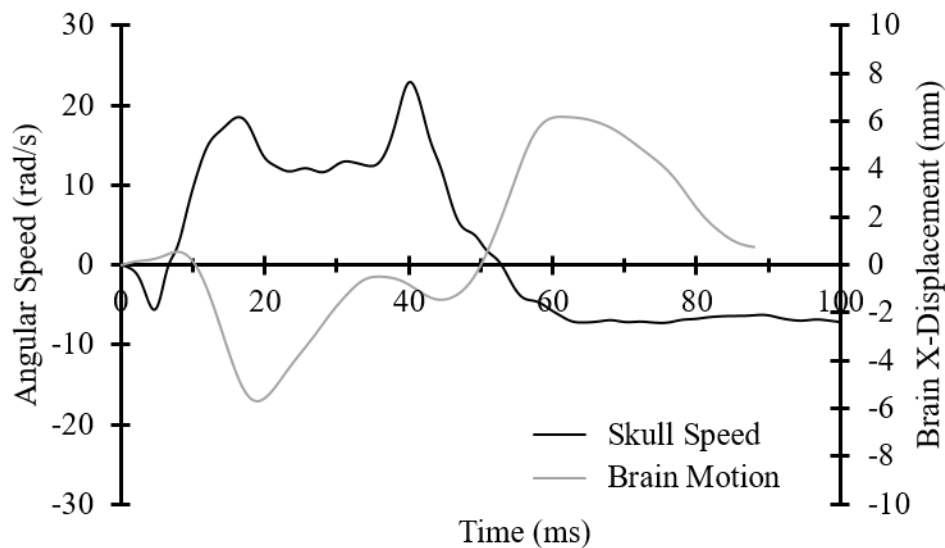

Figure 57. Comparison of angular speed and relative X-displacement from test C064-T2 [15].

Since the head was rotated in the sagittal plane, the right and left hemispheres should exhibit similar response shapes, as opposed to tests in the coronal plane, in which the falx cerebri

changes the response between hemispheres [15]. However, due to the different schemes for target deployment, the right-left symmetry in the brain response cannot be evaluated in these tests. The motion at two target locations can be compared because they were in similar positions in the X-Z plane (Figure 58). The X-displacement time histories for ARB1 and MGB3 (Figure 59) have the same phase, and overall change in displacement, although the MGB3 displacements correspond to a location in the brain that is approximately 4 mm more inferior. The Z-displacement time histories (Figure 59) show a slight phase shift between the points in NDTA-T2, but the overall path of displacement is very similar. Given that there is a slight difference in location between the points, it is suggested that the response at these locations is indicative of left-right symmetry in the brain's response.
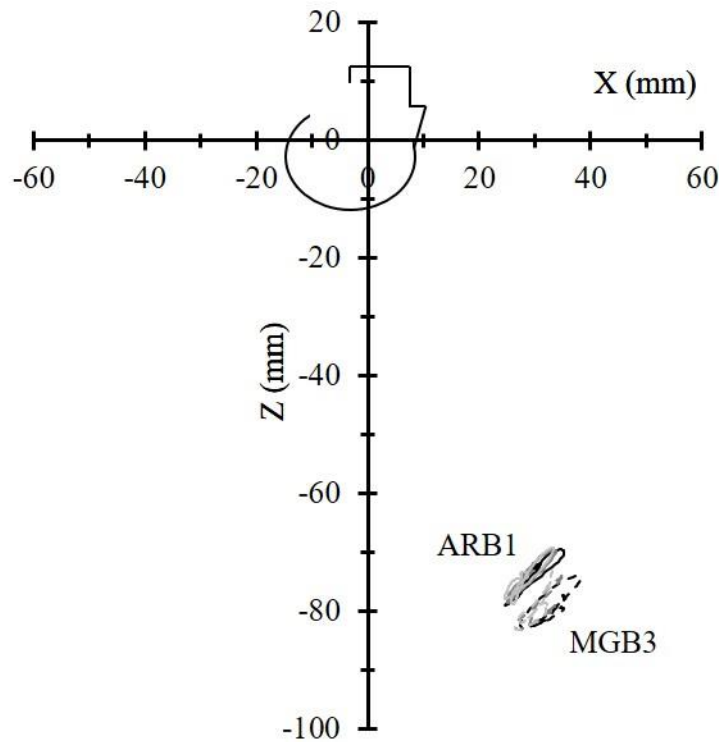

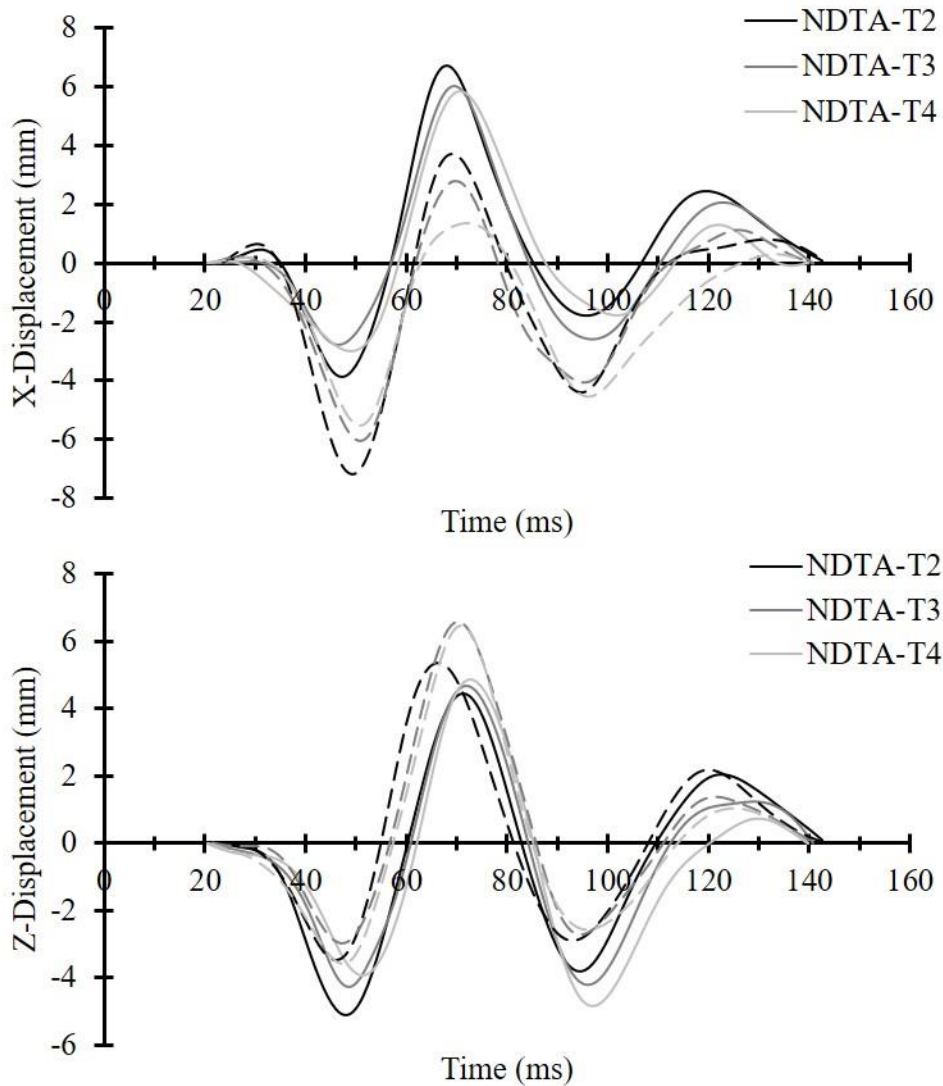**Figure 58. Comparison of position between ARB1 and MGB3 in NDTA.**

Figure 59. Time histories of ARB1 (solid lines) and MGB3 (dashed lines) in NDTA-T2 through T4.

For several targets, there was very little variation between tests. From comparisons of specific points between tests, (Appendix A), it is apparent that targets with small magnitudes of motion have more variability between tests. This occurs particularly with the deep targets, PGB1 and PGB2 (Figure -Figure), and Z-displacement of MRB1 and MRB2 (Figure and Figure). Other targets have good consistency in shape of the displacement time histories, but the NDTA-T2 data usually differs the most from the three sets of data. This is likely due to the fact that the peak angular speed of NDTA-T2 was 45.6 rad/s, while NDTA-T3 and T4 had peak angular

speeds of 39.5 and 36.8 rad/s, respectively. While of these trends can be seen visually, the comparisons of displacements from each test to the average displacement for each point (NRMSD) in

Table and Table show the same trends.

NDTB

Angular Speed

      The low-speed, long duration tests of NDTB had an average peak angular speed of 22.0 rad/s and average duration of 61.3 ms. NDTB-T4 had a peak angular speed of 44.3 rad/s, and positive duration of 42.4 rad/s. NDTB-T4 had a short negative phase (similar in magnitude to NDTA tests, Figure 60), however, the low-speed tests have a much smaller negative phase at the end of the pulse. The duration of the event was much closer to the desired duration for the low-speed tests than for NDTB-T4. For the low speed tests, the cam was rotating at half of the speed as for the NDTA test series and NDTB-T4. Decreasing the angular speed of the mass, decreases the angular momentum and therefore decreases the amount of energy transferred through the follower and the axle. With less energy transfer, the follower is less likely to lose contact with the cam, creating a closer match between the desired parameters and the parameters obtained experimentally (Figure 61.)
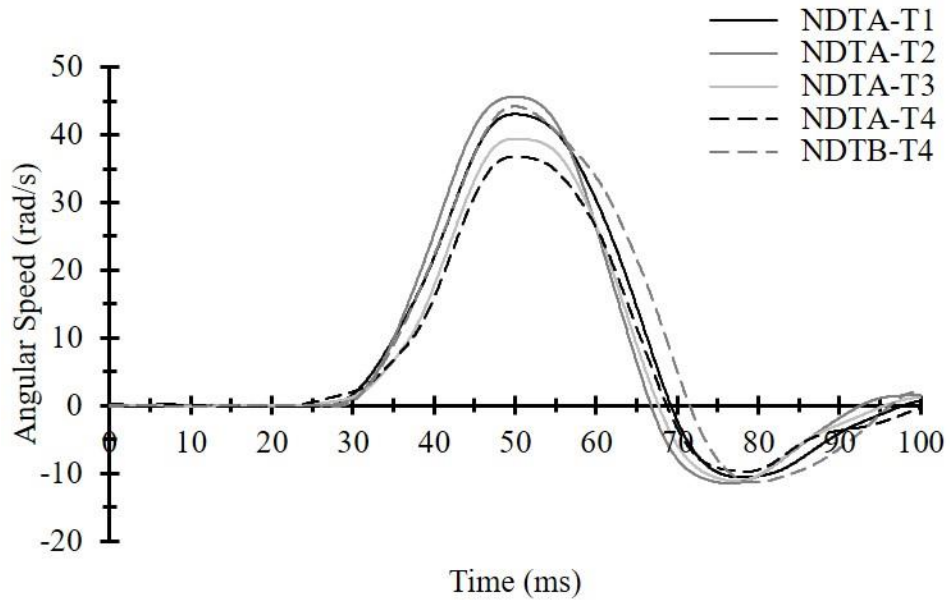
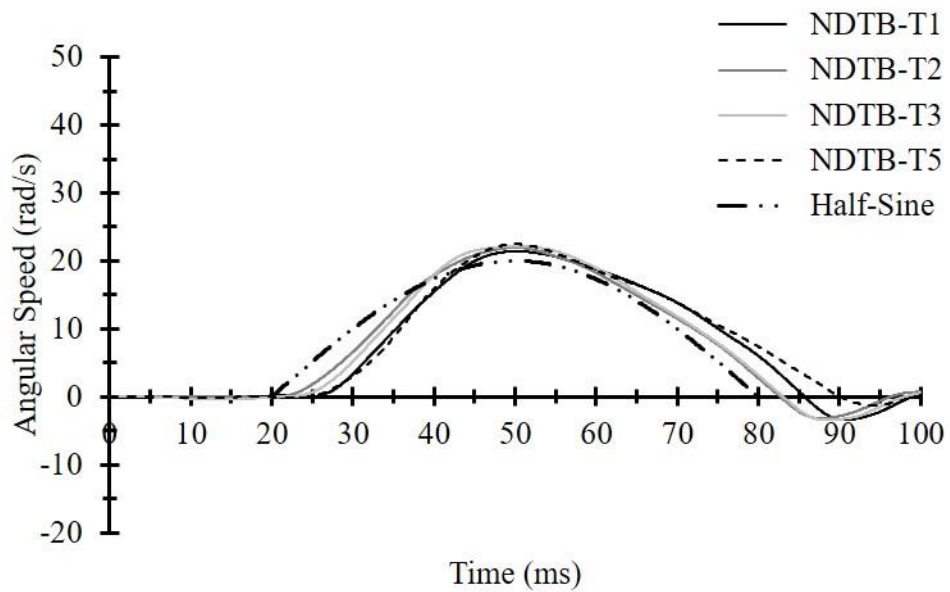**Figure 60. Angular speed profiles from NDTA and NDTB-T4.**

Figure 61. Angular speed pulses from the low-speed tests in NDTB with a half-sine resembling the ideal pulse.

Figure 61 shows an interesting difference between the ideal half-sine pulse and the low-speed pulses from NDTB. While the peak angular speeds were both aligned at coincident points, the event begins about 5 ms later than desired, and ends about 5 ms later than desired. The rising

edge of the pulse seems to have a nearly linear slope. After peak angular speed is reached, the head takes longer to slow down, following the expected path from the half-sine. A similar shape occurs in NDTB-T4 (Figure 62).
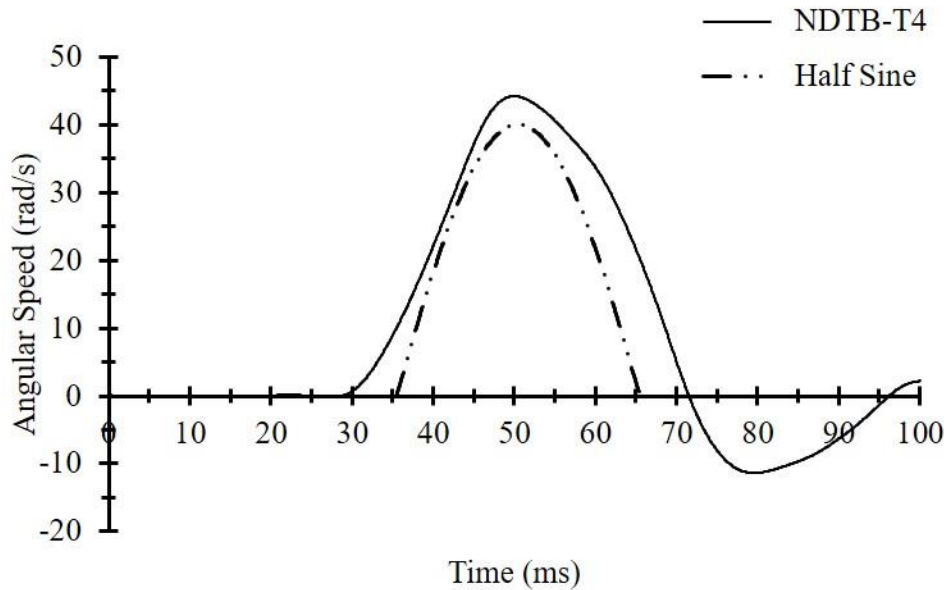

Figure 62. Angular speed of NDTB-T4 with the ideal half-sine pulse.

Like the tests in NDTA, the calculated NRMSD of the angular speed of each test showed good consistency between the low-speed tests in NDTB (average of 4.8%). The high-speed test, NDTB-T4, was compared to the average of all five high-speed tests. While the NRMSD for NDTB-T4 was 7.2%, the average NRMSD for the high-speed tests was 4.9%, a 0.8% increase from the comparison including only the tests in NDTA.

The high-speed tests from NDTA and NDTB had an average peak angular acceleration of 3,442 rad/sec^2. With an average peak angular speed of 41.8 rad/s, the high-speed tests from this study are in the AIS 4 injury category as proposed by Ommaya [4]. The low-speed tests in NDTB had an average peak angular acceleration of 1183 rad/s^2 and average peak angular speed of 22.0 rad/s; therefore the low-speed tests are in the AIS 0/1 category. For reference, if the low-speed tests had the same peak angular acceleration as the high-speed tests, they would also be

rated an AIS of 0/1. This highlights the importance of using both angular acceleration and angular speed as a temporal component.

Intracranial Pressure

The ICP measured in the NDTB series follow the same trends as in the NDTA series. The four low-speed tests in NDTB had peak ICPs of as little as half the magnitude of those in the NDTA tests while differences were dependent on location and the polarity of the ICP being considered. Table 10 contains the maximum and minimum ICP values from the NDTB series. Clear differences are shown between the low speed tests and NDTB-T4, with minimum occipital ICP being only a quarter of the magnitude of that from NDTB-T4. When comparing NDTB-T4 to the ICP traces from the NDTA series (Figure 63), the phase and duration of the pressure profiles are the same. The magnitudes of ICP are similar, however the maximum ICPs at the frontal and occipital regions were larger in NDTB-T4.
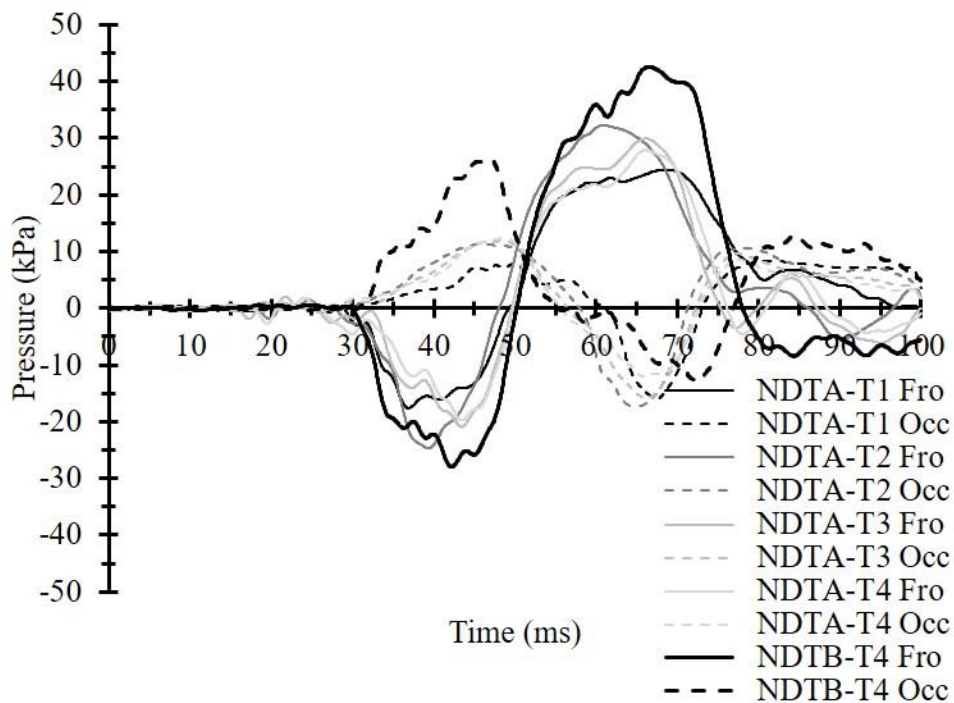

Figure 63. ICP from all high-speed tests in NDTA and NDTB.

84

Some of the differences in ICPs produced between impact and rotational loading can be observed when comparing the low speed tests in NDTB and some tests from Hardy et al. [15]. The measured angular speed of the head specimens in the Hardy study was typically 20 - 25 rad/s, which is similar to the low speed tests in NDTB (average of 22.0 rad/s). In the current study, ICP magnitudes reached about 10 kPa, while coup ICP in the Hardy study was as large as 150 kPa. While ICP was measured differently in each study, it is clear that the ICP response is dominated by the effects of impact.

Brain Kinematics

Relative displacement of all points in the low-speed tests in the NDTB series are much smaller than in the NDTA series and NDTB-T4. The average maximum X-displacement in the high-speed tests was +/- 5 mm, however the maximum average X-displacement in the low-speed tests was +/- 3 mm. While these magnitude changes are expected, the change in orientation and shape of the X-Z traces was not expected. While figure-eight and looping patterns still occur, the orientation of the MDAs does not appear to change. Several things could cause this difference. The most probable factor is that the plane distortion correction method typically used prior to 3D reconstruction did not work well for either test. This lead to post-analysis 3D corrections that ensured that the original target locations matched those designated during the stereotaxis/implanting procedure, and that rigid points on the skull did not move relative to each other. This post-analysis correction could lead to differences between test series. In further analysis of these data and future tests, a more robust distortion correction software will be used for initial correction of the x-ray videos.

Conclusions

Two PMHS head specimens were tested under two different angular speed profiles involving no linear impact. High-speed biplane x-ray was used to measure the deformation of the

brain with respect to the skull throughout these tests. Motion of several points throughout the brain was measured using radio-opaque tin targets, which were deployed in a prescribed, scalable, and repeatable manner that was developed as part of this study. Relative brain motions were shown to follow a MDA that was specific to each point. The magnitude and orientation of the MDAs were dependent on the target's location in the brain. The targets transcribed figure-eight and looping patterns along each MDA. Intracranial pressure was measured in frontal and occipital locations, and were much smaller than in tests involving impact.

Test inputs were consistent, and varied in magnitude by only about 10%. The target deployment schemes and stereotactic frame allowed for controlled deployment of radio-opaque targets in exact locations in the brain which were determined based on the anthropometry of each specimen.

Further improvements will facilitate improved control of energy transfer between the cam and follower to make sure the follower does not lose contact with the cam and does not allow the head to over-rotate or rebound. Improved distortion correction will be applied to x-ray video frames before data analysis so that a consistent correction can be obtained. The improved distortion correction will increase the accuracy or the relative motion measurements, and will likely show better fit of data between tests. More tests need to be conducted so that response corridors can developed for FE model evaluation and validation. An increased number of tests could also further clarify differences between test pulses, and highlight differences caused by subject-to-subject variation. Additionally, Angular speed profiles that are low-speed, low-duration, and high-speed, high-duration, would demonstrate how changes in angular acceleration affect the response of the brain.
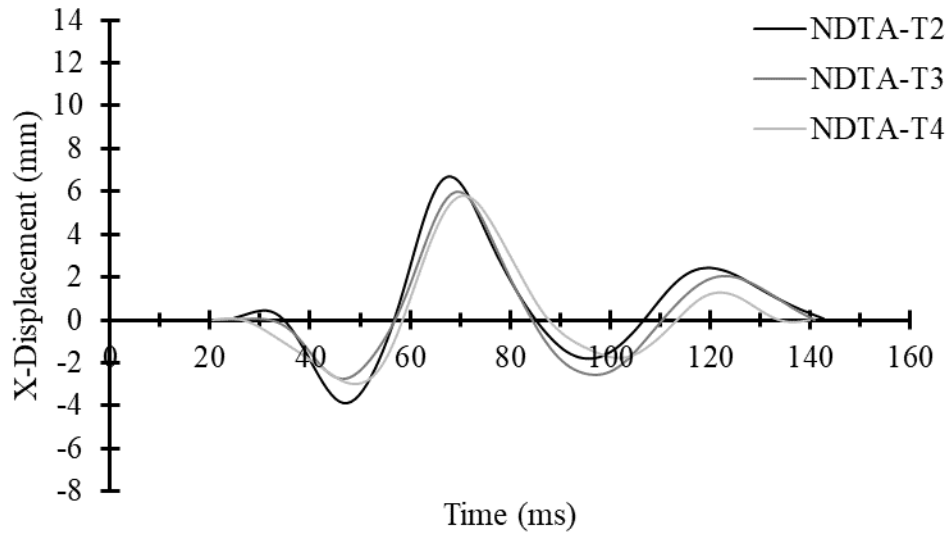
Appendix A

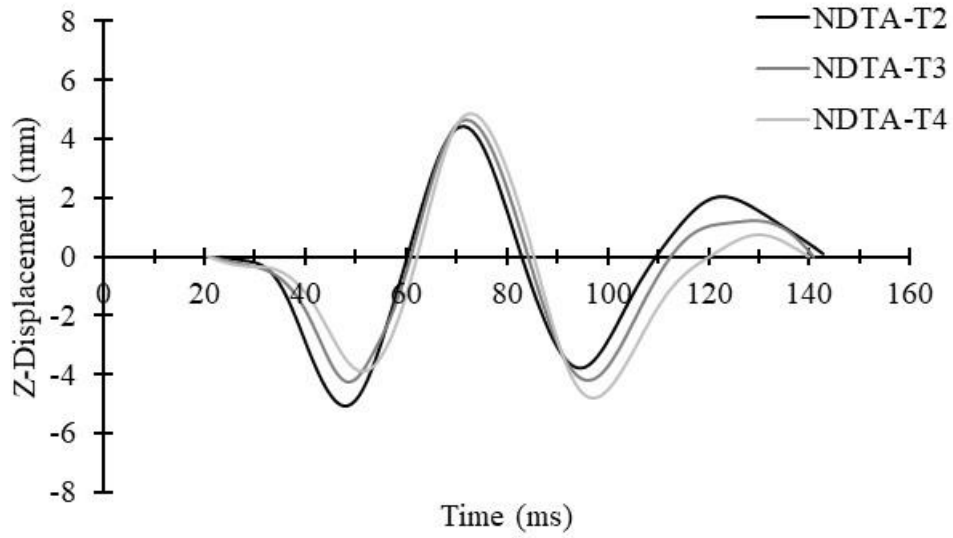**Figure A1. X-displacement of ARB1 from all tests in NDTA**

Figure A2. Z-displacement of ARB1 from all tests in NDTA
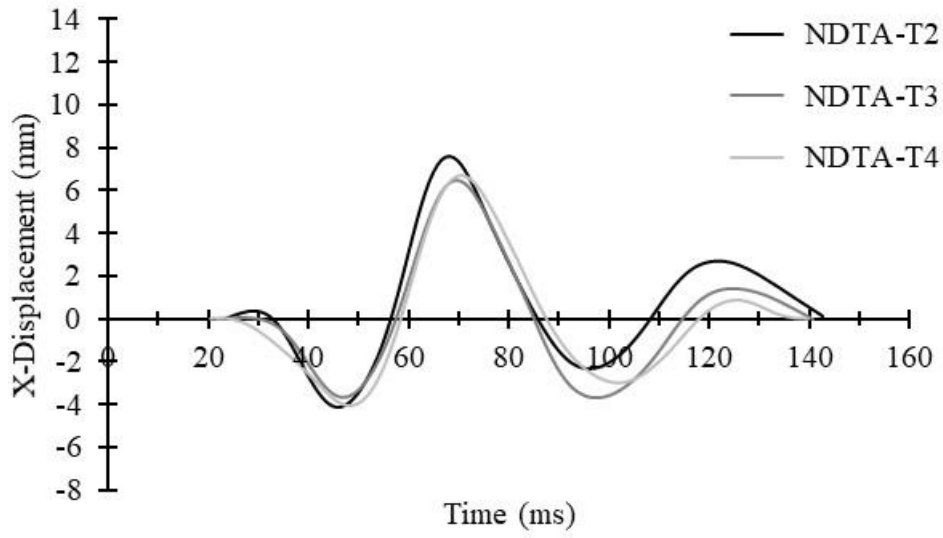
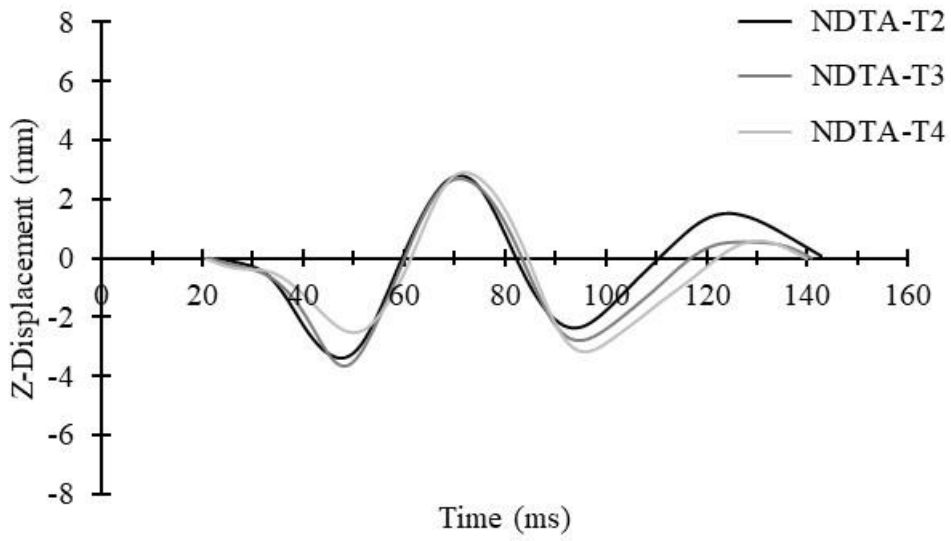**Figure A3. X-displacement of ARB2 from all tests in NDTA**
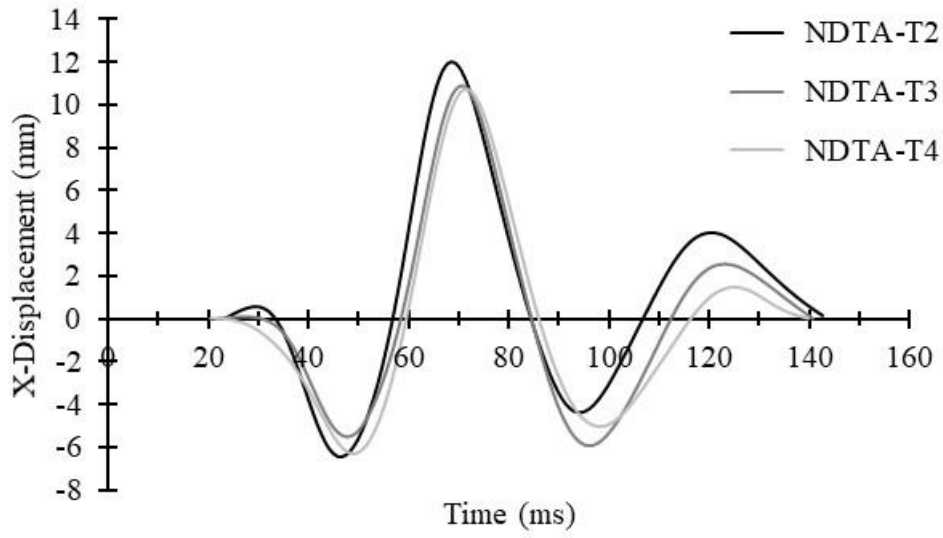

Figure A4. Z-displacement of ARB2 from all tests in NDTA
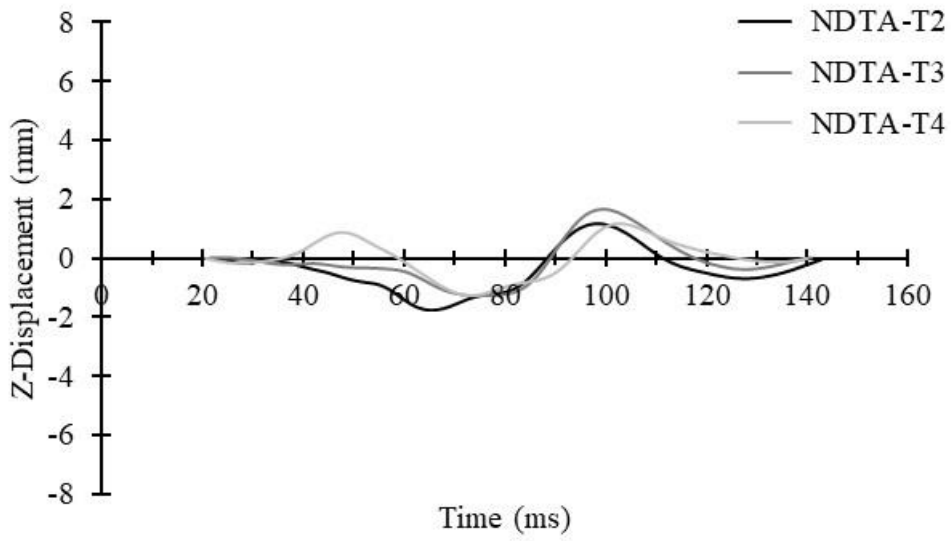
Figure A5. X-displacement of MRB1 from all tests in NDTA

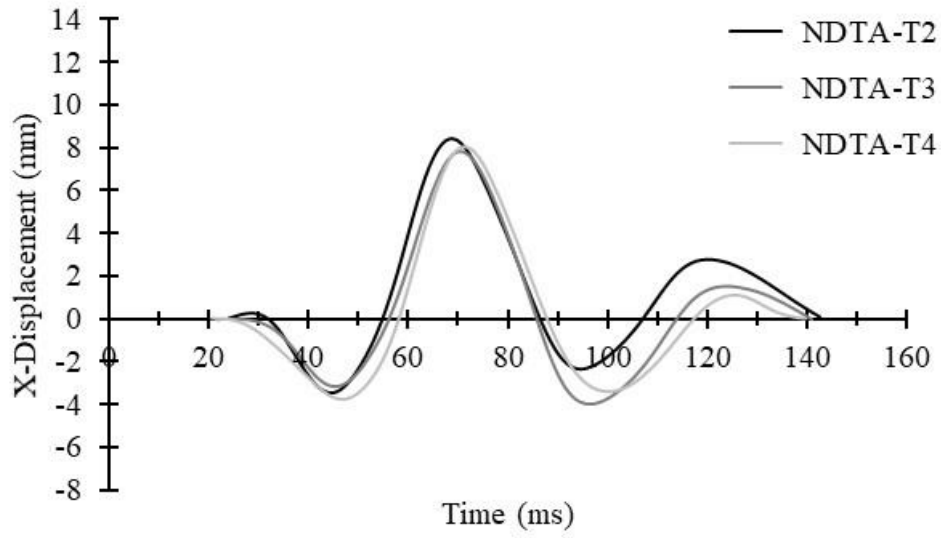**Figure A6. Z-displacement of MRB1 from all tests in NDTA**

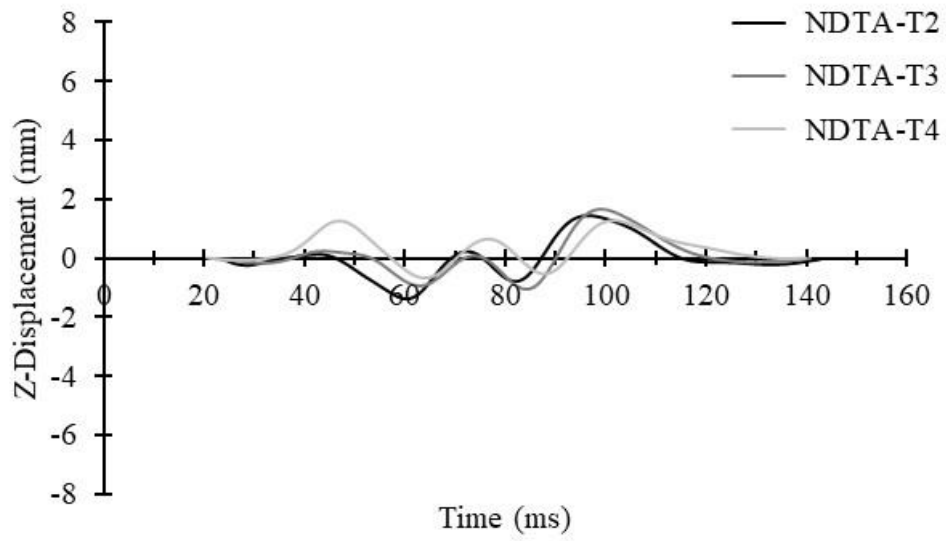**Figure A7. X-displacement of MRB2 from all tests in NDTA**
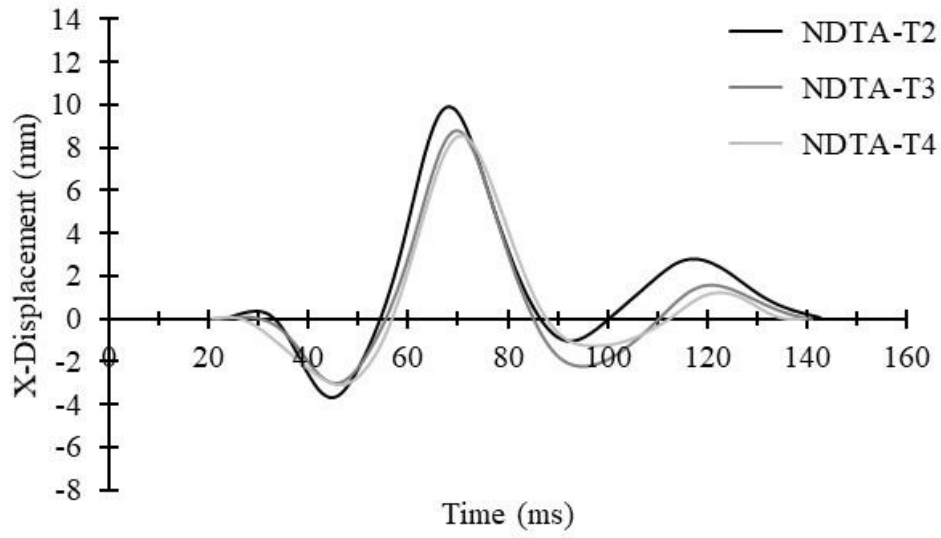

Figure A8. Z-displacement of MRB2 from all tests in NDTA

Figure A9. X-displacement of PRB1 from all tests in NDTA
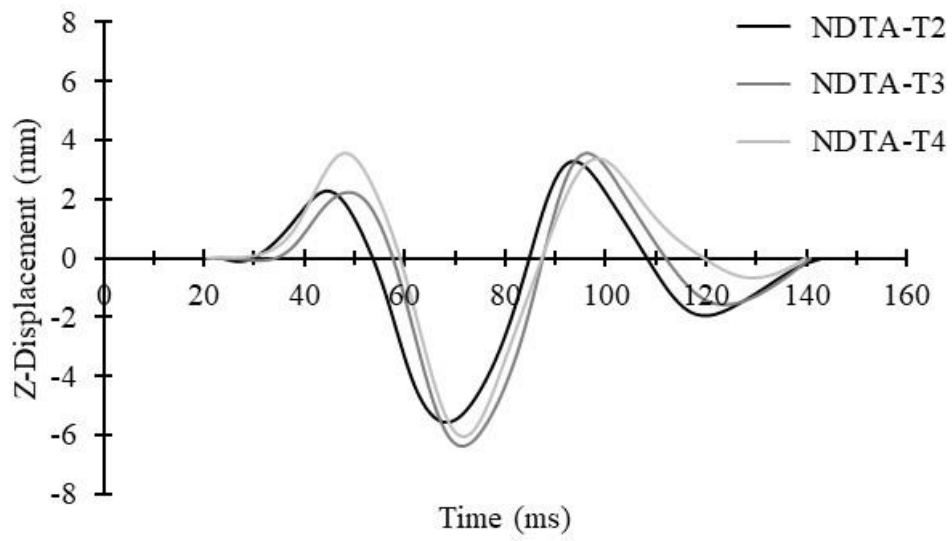

Figure A10. Z-displacement of PRB1 from all tests in NDTA

Figure A11. X-displacement of PRB2 from all tests in NDTA

Figure A12. Z-displacement of PRB2 from all tests in NDTA

Figure A13. X-displacement of MGB3 from all tests in NDTA

Figure A14. Z-displacement of MGB3 from all tests in NDTA

Figure A15. X-displacement of MGB4 from all tests in NDTA

Figure A16. Z-displacement of MGB4 from all tests in NDTA

Figure A17. X-displacement of PGB1 from all tests in NDTA

Figure A18. Z-displacement of PGB1 from all tests in NDTA
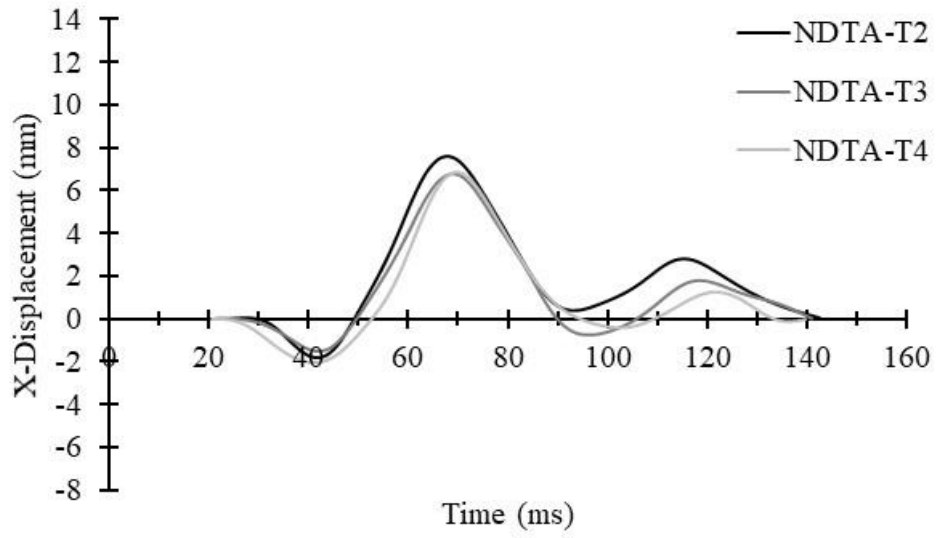
95

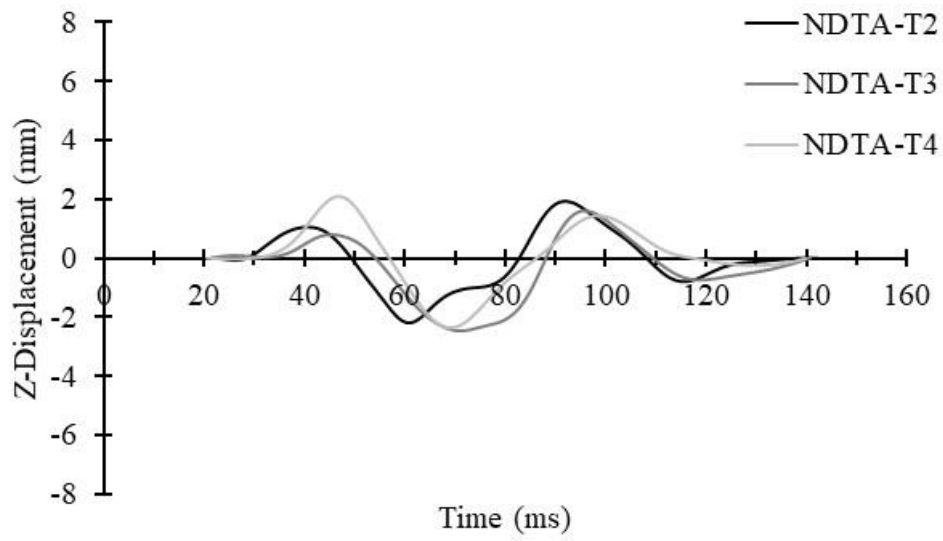**Figure A19. X-displacement of PGB2 from all tests in NDTA**

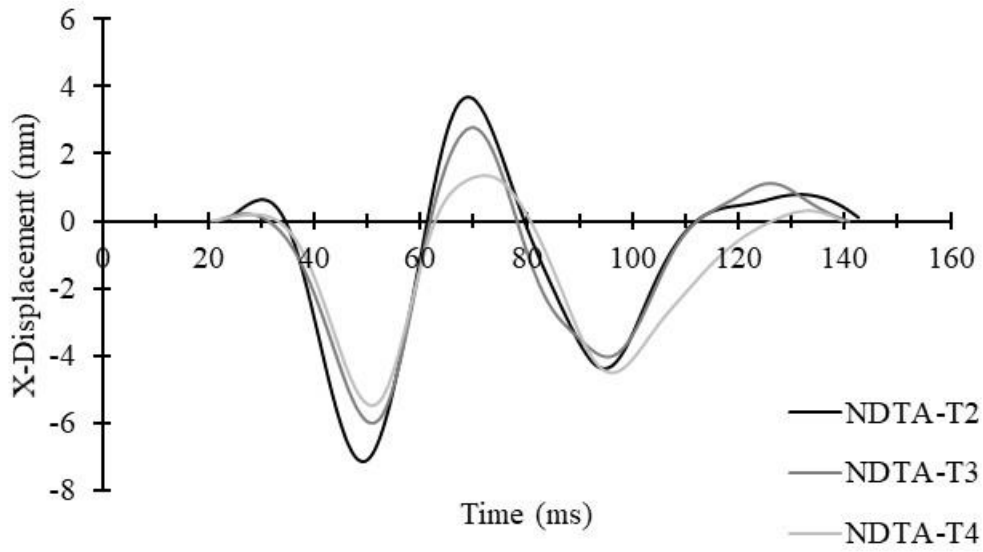**Figure A20. Z-displacement of PGB2 from all tests in NDTA**
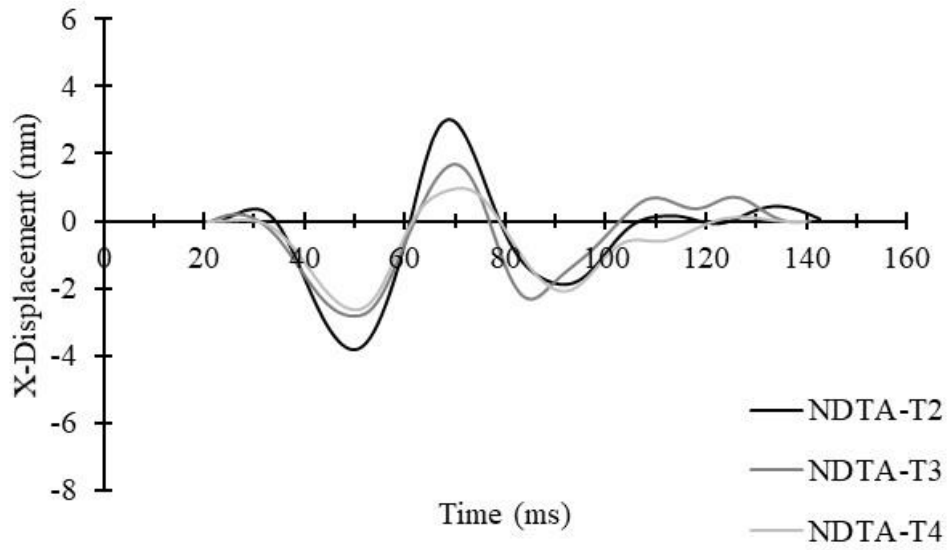
Figure A21. X-displacement of PGB3 from all tests in NDTA
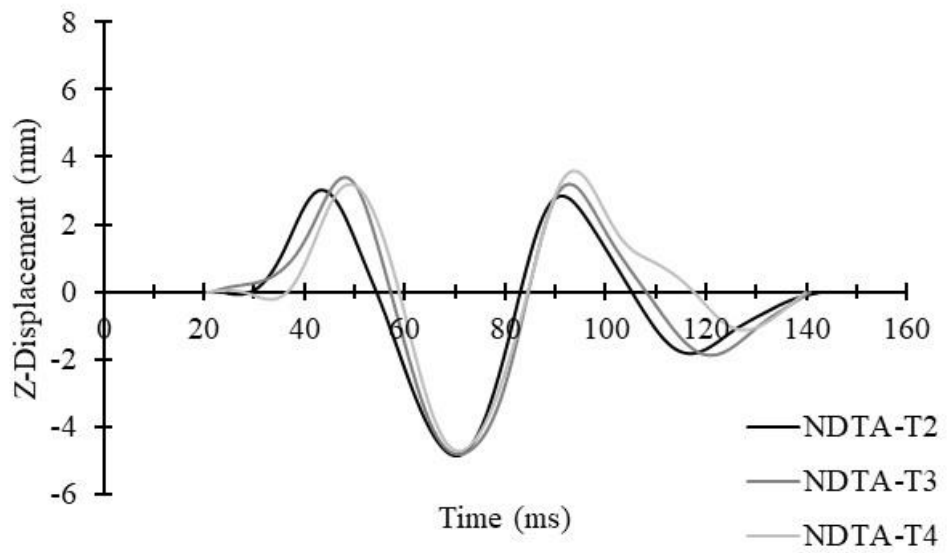
Figure A22. Z-displacement of PGB3 from all tests in NDTA
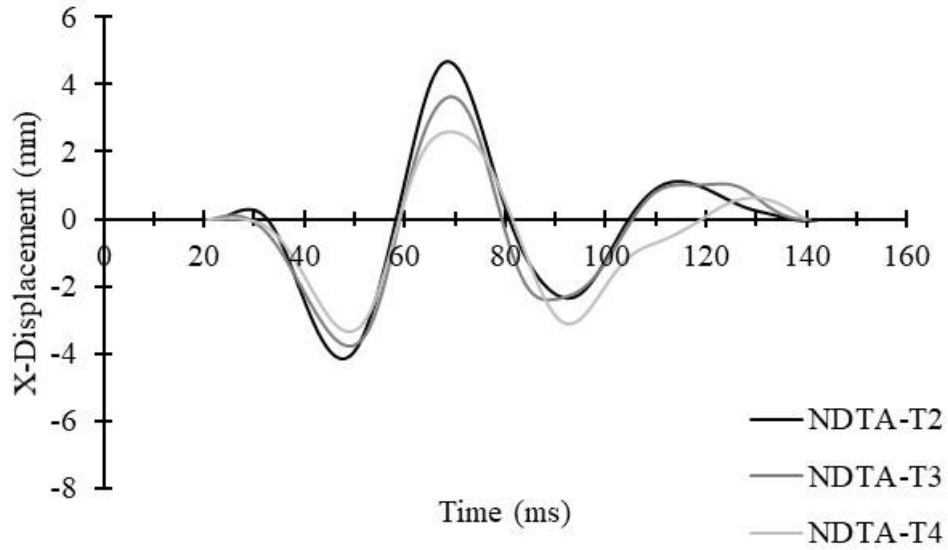
Figure A23. X-displacement of PGB4 from all tests in NDTA
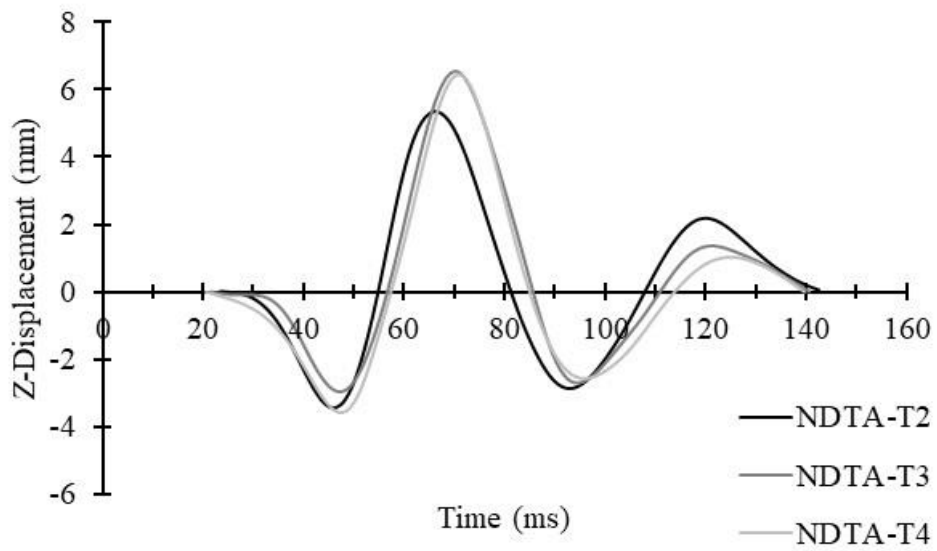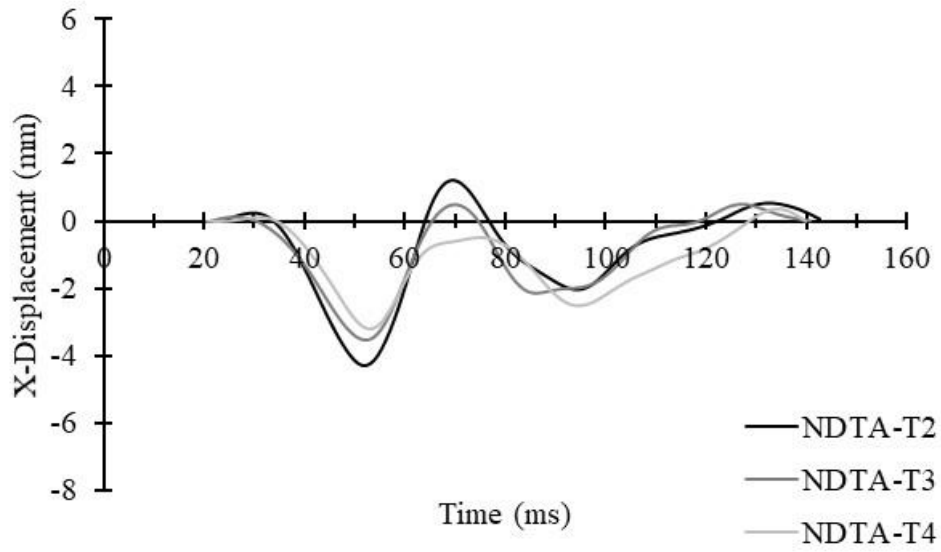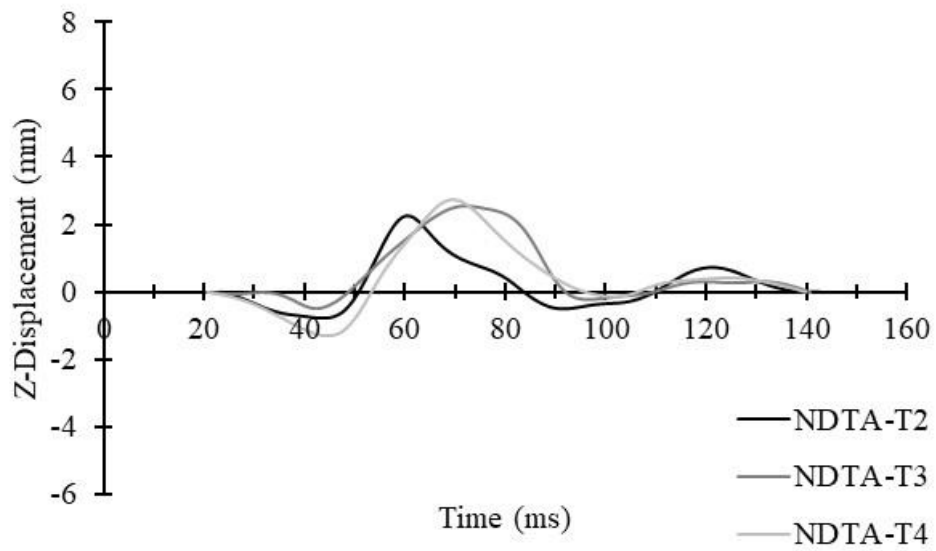

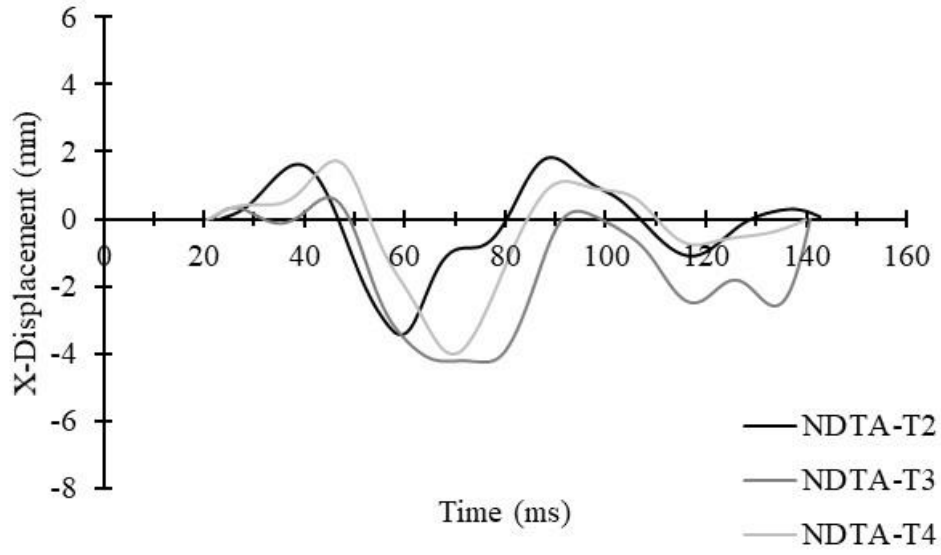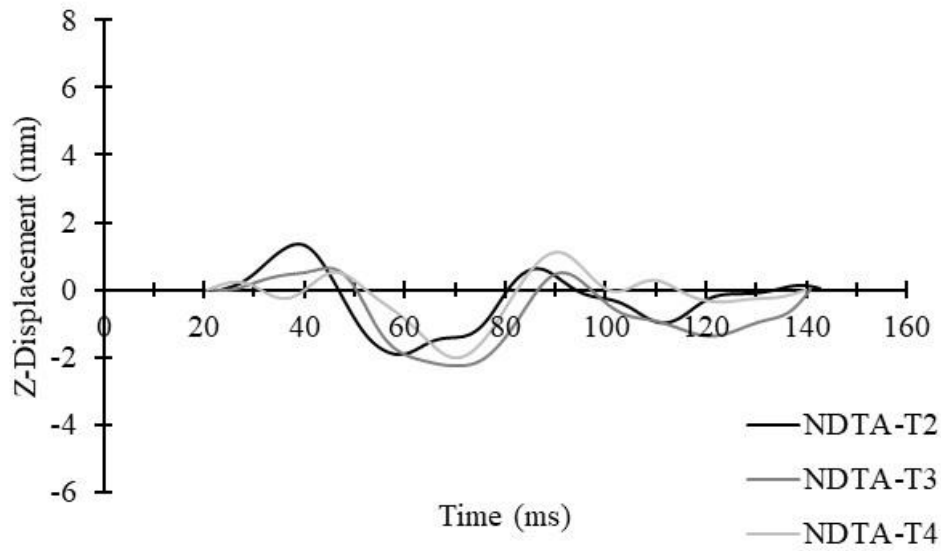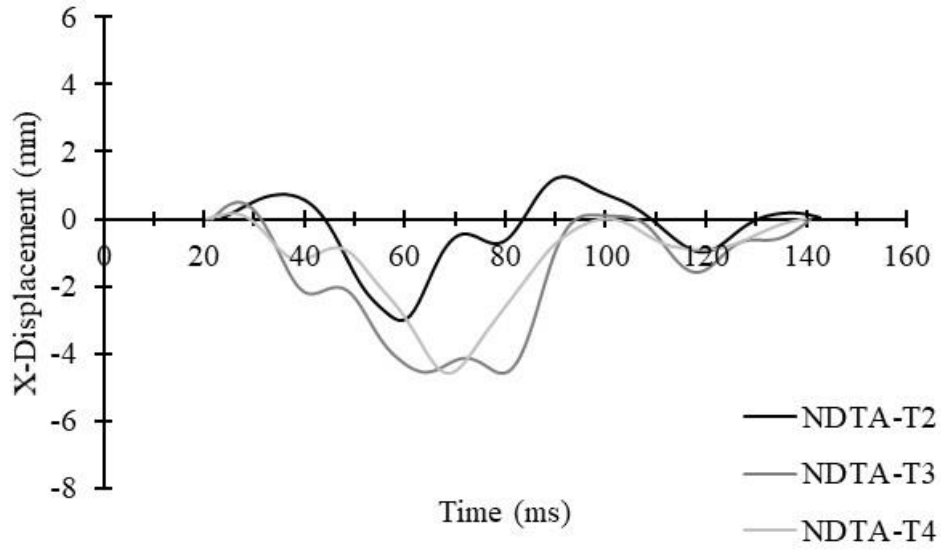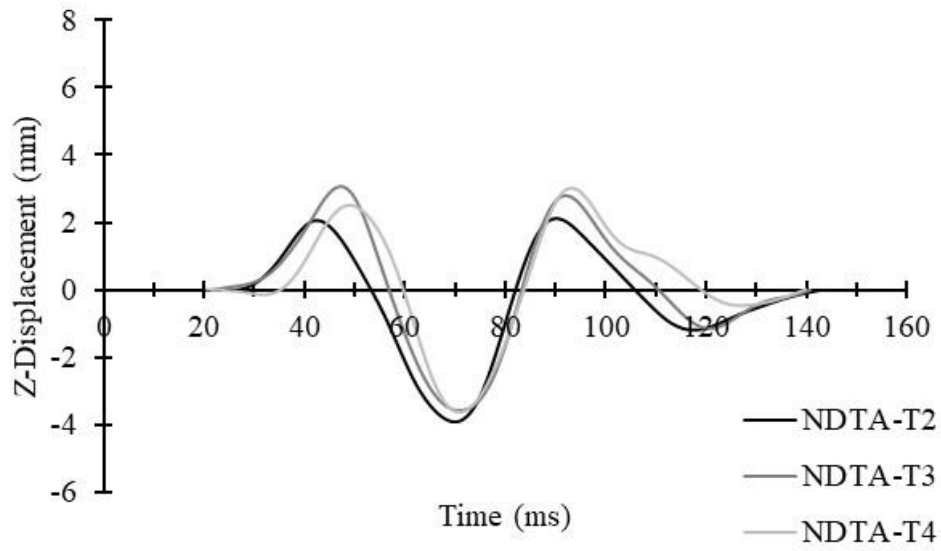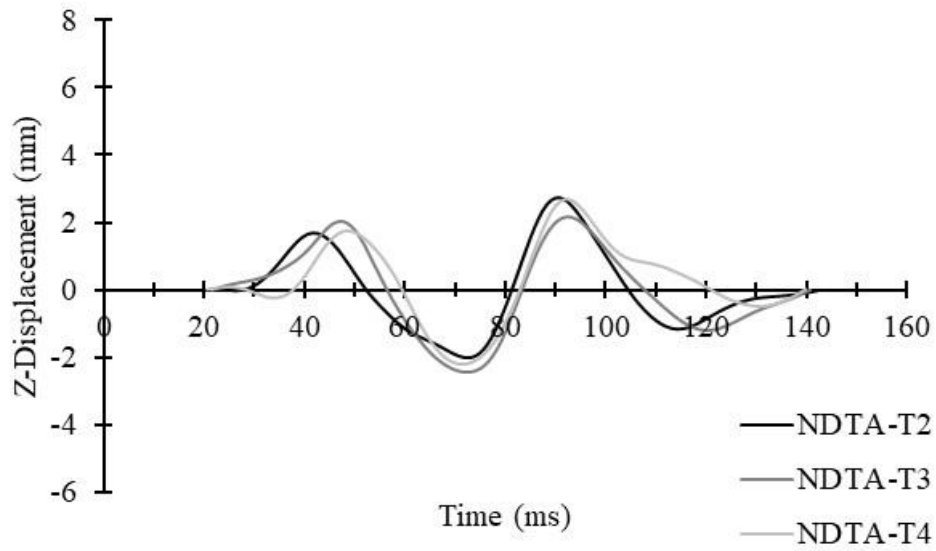**Figure A24. Z-displacement of PGB4 from all tests in NDTA**

Table A1. NRMSD of radial targets (in left hemisphere) in NDTA.

		ARB1	ARB2	MRB1	MRB2	PRB1	PRB2
NDTA-T2	X	5.50 %	7.22 %	6.71 %	7.59 %	6.17 %	6.89 %
	Z	6.89 %	7.75 %	14.11 %	13.33 %	8.33 %	14.45 %
NDTA-T3	X	3.60 %	3.76 %	2.60 %	3.43 %	3.27 %	3.17 %
	Z	1.09 %	2.78 %	6.79 %	6.83 %	4.17 %	10.94 %
NDTA-T4	X	5.95 %	5.92 %	5.67 %	6.38 %	4.61 %	5.94 %
	Z	6.96 %	7.38 %	15.15 %	15.50 %	7.10 %	11.58 %

Table A2. NRMSD of grid targets (in right hemisphere) in NDTA.

		MGB3	MGB4	PGB1	PGB2	PGB3	PGB4
NDTA-T2	X	5.98 %	8.72 %	23.16 %	28.98 %	8.27 %	5.50 %
	Z	7.98 %	15.85 %	16.24 %	8.71 %	7.26 %	8.90 %
NDTA-T3	X	3.93 %	5.90 %	25.00 %	22.30 %	6.65 %	3.54 %
	Z	4.22 %	12.05 %	15.69 %	3.91 %	3.25 %	5.65 %
NDTA-T4	X	7.50 %	10.95 %	14.56 %	12.62 %	7.53 %	6.89 %
	Z	4.90 %	9.52 %	16.72 %	8.16 %	7.29 %	9.39 %

References

[1]   M. Faul, L. Xu, M. M. Wald, and V. G. Coronado, "Traumatic brain injury in the United States: emergency department visits, hospitalizations, and deaths," Atlanta (GA), 2010.

[2]   World Health Organization, "Global Status Report on Road Safety 2015," *WHO Libr. Cat. Data Glob.*, p. 340, 2015.

[3]   J. Versace, "A review of the severity index," *SAE Int.*, pp. 771–797, 1971.

[4]   A. K. Ommaya, "Biomechanics of Head Injury: Experimental Aspects," in *The biomechanics of trauma*, Appleton & Lange, 1985, pp. 245–269.

[5]   E. G. Takhounts, M. J. Craig, K. Moorhouse, J. McFadden, and V. Hasija, "Development of brain injury criteria (BrIC).," *Stapp Car Crash J.*, vol. 57, no. November, pp. 243–66, 2013.

[6]   E. G. Takhounts, S. A. Ridella, V. Hasija, R. E. Tannous, J. Q. Campbell, D. Malone, K. Danelson, J. Stitzel, S. Rowson, and S. Duma, "Investigation of traumatic brain injuries using the next generation of simulated injury monitor (SIMon) finite element head model," SAE Technical Paper, 2008.

[7]   H. Mao, L. Zhang, B. Jiang, V. V Genthikatti, X. Jin, F. Zhu, R. Makwana, A. Gill, G. Jandir, and A. Singh, "Development of a finite element human head model partially validated with thirty five experimental cases," *J. Biomech. Eng.*, vol. 135, no. 11, p. 111002, 2013.

[8]   S. Kleiven, "Predictors for traumatic brain injuries evaluated through accident reconstructions," SAE Technical Paper, 2007.

[9]   C. Giordano, R. J. H. Cloots, J. A. W. Van Dommelen, and S. Kleiven, "The influence of anisotropy on brain injury prediction," *J. Biomech.*, vol. 47, no. 5, pp. 1052–1059, 2014.

[10]   H. Kimpara, Y. Nakahira, M. Iwamoto, K. Miki, K. Ichihara, S. Kawano, and T. Taguchi, "Investigation of anteroposterior head-neck responses during severe frontal impacts using a brain-spinal cord complex FE model," SAE Technical Paper, 2006.

[11]   W. Zhao, Y. Cai, Z. Li, and S. Ji, "Injury prediction and vulnerability assessment using strain and susceptibility measures of the deep white matter," *Biomech. Model. Mechanobiol.*, vol. 16, no. 5, pp. 1709–1727, 2017.

[12]   C. Deck and R. Willinger, "Improved head injury criteria based on head FE model," *Int. J. Crashworthiness*, vol. 13, no. 6, pp. 667–678, 2008.

[13]   A. M. Nahum, R. Smith, and C. C. Ward, "Intracranial pressure dynamics during head impact," SAE Technical Paper, 1977.

[14]   W. N. Hardy, C. D. Foster, M. J. Mason, K. H. Yang, a I. King, and S. Tashman, "Investigation of Head Injury Mechanisms Using Neutral Density Technology and High-Speed Biplanar X-ray.," *Stapp Car Crash J.*, vol. 45, no. November, pp. 337–368, 2001.

[15]   W. N. Hardy, M. J. Mason, C. D. Foster, C. S. Shah, J. M. Kopacz, K. H. Yang, A. I. King, J. Bishop, M. Bey, and W. Anderst, "A study of the response of the human cadaver head to impact," *Stapp Car Crash J.*, vol. 51, p. 17, 2007.

[16]   C. Giordano and S. Kleiven, "Development of an unbiased validation protocol to assess the biofidelity of finite element head models used in prediction of traumatic brain injury," SAE Technical Paper, 2016.

[17]   R. H. Pudenz and C. H. Shelden, "The lucite calvarium—a method for direct observation

of the brain: II. Cranial trauma and brain movement," *J. Neurosurg.*, vol. 3, no. 6, pp. 487–505, 1946.

[18] H. H. Gosch, E. Gooding, and R. C. Schneider, "Distortion and displacement of the brain in experimental head injuries.," in *Surgical forum*, 1969, vol. 20, p. 425.

[19] V. R. Hodgson, E. S. Gurdjian, and L. M. Thomas, "Experimental skull deformation and brain displacement demonstrated by flash x-ray technique," *J. Neurosurg.*, vol. 25, no. 5, pp. 549–552, 1966.

[20] S. A. Shatsky, W. A. Alter, D. E. Evans, V. W. Armbrustmacher, K. M. Earle, and G. Clark, "Traumatic distortions of the primate head and chest: correlation of biomechanical, radiological and pathological data," SAE Technical Paper, 1974.

[21] R. L. Stalnaker, J. W. Melvin, G. S. Nusholtz, N. M. Alem, and J. B. Benson, "Head Impact Response." SAE International, 1977.

[22] W. N. Hardy, C. D. Foster, A. I. King, and S. Tashman, "Investigation of brain injury kinematics: introduction of a new technique," *ASME Appl. Mech. Div.*, vol. 225, pp. 241–254, 1997.

[23] A. S. Al-Bsharat, W. N. Hardy, K. H. Yang, T. B. Khalil, S. Tashman, and A. I. King, "Brain/skull relative displacement magnitude due to blunt head impact: new experimental data and model," SAE Technical Paper, 1999.

[24] X. Trosseille, C. Tarriere, F. Lavaste, F. Guillon, and A. Domont, "Development of a FEM of the human head according to a specific test protocol," SAE Technical Paper, 1992.

[25] H. Zou, J. P. Schmiedeler, and W. N. Hardy, "Separating brain motion into rigid body displacement and deformation under low-severity impacts," *J. Biomech.*, vol. 40, no. 6, pp. 1183–1191, 2007.

[26] S. S. Margulies, L. E. Thibault, and T. A. Gennarelli, "Physical model simulations of brain injury in the primate.," *J. Biomech.*, vol. 23, no. 8, pp. 823–836, 1990.

[27] T. A. Gennarelli, J. H. Adams, and D. I. Graham, "Acceleration induced head injury in the monkey. I. The model, its mechanical and physiological correlates," in *Experimental and Clinical Neuropathology*, Springer, 1981, pp. 23–25.

[28] J. H. Adams, D. I. Graham, and T. A. Gennarelli, "Acceleration induced head injury in the monkey. II. Neuropathology," in *Experimental and Clinical Neuropathology*, Springer, 1981, pp. 26–28.

[29] S. Ji, Q. Zhu, L. Dougherty, and S. S. Margulies, "In vivo measurements of human brain displacement," *Stapp Car Crash J.*, vol. 48, p. 227, 2004.

[30] P. V. Bayly, T. S. Cohen, E. P. Leister, D. Ajo, E. Leuthardt, and G. M. Genin, "Deformation of the human brain induced by mild acceleration," *J. Neurtotrauma*, vol. 22, no. 8, pp. 845–856, 2005.

[31] G. S. Nusholtz, P. Lux, P. Kaiker, and M. A. Janicki, "Head impact response—Skull deformation and angular accelerations," SAE Technical Paper, 1984.

[32] L. Zhang, K. H. Yang, R. Dwarampudi, K. Omori, T. Li, K. Chang, W. N. Hardy, T. B. Khalil, and a I. King, "Recent advances in brain injury research: a new human head model development and validation.," *Stapp Car Crash J.*, vol. 45, no. DECEMBER, pp. 369–394, 2001.

[33] S. Kleiven and W. N. Hardy, "Correlation of an FE model of the human head with local brain motion: Consequences for injury prediction," *Stapp Car Crash J.*, vol. 46, pp. 123–144, 2002.

[34] E. G. Takhounts, R. H. Eppinger, J. Q. Campbell, and R. E. Tannous, "On the

development of the SIMon finite element head model," *Stapp Car Crash J.*, vol. 47, p. 107, 2003.

[35] Y.-S. Kang, K. Moorhouse, and J. H. Bolte, "Measurement of Six Degrees of Freedom Head Kinematics in Impact Conditions Employing Six Accelerometers and Three Angular Rate Sensors (6aω Configuration)," *J. Biomech. Eng.*, vol. 133, no. 11, p. 111007, 2011.